

A Dissertation for the Degree of Doctor of Science

**Vertical coupling in the polar mesosphere and lower thermosphere:
Event studies of a gravity wave and a sporadic sodium layer**

Toru Takahashi

Division of Particle and Astrophysical Science
Graduate School of Science
(Solar-Terrestrial Environment Laboratory)
Nagoya University, Japan

2015

Acknowledgements

I would like to express my deepest gratitude to my supervisor Associate Professor Satonori Nozawa of the Solar-Terrestrial Environment Laboratory (STEL), Nagoya University for his continuous encouragement of my work on this thesis. He gave me an opportunity to step into the leading edge of aeronomy.

Dr. Oyama of the STEL has supported me throughout my work. I would like to appreciate so much his advice.

Special thanks are due to the members of advisory committee on my thesis in STEL, the chairman Associate Professor Satonori Nozawa, Professor Kazuo Shiokawa, and Professor Akira Mizuno, and Associate Professor Yuichi Otsuka.

I am deeply grateful to Dr. Masaki Tsutsumi, Dr. Yasunobu Ogawa of the National Institute of Polar Research (NIPR), Dr. Takuo Tsuda of the University of Electro-Communications, Dr. Shin Suzuki, Mr. Tetsuya Kawabata of the STEL, Professor Chris Hall of the Tromsø Geophysical Observatory, University of Tromsø, Dr. Takuya Kawahara of the Faculty of Engineering, Shinshu University, Dr. Norihito Saito, Dr. Satoshi Wada of the RIKEN Center for Advanced Photonics, RIKEN, Professor Hitoshi Fujiwara of the Faculty of Science and Technology, Seikei University, Professor Asgeir Brekke of the Faculty of Science, University of Tromsø, Professor Alan Manson, and Professor Chris Meek of the Institute of Space and Atmospheric Studies, University of Saskatchewan for their useful suggestions, comments, and technical supports of the sodium LIDAR operation.

I express my appreciation to Professor Ryoichi Fujii, Professor Nobuo Matuura, Professor Kazuo Shiokawa, Professor Masahumi Hirahara, Dr. Nozomu Nishitani, Dr. Yuichi Otsuka, and Dr. Manabu Shimoyama of the STEL for their useful discussion and encouragement.

I wish to thank Dr. Mitsumu Ejiri and Dr. Yoshihiro Tomikawa of NIPR for their valuable comments.

I wish to express my hearty thanks to Dr. Mariko Teramoto, Dr. Reiko Nomura, Ms. Claudia Martinez, Dr. Takehiro Hidemori, Dr. Takahiro Iino, Dr. Satoshi Kurita,

Mr. Daisuke Fukushima, Mr. Daishi Shukuya, and Mr. Hirotochi Uchino for their kind suggestions to my study and lifestyle.

I am grateful to Ms. Miho Ito, Ms. Minako Noguchi, Ms. Tomoko Suzuki, Ms. Hinako Komatsu, Ms. Risa Sakakibara, Mr. Daiki Watanabe, Mr. Taishi Tsuya, Mr. Ryota Takeuchi, Mr. Takashi Nakabo, Mr. Kai Shigematsu, Mr. Kohei Miyaji, Mr. Kazunari Matsunaga, Mr. Natsuo Kanda, Mr. Yoshihiro Nakamura, Mr. Hiroki Nagano, Mr. Ryusuke Kigawa, Mr. Takuya Mizoguchi, and EISCAT group members for my precious memories.

The Tromsø sodium LIDAR project is mainly supported by Special Funds for Education and Research (Energy Transport Processes in Geospace) from the Ministry of Education, Culture, Sports, Science, and Technology in Japan (MEXT), in collaboration with Nagoya University, Shinshu University, RIKEN, University of Tromsø, and the EISCAT Scientific Association.

I wish to thank K. Hocke for letting us use his Lomb-Scargle periodogram method routines. I also acknowledge the use of geomagnetic data from the World Data Centers for Geomagnetism in Kyoto, Japan, and Copenhagen, Denmark, and the Kp indices from GeoForschungsZentrum Potsdam (www.gfz-potsdam.de).

I am supported as a research fellow of the Japan Society for the Promotion of Science (JSPS) for Young Scientists. This research has been partly supported by MEXT through a Grant-in-Aid for JSPS fellows (25-3733), Scientific Research B (22403010, 23340144, 24310010, and 25287126), and Special Funds for Education and Research (Energy Transport Processes in Geospace). This research was also partially supported by MEXT through the Grant-in-Aid for Nagoya University Global COE Program, Quest for Fundamental Principles in the Universe: From Particles to the Solar System and the Cosmos, and Inter-University Upper atmosphere Global Observation NET-work (IUGONET). This research was also partly supported by the National Institute of Polar Research through General Collaboration Projects no. 24-10.

Finally, I would like to express my deepest thanks to my family for their continuous encouragement and especially to my parents and grandparents for me proceed with my studies in the graduate school.

Abstract

In this thesis, we have investigated two phenomena occurring in the polar mesosphere and lower thermosphere (MLT) region: upward propagation and dissipation of an atmospheric gravity wave (GW) and generation mechanisms of a sporadic sodium layer (SSL). GWs play an important role in momentum transportation from the lower atmosphere to the MLT region. Electric fields and auroral precipitation, originating from the magnetosphere, appear to play an important role in generation of SSLs at high latitudes. Thus the results of this thesis contribute to further understanding of the vertical coupling process between the atmosphere and magnetosphere/ionosphere.

For study of an upward propagating GW, an event observed from 16:30 to 24:30 UT on 29 October 2010 during a very geomagnetically quiet interval ($Kp \leq 1$) was analyzed. The sodium LIDAR observations conducted at Ramfjordmoen, Tromsø, Norway (69.6°N, 19.2°E) captured a clearly discernible GW signature. Derived vertical and horizontal wavelengths, maximum amplitude, apparent and intrinsic period, and horizontal phase velocity were about ~ 11.9 km, $\sim 1.38 \times 10^3$ km, ~ 15 K, 4 h, ~ 7.7 h, and ~ 96 m s⁻¹, respectively, between 80 and 95 km. Of particular interest is a temporal development of the uppermost altitude that the GW reached. The GW disappeared around 95 km height between 16:30 and 21:00 UT, while after 21:00 UT the GW appeared to propagate to higher altitudes (above 100 km). We have evaluated critical-level filtering, convective, and dynamic instabilities for dissipation using data obtained by the sodium LIDAR and a meteor radar. It is found that critical-level filtering did not occur, and the convective and dynamic instabilities occurred on some occasions. MF radar echo power showed significant enhancements between 18:00 and 21:00 UT, and an overturning feature of the sodium mixing ratio was observed between 18:00 and 21:30 UT above about 95 km. From these results, we have concluded that the GW was dissipated due to wave breaking caused by instabilities before 21:00 UT. We have also investigated the difference of the background atmosphere for the two intervals and would suggest that a probable cause

of the change in the GW propagation was due to the difference in the temperature gradient of the background atmosphere above 94 km.

We have quantitatively evaluated generation mechanisms of an SSL based on observational data obtained by multiple instruments at Ramfjordmoen. The sodium LIDAR observed an SSL at 21:18 UT on 22 January 2012. The SSL was observed for 18 min with a maximum sodium density of about $1.9 \times 10^{10} \text{ m}^{-3}$ at 93 km with a 1.1 km thickness. The EISCAT UHF radar observed a sporadic *E* layer (*Es* layer) above 90 km from 20:00 to 23:00 UT. After 20:00 UT, the *Es* layer gradually descended and reached 94 km at 21:18 UT when the SSL appeared at the same altitude. In this event, considering the abundance of sodium ions (10% or less), the *Es* layer could provide only about 21% or less of the sodium atoms to the SSL. We have investigated a temporal development of the normal sodium ion layer with consideration of chemical reactions and the effect of the (south-westward) electric field using observational values of the neutral temperature, electron density, horizontal neutral wind, and electric field. This calculation has shown that those processes, including contributions of the *Es* layer, would provide about 88% of the sodium atoms of the SSL. Effects of meteor absorption and auroral particle spattering appear to be less important. Therefore, we have concluded that the major source of the SSL was sodium ions in a normal sodium ion layer. Two processes—namely the downward transportation of sodium ions from a normal sodium ion layer due to the electric field, and the additional supply of sodium ions from the *Es* layer under relatively high electron density conditions (i.e., in the *Es* layer)—played a major role in generating the SSL in this event. Furthermore, we have found that the SSL was located in a lower temperature region, and that the temperature inside the SSL did not show any remarkable temperature enhancements.

Based on observational data, we have quantitatively discussed the effects of energy influx from the lower and the upper atmosphere by investigating gravity wave and SSL events under different geomagnetic conditions. To summarize, we propose that atmospheric instabilities and electric fields applied by the magnetosphere play an important role in the vertical coupling of the atmosphere in the polar MLT region.

Contents

List of Figures	ix
1 Introduction	1
1.1 Polar Earth's Atmosphere	1
1.1.1 Polar Neutral Atmosphere	1
1.1.2 Polar Ionosphere	3
1.1.3 Auroral Ionization	3
1.1.4 Sodium Layer	3
1.1.5 Atmospheric Stability	5
1.1.6 Charged Particle Motion	6
1.2 Atmospheric Gravity Wave	9
1.2.1 Linear Wave Theory	10
1.2.2 Propagation of GW	12
1.2.3 Critical-Level Filtering	12
1.2.4 Wave Dissipation	13
1.3 Sporadic Sodium Layer	14
1.3.1 Common Characteristics	14
1.3.2 Seasonal and Latitudinal Dependence	15
1.3.3 Generation Mechanisms	16
1.4 Purpose of This Thesis	18
2 Instruments	21
2.1 Sodium LIDAR	21
2.1.1 Measurement Principle	21
2.1.2 Temperature and Density Derivation Method	23
2.1.3 Error Calculation	27
2.1.4 Transmission and Receiving Units	27

2.2	EISCAT UHF Radar	29
2.3	Meteor Radar and MF Radar	30
2.4	Photometer	30
2.5	Digital Camera	31
3	Gravity Wave Dissipation in the Polar MLT Region	33
3.1	Observational Results	33
3.2	Discussion	38
3.2.1	Critical-Level Filtering	38
3.2.2	Convective and Dynamic Instabilities	44
3.2.3	GW Breaking	46
3.2.4	Possible Caused of the Difference of the GW Propagation	48
3.3	Summary	51
4	Generation Mechanisms of the Sporadic Sodium Layer During a Night of High Auroral Activity	53
4.1	Observational Results	53
4.2	Discussion	60
4.2.1	Production From the <i>Es</i> Layer	60
4.2.2	Concentration From a Sodium Ion Layer by Electric Field	62
4.2.3	Effect of Temperature	67
4.2.4	Meteor Absorption and Auroral Particle Spattering	68
4.2.5	The Effect of Advection	69
4.3	Summary	70
5	Summary and Conclusions	73
	References	77

List of Figures

1.1	Vertical atmosphere thermal and composition profiles at Tromsø at 12:00 UT (UT=LT-1) on 22 January 2012. The electric density profile is calculated with an ionospheric model, IRI-2012 model. The neutral temperature and particles as well as each neutral species are calculated with MSIS-E-90 model.	2
1.2	Schematic chemical reactions in the sodium layer. (<i>Plane, 2004</i>) . .	4
1.3	(a) The coordinate system applied the magnetic field in the direction of the z axis, (b) the coordinate system for the earth's magnetic field. I is inclination angle.	7
1.4	Height profile of the vertical ion speed at Tromsø, Norway for various electric field directions. Positive is upward (<i>Oyama et al., 2012</i>). . .	9
1.5	Schematic of air parcel oscillation in the atmosphere and relationship between group velocity C_G and wavenumber vector k . u and v are wind velocity along with the propagation direction and perpendicular to the propagation direction, respectively. T is the temperature. . . .	10
1.6	Sodium density profile obtained with airborne sodium LIDAR (<i>Gu et al., 1995</i>). An SSL appeared at about 94 km.	15
1.7	Electron and neutral sodium number densities (m^{-3}) as functions of altitude and time on 11 December 1997 (<i>Heinselman et al., 1998</i>). .	17
2.1	Energy level diagram of atomic Na (<i>She and Yu, 1995</i>)	22
2.2	Absorption cross section of sodium atom for three temperatures in background $v_R = 0$. f_a is frequency at D_{2a} peak. f_c is shifted several hundred MHz from the f_a	24
2.3	Ratio R_T versus the temperature T from 150 to 300 K in background wind $v_R = 0$	26

2.4	Layout of sodium D ₂ resonance light source for the sodium LIDAR at Tromø (<i>Nozawa et al.</i> , 2014).	28
2.5	Power spectrum of incoherent scatter radar. (from the pamphlet of the EISCAT Scientific Association)	29
2.6	Layout of the photometer. HF and DM are half mirror and dichroic mirror.	30
2.7	Images under conditions of (a) geomagnetic quiet condition, (b) high auroral activity, and (c) overcast.	31
3.1	(a) The neutral temperature variation from 16:30 UT 29 October to 00:30 UT on 30 October 2010. The warmer color indicates higher temperature and colder color indicates lower temperature. The original temporal and altitude resolution is 10 min and 1.2 km, respectively, and a 30 min running average is applied. (b) The corresponding error values of the temperature.	35
3.2	Periodograms as a function of altitude for the neutral temperature variation (a) between 16:30 to 24:30 UT, (b) between 16:30 and 20:30 UT, and (c) between 20:30 and 24:30 UT derived by the Lomb-Scargle method with an oversampling factor of 4.	36
3.3	The eastward (a) and northward (b) wind velocity obtained by meteor radar from 80 to 100 km from 16:30 to 24:30 UT on 29 October 2010. White dashed lines indicate zero wind velocity.	37
3.4	Eight hourly hodographs associated with the fitted eclipses are shown. Crosses denote data values associated with corresponding height values (in km). In the bottom right panel, superimposed hodographs with the fitted ellipse (thicker solid line) are presented. The estimated propagation direction is illustrated in each panel.	40
3.5	The local time maximum (a), phase difference between temperature and wind oscillation (b), and amplitude profile of the temperature and wind (c). The red and blue circles denote wind and temperature data, respectively. The period is 4 h. The double circles show values over the 99% significance level.	43
3.6	Variations of the square of Brunt-Väisälä frequencies (N^2) from 16:30 to 24:30 UT between 81 and 104 km. Negative N^2 regions are shown by blue filled squares.	44

-
- 3.7 (a) Variations of the Richardson number from 81 to 99 km between 16:30 and 24:30 UT on 29 October 2010. Negative values are shown by blue filled squares. (b) Error values of the Richardson number. 45
- 3.8 Variations of MF radar echo intensity from 80 to 105 km (in virtual height) between 16:30 and 24:30 UT on 29 October 2010. The black lines are contours of the neutral temperature (K) shown in Figure 3.1a. 46
- 3.9 The color contours show the sodium mixing ratio ($\times 10^{-11}$) on 29 October 2010. The black lines are contours of the potential temperature (K). 47
- 3.10 Altitude profiles of semidiurnal tidal amplitude (left) and local time of maximum (right). Diamonds and triangles denote eastward and northward components, respectively. 49
- 3.11 (a) Altitude profiles of the background temperature are compared for the two intervals between 16:30 and 21:00 UT and 21:00 and 24:30 UT. (b) Same as (a) but for the neutral density. (c) Ratios of neutral density (thick line) and pressure (thin line) between the two intervals. 50
- 4.1 Variations of the sodium density (a), the neutral temperature (b), and the electron density (c), the emission intensity (10 sec averaged values) of 427.8 nm (d) and 557.7 nm (e) from 16:00 UT on 22 January to 04:00 UT on 23 January are shown. The temporal and altitude resolution in (a) and (b) is 2 min and 0.5 km and in (c) is 30 sec and about 2.2 km, respectively. 55
- 4.2 (a) Variations of the sodium density from 20:00 to 24:00 UT on 22 January 2012 between 90 and 100 km are presented. Black dots denote altitudes of the maximum density of the SSL(s). (b) The maximum sodium density of the SSL(s). (c) The ratio of the maximum sodium density to the background sodium density at the same altitude. Red dots in (b) and (c) denote data values with the ratio greater than 2. In this study, we mainly focus on the SSL occurring for time intervals shown in the gray shade (i.e. 21:18 and 21:36 UT). 56

4.3	Altitude profiles of sodium density (red line) and neutral temperature (black line) from 21:14 UT to 21:37 UT every 1 min on 22 January 2012 are presented. These values are derived with a 15 sec temporal and 96 m height resolution. A 1 km running average is applied to the temperature profile. The gray shade shows standard deviations of the temperature data (1 sigma)	58
4.4	All-sky images obtained with the digital camera. The images obtained between 21:15 and 21:40 UT on 22 January 2012 are shown every 1 min, while the images between 20:50 and 20:55 UT and between 21:40 and 22:00 UT are shown every 5 min.	59
4.5	(a) Variations of altitudes of the maximum SSL (red line) and the <i>Es</i> layer for three different directions (square, closed circle, and triangle) of the EISCAT UHF radar measurements are compared. Shade area denotes the time interval when the SSL was seen. (b) Same in (a) except for the density. (c) Variations of the ratio of the maximum sodium density of the SSL to the maximum electron density in the <i>Es</i> layer (in the vertical position of the EISCAT measurements) are shown. (d) Comparison of column densities integrated between 92 and 97 km are shown.	61
4.6	Temporal variations of the direction (red line) and the strength (blue line) of the electric field derived by the EISCAT UHF radar from 18:00 to 24:00 UT on 22 January 2012 are shown.	63
4.7	Schematic drawing of circular reactions among Na, Na ⁺ , NaN ₂ ⁺ , NaO ⁺ , NaH ₂ O ⁺ , and NaCO ₂ ⁺	64
4.8	Temporal developments of sodium ions (a) and sodium atoms (b) are illustrated.	66
4.9	Comparison of sodium column density (red line) and mean temperature (black line) between 92 and 97 km every 1 min. The sodium density and the temperature are derived with 15 sec temporal and 96 m height resolution. The gray shading denotes standard deviations of the mean temperature.	68
4.10	Variations of meteor count from 12:00 to 24:00 UT on 22 January 2012 observed by the meteor radar at Tromsø are shown by the solid line. Dashed line denotes monthly averaged meteor counts over January 2012.	69

Chapter 1

Introduction

1.1 Polar Earth's Atmosphere

In this section, we describe the composition and the temperature profile of the atmosphere at high latitudes. The temperature profile is dependent on the balance of absorption and radiation cooling of solar radiation. The neutral atmosphere is approximately constant in composition because of eddy diffusion below 100 km. Since the molecule diffusion becomes dominant, the constituents begin to separate due to their masses above 100 km. This boundary is called turbopause. The neutral atmosphere is characterized by temperature profile as shown in Figure 1.1. On the other hand, the earth's atmosphere is partially ionized by solar radiation during daytime. This region where charged particles exist is called the ionosphere. The neutral particles and charged particles interact through collisions with each other in the ionosphere.

Figure 1.1 shows vertical profiles of the temperature and also shows the density of neutral gases and electron density. These parameters are obtained by Mass Spectrometer Incoherent Scatter (MSIS-E-90) atmosphere model for the temperature and neutral gases and the International Reference Ionosphere 2012 (IRI-2012) model for the ionized particles (*Hedin, 1991; Bilitza, 2002*).

1.1.1 Polar Neutral Atmosphere

The troposphere extends from the earth's surface to about 10 km in the polar region where the temperature decreases with altitude. Since temperature lapse rate is about -7 K km^{-1} , which is nearly equal to the dry-adiabatic lapse rate of about -10 K km^{-1} , the troposphere frequently becomes unstable. The atmospheric instability in

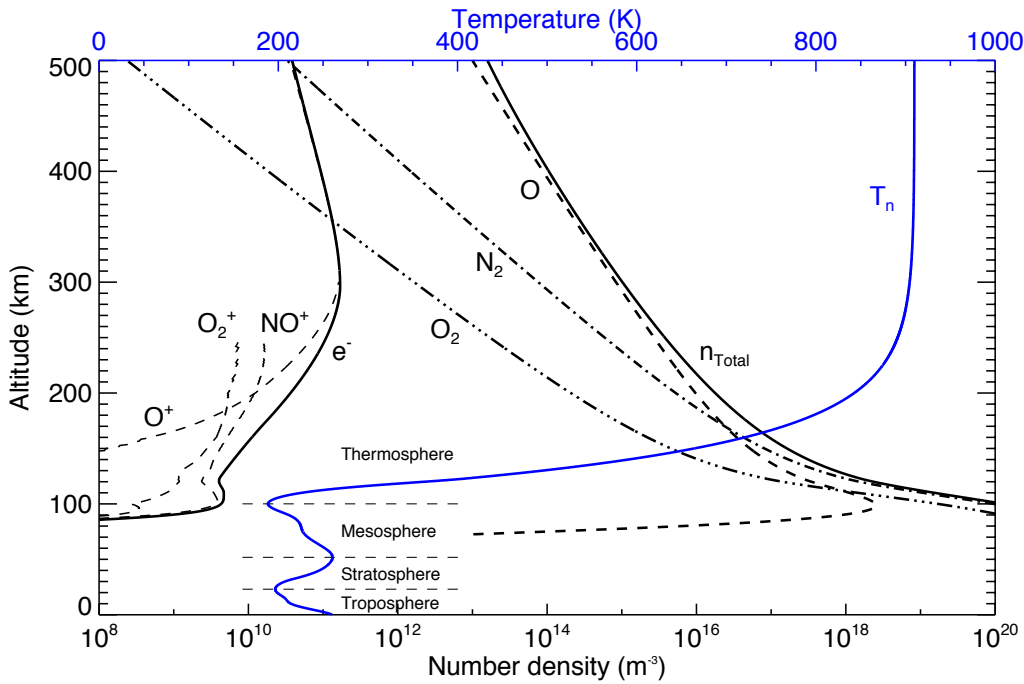


Figure 1.1 Vertical atmosphere thermal and composition profiles at Tromsø at 12:00 UT (UT=LT-1) on 22 January 2012. The electric density profile is calculated with an ionospheric model, IRI-2012 model. The neutral temperature and particles as well as each neutral species are calculated with MSIS-E-90 model.

the troposphere may generate atmospheric gravity waves that propagate to the upper atmosphere.

The stratosphere is from about 10 km to about 50 km with a temperature lapse rate of 3.3 K km^{-1} . The absorption of solar ultra violet (UV) radiation by ozone molecules in the stratosphere plays a role in atmospheric tidal wave generation.

The mesosphere extends from about 50 km to the mesopause, which is the boundary surface between the mesosphere and thermosphere. Since radiative cooling is dominant in the mesosphere, temperature profile has a negative temperature gradient with a lapse rate of about -3.5 K km^{-1} . Although the temperature gradient is negative in the mesosphere, the atmosphere is almost stable. However, GWs and tidal waves often cause the atmospheric instability due to their release of momentum flux and/or amplitude in the mesosphere. The temperature and altitude of the mesopause experience seasonal variation due to meridional circulation. This seasonal variation is stronger at high latitudes than at lower latitudes. Based on satellite observation, *Xu et al.* (2007) showed that the mesopause is high (97 km) and warm (180 K) in winter and low (85 km) and cold (140 K) in summer at polar latitudes.

The temperature exponentially increases in the thermosphere because of absorption of UV and extreme ultra violet (EUV) radiation from the sun. The neutral temperature in the thermosphere first increases with increasing altitude up to a maximum (1000-2000 K), and then it becomes constant.

1.1.2 Polar Ionosphere

The solar radiation is responsible for production of plasma. Above about 60 km, less than 1% of the atmosphere is ionized by solar radiation. This region where the ionized particles exist is called the ionosphere. The ionosphere is characterized as the *D*, *E*, and *F* region by the vertical electron profile. The atomic hydrogen Lyman α is a dominant source of ionization for photoionization of NO in the *D* region from about 60 km to about 90 km. The *D* region essentially vanishes during the night. The height region from about 90 km to about 130 km is called the *E* region. NO^+ and O_2^+ ionized from N_2 , O_2 , and O are major ions in the *E* region. The region above the *E* region is termed the *F* region.

1.1.3 Auroral Ionization

Auroral precipitation provides the high-energy electrons in the polar upper atmosphere. The altitudes at which electron energy is deposited are dependent on energy, neutral particle densities, and pitch angles. *Rees* (1963) shows distribution of energy deposition of auroral particles. The peak deposition altitude for 5.60 and 40 keV are about 120 and 90 km, respectively. Thus, the energies of auroral electrons are much greater than ionization energies of N_2 and O_2 . Therefore, the auroral precipitation plays a role in the ionization source at high latitudes during nighttime.

The auroral electrons primarily ionize N_2^+ and O_2^+ . However, N_2^+ and O_2^+ are neutralized quickly and provide NO^+ and metallic ions because of their rapid chemical reactions. The number density of NO is drastically affected by auroral precipitation (*Siskind et al.*, 1998) and metallic ions provided by auroral precipitation are a major formational component for *Es* layers (*Nygrén et al.*, 1990).

1.1.4 Sodium Layer

The existence of sodium atoms in the upper atmosphere has been known since the mid-1930s through the spectroscopic observation of sodium D line enhancement (*Chapman*, 1939). Based on radiative transfer theory, *Donahue et al.* (1956) deduced

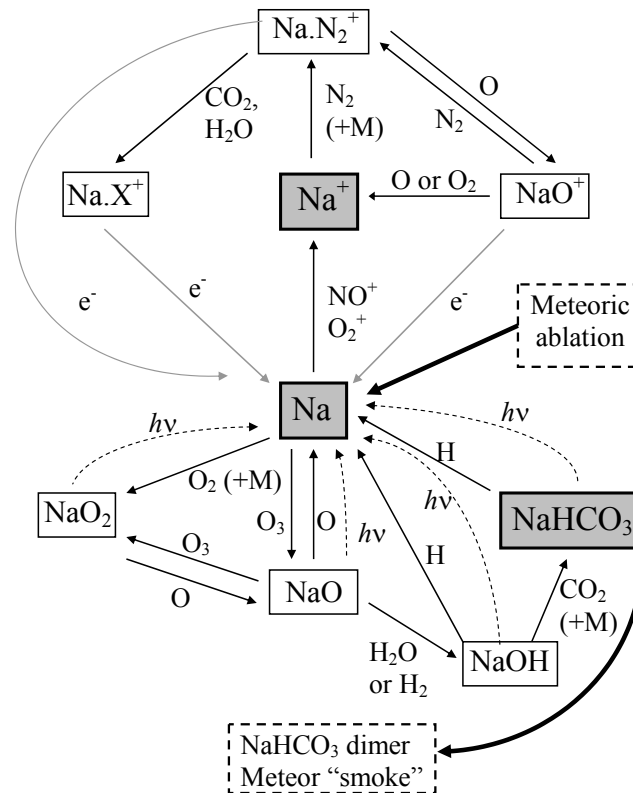


Figure 1.2 Schematic chemical reactions in the sodium layer. (*Plane, 2004*)

the sodium density profile by the integrated light obtained from twilight scattering. The laser radar (so-called LIDAR) technique has been developed since the late 1960s and drastically improved the understanding of properties of sodium layers in detail (*Bowman et al., 1969*). The sodium layer has been investigated by using sodium LIDAR techniques. In this section, the fundamentals of the sodium layer are described.

The sodium layer is sustained by balance of meteor absorption, chemical reaction, and diffusion. Chemical reactions are particularly important for formation of the sodium layer. The schematic of the sodium chemistries in the sodium layer is shown in Figure 1.2 (*Plane, 2004*). In the bottom side of the sodium layer, sodium-bearing molecules work as a reservoir of atomic sodium. A sodium atom becomes the stable reservoir NaHCO₃ by a series of steps. As shown in Figure 1.2, species such as NaO, NaOH, and NaHCO₃ are converted back to sodium atoms by reaction with O and H. On the other hand, ion chemistry predominates in the topside of the sodium layer. A sodium ion works as a reservoir of a sodium atom. Sodium atoms are ionized mostly by charge exchange with ambient NO⁺ and O₂⁺ ions, with a small contribution from solar photoionization. Sodium ions become converted to the NaN₂⁺ ions with N₂ and

third body M ($M = \text{N}_2$ or O_2). The NaN_2^+ ion is neutralized with an electron directly or by forming clusters that undergo dissociative electron recombination (*Plane, 2004*).

Since these chemical processes are sensitive to the temperature, the peak altitude of the sodium layer and column sodium density exhibit a seasonal variation. The peak altitude of the sodium layer varies between about 88 and 92 km, with the highest peak altitude occurring during summer (*Plane, 1998; Gibson and Sandford, 1971; Kuruzawa and von Zahn, 1990*). Although the sodium column density varies by up to a factor of 10 depending on time and location, the mean sodium column density is $1 \times 10^{13} \text{ m}^{-2}$ in summer and $5 \times 10^{14} \text{ m}^{-2}$ in winter in the polar region (*Kuruzawa and von Zahn, 1990*). This seasonal variation peaks at high latitudes and lessens at low latitudes. A ratio of the sodium column density in winter to in summer is about 1.3 at low latitudes, whereas the ratio is about 3 at mid latitudes and more than 10 at high latitudes (*Simonich et al., 1979; Plane et al., 1999; Kuruzawa and von Zahn, 1990*).

1.1.5 Atmospheric Stability

An air parcel oscillates in a stable atmosphere when it moves from its equilibrium position. The frequency of the oscillation is useful as the parameter of atmospheric instability. This frequency is called the Brunt-Väisälä frequency and is expressed as

$$N^2 = \frac{g}{\theta} \frac{d\theta}{dz} = \frac{g}{T} \left(\frac{dT}{dz} + \Gamma_d \right) \quad (1.1)$$

where N is the Brunt-Väisälä frequency, g is the acceleration of gravity, θ is the potential temperature, T is the temperature, and Γ_d is the dry-adiabatic lapse rate. If the N^2 is positive, the air parcel can oscillate at the radian frequency N . However, if the N^2 is negative, the air parcel cannot return to its equilibrium position and the ambient atmosphere becomes convectively unstable. Since the Γ_d is approximately constant with altitude, the N^2 strongly depends on the temperature gradient.

The wind shear also generates an atmospheric instability. The ratio of Brunt-Väisälä frequency to wind shear is often used to evaluate atmospheric stability. The square of the ratio is called Richardson number Ri and is expressed as

$$Ri = \frac{N^2}{\left(\frac{dU}{dz}\right)^2} \quad (1.2)$$

where U is the horizontal wind velocity. If Ri becomes less than 0.25, the wind shears are strong enough to generate the atmospheric instability. This instability is called dynamical or Kelvin-Helmholtz instability (*Drazin, 1958*).

1.1.6 Charged Particle Motion

The plasma motion in the ionosphere is written by the motion equation for a charged particle, which is given as

$$nm_j \frac{d\mathbf{v}_j}{dt} = -k_B T_j \nabla n + nm_j \mathbf{g} + nq_j (\mathbf{E} + \mathbf{v}_j \times \mathbf{B}) - nm_j \nu_{in} (\mathbf{v}_j - \mathbf{u}_n) \quad (1.3)$$

where n is the plasma density, k_B is the Boltzmann constant, g is the acceleration of gravity, q_j is the electric charge, \mathbf{E} is the electric field, \mathbf{B} is the earth's magnetic field, ν_{in} is ion-neutral collision frequency, \mathbf{u}_n is the velocity of neutral wind, and \mathbf{v}_j , T_j , and m_j are velocity, temperature, and mass of an electron or an ion, respectively. The momentum equation consists of the pressure gradient term, the gravity term, the Lorentz term, and the friction term, respectively. In this thesis, we focus on the ion motion.

The ion-neutral collision frequency plays an important role in the kinetic energy transportation between ion and neutral particles in the partially ionized plasma. An approximate formula for the ion-neutral collision frequency is given by

$$\nu_{in} = 2.6 \times 10^{-15} (n_n + n_i) A_n^{-1/2} \quad (1.4)$$

where n_n and n_i are neutral and ion density, and A_n is mean neutral molecule mass from equation (2.29) by *Kelley (2009)*.

The steady state of equation (1.3) for an ion is written as

$$-k_B T_i \nabla n + nm_i \mathbf{g} + nq_i (\mathbf{E} + \mathbf{v}_i \times \mathbf{B}) - nm_i \nu_{in} (\mathbf{v}_i - \mathbf{u}_n) = 0 \quad (1.5)$$

Solving (1.5) for \mathbf{v}_i , we find

$$\mathbf{v}_i = \mathbf{u}_n + D_i \left(\frac{\mathbf{g}}{H_i} - \frac{\nabla n}{n} \right) + \frac{q_i}{m_i \nu_{in}} (\mathbf{E} + \mathbf{v}_i \times \mathbf{B}) \quad (1.6)$$

where $D_i (= k_B T_i m_i^{-1} \nu_{in}^{-1})$ is the diffusion coefficient for ion and $H_i (= k_B T_i m_i^{-1} g^{-1})$ is the scale height for ions. In the lower thermosphere, the ion-neutral frequency increases exponentially with decreasing altitudes: about 100 Hz at 130 km and about

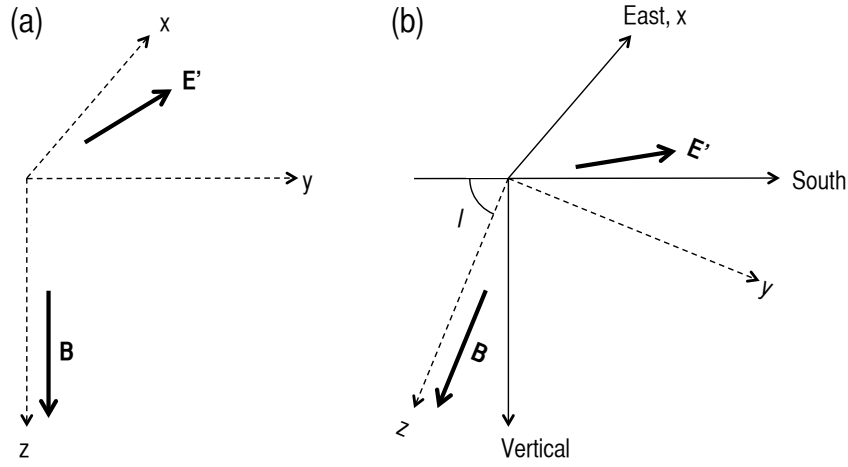


Figure 1.3 (a) The coordinate system applied the magnetic field in the direction of the z axis, (b) the coordinate system for the earth's magnetic field. I is inclination angle.

5000 Hz at 100 km. Since D_i is correspondingly small in the lower thermosphere, the pressure gradient and gravity terms are neglected in this thesis. The equation (1.6) is rewritten as

$$\mathbf{v}_i = \mathbf{u}_n + \frac{q_i}{m_i \nu_{in}} (\mathbf{E} + \mathbf{v}_i \times \mathbf{B}) \quad (1.7)$$

By adding $\pm \mathbf{u}_n \times \mathbf{B}$, we get

$$\begin{aligned} \mathbf{v}_i - \mathbf{u}_n &= \frac{q_i}{m_i \nu_{in}} \mathbf{E} + \frac{q_i}{m_i \nu_{in}} (\mathbf{u}_n \times \mathbf{B}) + \frac{q_i}{m_i \nu_{in}} (\mathbf{v}_i \times \mathbf{B}) - \frac{q_i}{m_i \nu_{in}} (\mathbf{u}_n \times \mathbf{B}) \\ &= \frac{q_i}{m_i \nu_{in}} (\mathbf{E} + \mathbf{u}_n \times \mathbf{B}) + \frac{q_i}{m_i \nu_{in}} \{(\mathbf{v}_i - \mathbf{u}_n) \times \mathbf{B}\} \end{aligned} \quad (1.8)$$

The electric field and ion velocity measured in a reference frame moving with the neutral wind is expressed as

$$\mathbf{v}'_i = \mathbf{v}_i - \mathbf{u}_n \quad (1.9)$$

$$\mathbf{E}' = \mathbf{E} + \mathbf{u}_n \times \mathbf{B} \quad (1.10)$$

Therefore the simplified motion equation for an ion is written as

$$\mathbf{v}'_i = \frac{q_i}{m_i \nu_{in}} (\mathbf{E}' + \mathbf{v}'_i \times \mathbf{B}) \quad (1.11)$$

Here we consider a coordinate to which magnetic field \mathbf{B} is applied in the direction of the z axis as shown in Figure 1.3 (a). Solving (1.11) for the x , y , and z component,

we get

$$v'_x = \frac{q_i}{m_i} \frac{v_{in}}{v_{in}^2 + \Omega_i^2} E'_x + \frac{q_i}{m_i} \frac{\Omega_i}{v_{in}^2 + \Omega_i^2} E'_y \quad (1.12)$$

$$v'_y = -\frac{q_i}{m_i} \frac{\Omega_i}{v_{in}^2 + \Omega_i^2} E'_x + \frac{q_i}{m_i} \frac{v_{in}}{v_{in}^2 + \Omega_i^2} E'_y \quad (1.13)$$

$$v'_z = \frac{q_i}{m_i v_{in}} E'_z \quad (1.14)$$

where the Ω_i is ion gyro frequency ($=q_i B/m_i$). Since the conductivity along with \mathbf{B} is high, the electric field \mathbf{E} is assumed to be perpendicular to \mathbf{B} . Thus, E'_z is assumed to be zero.

The earth's magnetic field is inclined southward in the Northern Hemisphere. Figure 1.3 (b) shows a comparison of (a) with the geographical coordinate. The I is the inclination angle of the earth's magnetic field. The v'_e , v'_s , v'_v , E'_x , and E'_y are

$$v'_e = v'_x \quad (1.15)$$

$$v'_s = v'_y \sin I \quad (1.16)$$

$$v'_v = v'_y \cos I \quad (1.17)$$

$$E'_x = E_e + (u_v \cos I + u_s \sin I) B \quad (1.18)$$

$$E'_y = E_s \sin I - u_e B \quad (1.19)$$

Thus,

$$v_e = \frac{v_{in} \Omega_i}{v_{in}^2 + \Omega_i^2} \left(\frac{E_e}{B} + u_v \cos I + u_s \sin I \right) + \frac{\Omega_i^2}{v_{in}^2 + \Omega_i^2} \frac{E_s}{B} \sin I + \left(1 - \frac{\Omega_i^2}{v_{in}^2 + \Omega_i^2} \right) u_e \quad (1.20)$$

$$v_s = \frac{v_{in} \Omega_i}{v_{in}^2 + \Omega_i^2} \left(\frac{E_s}{B} \sin I - u_e \right) \sin I - \frac{\Omega_i^2}{v_{in}^2 + \Omega_i^2} \left(\frac{E_e}{B} + u_v \cos I \right) \sin I + \left(1 - \frac{\Omega_i^2 \sin^2 I}{v_{in}^2 + \Omega_i^2} \right) u_s \quad (1.21)$$

$$v_v = \frac{v_{in} \Omega_i}{v_{in}^2 + \Omega_i^2} \left(\frac{E_s}{B} \sin I - u_e \right) \cos I - \frac{\Omega_i^2}{v_{in}^2 + \Omega_i^2} \left(\frac{E_e}{B} + u_s \sin I \right) \cos I + \left(1 - \frac{\Omega_i^2 \cos^2 I}{v_{in}^2 + \Omega_i^2} \right) u_v \quad (1.22)$$

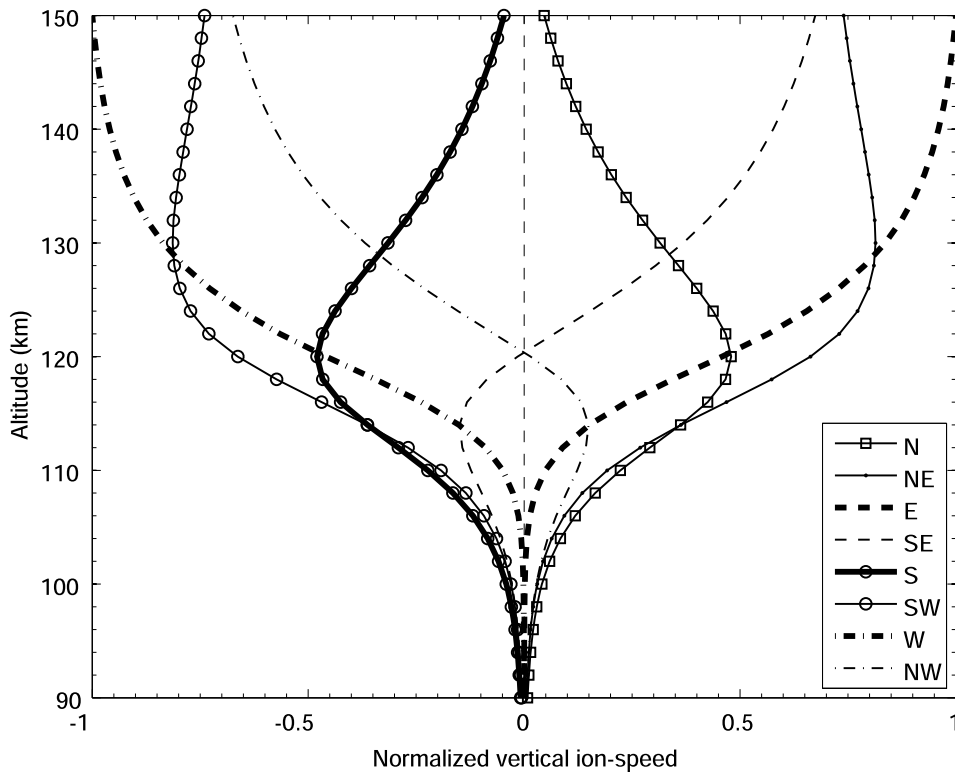


Figure 1.4 Height profile of the vertical ion speed at Tromsø, Norway for various electric field directions. Positive is upward (Oyama *et al.*, 2012).

Therefore, charged particles are forced downward by the horizontal electric field and neutral wind because of the magnetic field inclination.

Figure 1.4 shows height profile of the vertical ion speed (Oyama *et al.*, 2012). Below 120 km, from south-eastward to westward electric field makes downward ion motion. Kirkwood and von Zahn (1991) proposed a possibility for concentration of metallic ions due to the downward ion motion by the electric fields.

1.2 Atmospheric Gravity Wave

The earth's atmosphere is continuously disturbed by a number of sources. Atmospheric waves generated by these disturbances propagate in the atmosphere and transport their momentum flux. These waves are characterized in their oscillation period and called sound wave, atmospheric gravity wave (GW), tidal wave, and planetary wave. The typical oscillation frequency of GWs is from the Brunt-Väisälä frequency (corresponds to oscillation period of about 5 min in the mesopause region) to the inertia frequency

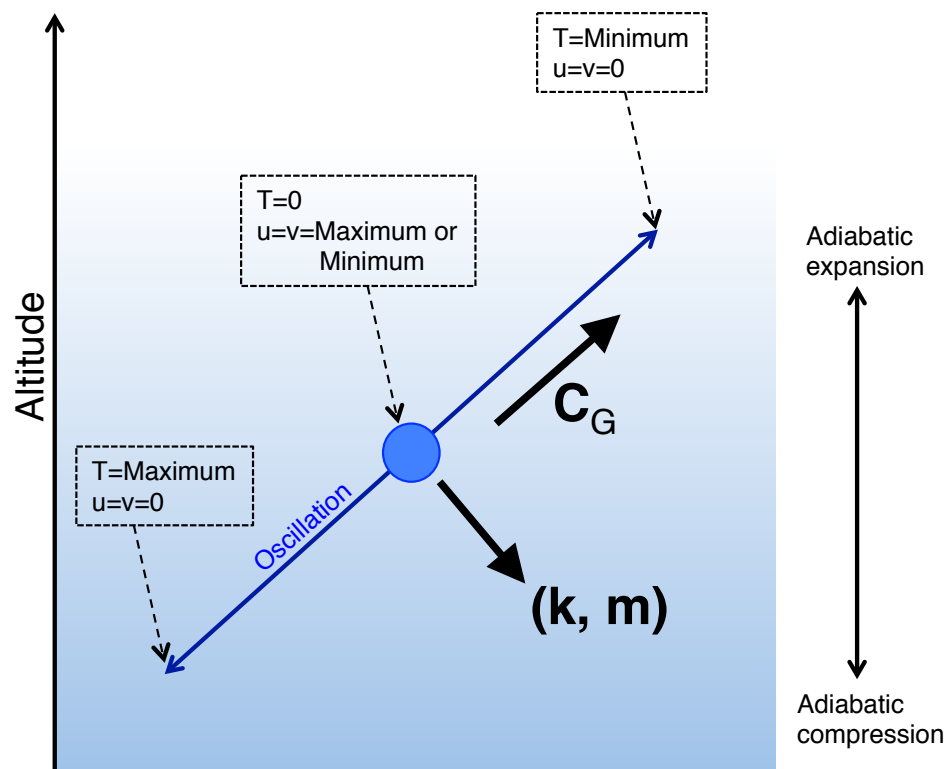


Figure 1.5 Schematic of air parcel oscillation in the atmosphere and relationship between group velocity C_G and wavenumber vector k . u and v are wind velocity along with the propagation direction and perpendicular to the propagation direction, respectively. T is the temperature.

(corresponding to oscillation period of 12.8 hours at Tromsø) in the mesosphere and lower thermosphere (MLT) region.

GWs mainly are generated in the troposphere and propagate upward through the stratosphere and lower mesosphere. GWs may release their momentum flux, which causes acceleration or deceleration of mean wind around the mesopause. This release of the momentum flux contributes to the acceleration of the meridional mean circulation of middle atmosphere.

1.2.1 Linear Wave Theory

Figure 1.5 shows air parcel movement by upward propagation of a GW in hydrostatic equilibrium. The fundamental equations for GWs are derived from motion equation, entropy equation, ideal gas law, perturbation equation and continuity equation as

follows:

$$-i\sigma\tilde{u} - f\tilde{v} + igHk\tilde{p} = 0 \quad (1.23)$$

$$-i\sigma\tilde{v} + f\tilde{u} = 0 \quad (1.24)$$

$$-i\sigma g\tilde{\rho} + gH \left(im - \frac{1}{2H} \right) \tilde{p} = 0 \quad (1.25)$$

$$-ik\tilde{u} + \left(im - \frac{1}{2H} \right) \tilde{w} - i\sigma\tilde{\rho} = 0 \quad (1.26)$$

$$\frac{N^2}{g}\tilde{w} - i\frac{\sigma}{\gamma}\tilde{p} + i\sigma\tilde{\rho} = 0 \quad (1.27)$$

$$\frac{N^2}{g}\tilde{w} - i\sigma\tilde{\theta} = 0 \quad (1.28)$$

where \tilde{u} and \tilde{v} are wind velocity amplitudes parallel and perpendicular to propagation direction, respectively, \tilde{p} is the amplitude of pressure, $\tilde{\theta}$ is the amplitude of potential temperature, i is the imaginary unit, σ is intrinsic frequency ($\sigma = \omega - Uk$), ω is grand-based frequency, f is the inertia frequency, g is the acceleration of gravity, H is the scale height, k and m are horizontal and vertical wavenumbers, respectively. The equations from (1.23) to (1.26) provide

$$\tilde{w} = -\frac{\sigma^2 - f^2}{N^2 - \sigma^2} \frac{m + \frac{i}{H} \left(\frac{1}{2} - \frac{1}{\gamma} \right)}{k} \tilde{u} \quad (1.29)$$

where \tilde{w} is the vertical wind amplitude. This equation is called the dispersion relation, which defines the relationship between the wavenumber and frequency. For a GW, which has a short vertical wavelength of less than about 10 km, the dispersion relation, equation (1.26), and equation (1.28) are expressed as

$$m^2 \approx \frac{N^2 - \sigma^2}{\sigma^2 - f^2} k^2 \quad (1.30)$$

$$\tilde{w} \approx -\frac{k}{m} \tilde{u} \quad (1.31)$$

$$\tilde{\theta} \approx -i \frac{N}{g\sigma} \frac{k}{m} \tilde{u} \quad (1.32)$$

These equations indicate three basic behaviors of a GW. First, the intrinsic frequency confined to the range $N > \sigma > f$ can propagate upward. Second, oscillation direction is in a direction perpendicular to the k vector. This means that an upward-

propagating GW draws an ellipse in a clockwise fashion in the Northern Hemisphere. Third, the phase of a GW in the temperature should precede by 90 degrees that of the wind along the propagation direction.

1.2.2 Propagation of GW

GWs are composed of some wave packets. The wave packet motion is expressed by group velocity \mathbf{C}_G .

$$\mathbf{C}_G = \frac{\partial \sigma}{\partial \mathbf{k}} = \left(\frac{\partial \sigma}{\partial k}, \frac{\partial \sigma}{\partial m} \right) \quad (1.33)$$

Substituting the dispersion relation (1.30) into the equation (1.33), the horizontal and vertical group velocities are

$$C_{G_x} = km^2 \frac{(k^2 N^2 + m^2 f^2)^{-1/2}}{(k^2 + m^2)^{3/2}} (N^2 - f^2) \quad (1.34)$$

$$C_{G_z} = -mk^2 \frac{(k^2 N^2 + m^2 f^2)^{-1/2}}{(k^2 + m^2)^{3/2}} (N^2 - f^2) \quad (1.35)$$

The equations (1.34) and (1.35) show the notable characteristic of upward-propagating GWs. The horizontal phase velocity is in the same direction of the horizontal group velocity. However, the vertical phase velocity is in the opposite direction of the vertical group velocity. Therefore, the downward phase propagation denotes the upward-propagating GW.

1.2.3 Critical-Level Filtering

The deformation of the dispersion relation (1.30) is given as

$$m^2 = \frac{m^2 N^2 + k^2 f^2}{\sigma^2} - k^2 = \frac{m^2 N^2 + k^2 f^2}{(c - U)^2 k^2} - k^2 \quad (1.36)$$

where c is phase velocity and U is background wind velocity. If the GW propagates upward in background wind U , which has a positive gradient with the altitude, the GW reaches the altitude where $c = U$. The altitude is called the critical level. The vertical wavenumber becomes infinity at the critical level. Thus, the GW cannot propagate further altitude above the critical level.

1.2.4 Wave Dissipation

GWs propagating upward usually dissipate in the upper mesosphere and (partly) lower thermosphere (MLT) region, and their energy and momentum release through dissipation play a dominant role in the zonal mean wind reversal as well as in meridional circulation in the upper mesosphere (*Lindzen, 1981; Holton, 1982*). A GW propagation depends on background thermodynamics and wind dynamics (*Fritts and Alexander, 2003*). Dissipation of GWs mainly results from wave breaking and instabilities, wave-wave and wave mean flow interactions, and radiative damping (*Lu et al., 2009*). GWs that are not otherwise attenuated by ambient turbulence, wave-wave interactions, and the like will eventually break down owing to instabilities that the waves themselves generate (*Hecht et al., 1997*). Instabilities generated by GWs may be convective and/or dynamical (shear) instabilities. There is an issue concerning how GWs can penetrate into the thermosphere without having significant dissipation in the mesosphere. Some model studies pointed out that GWs can propagate into the thermosphere (e.g., *Vadas and Fritts, 2004; Fritts and Vadas, 2008*). Therefore, the investigation of upward-propagating GWs and their dissipation process are essentially needed to understand the global circulation in the upper mesosphere and lower thermosphere.

Conditions of upward propagation of GWs through the mesosphere into the thermosphere have not yet been investigated fully based on observations. In particular, there are fewer studies conducted in the polar MLT region, which has another energy source than the magnetosphere, than those conducted at middle and low latitudes. It is important to understand the relationship between the upward propagation of GWs and background thermo-dynamics/wind dynamics in the polar MLT region for a further understanding of the lower thermosphere dynamics, variability of the ionosphere, and the magnetosphere-ionosphere-thermosphere coupling process. Dynamical and convective instabilities are two mechanisms that contribute significantly to the dissipation of larger scale motions and the generation of turbulence in the middle atmosphere (*Fritts and Rastogi, 1985*). Recent observations using an OH airglow imager and a sodium LIDAR showed that wave breaking occurred and the subsequent appearance of ripples was related to dynamical (or Kelvin-Helmholtz) instabilities (*Li et al., 2005; Hecht et al., 2005*). *Hodges Jr. (1967)* pointed out that GWs can produce convective instabilities in thin layers that propagate with the waves and then generate turbulence. *Hodges Jr. (1967)* also stated that wind shears, which are strong enough to produce regions in which the Richardson number (Ri) is less than 1, often exist and that these

may possibly be important in sustaining turbulence. One of the dynamical instabilities in the atmosphere is the Kelvin-Helmholtz (KH) instability, which sets in when the Richardson number of the wind profile is less than 0.25 (*Drazin, 1958*). Because KH instabilities can achieve large amplitudes and kinetic energies, they can have a number of important effects, including the excitation of other wave motions, the local transport of momentum and energy, and the generation of turbulence and diffusion (*Fritts and Rastogi, 1985*). On the other hand, the most obvious regions of convective instability occur in the upper stratosphere, mesosphere, and lower thermosphere due to the growth of wave amplitude with height increase. The depths of these layers are typically about 3-10 km in the MLT region, suggesting that dominant vertical wavelengths are more than twice these values (*Fritts and Rastogi, 1985*). Based on wind observations by the middle- and upper-atmosphere (MU) radar at Shigaraki (34.9°N, 136.1°E) and the temperature from the COSPAR International Reference Atmosphere (1972) model, *Yamamoto et al. (1987)* found a monochromatic inertia gravity wave and showed clear evidence that gravity waves were saturated, induced the shear or convective instabilities, and generated turbulence in the mesosphere. *Li et al. (2005)* reported the breakdown of a high-frequency quasi-monochromatic gravity wave into small-scale ripples based on OH airglow data obtained in Maui, Hawaii. They concluded that the breakdown was caused by dynamical (or KH) instabilities. Although numerous studies have been carried out, there are not many studies published that deal with dissipation of GWs of longer periods ($\geq \sim 4$ h) based on observational data of temperature and wind.

1.3 Sporadic Sodium Layer

A sporadic sodium layer (SSL) is a dense thin sodium layer superposed on a normal sodium layer as shown in Figure 1.6 and was first reported by *Clemesha et al. (1978)* in São Paulo, Brazil (23°S, 46°W). This interesting phenomenon has been investigated for more than three decades. The clarified features of SSLs by previous studies are described below.

1.3.1 Common Characteristics

SSLs have three common characteristics. The first is vertical and horizontal distributions. SSLs typically have a thin vertical extent with a full-width of half maximum (FWHM) of 1-2 km and have a wide horizontal extent. The typical horizontal extent

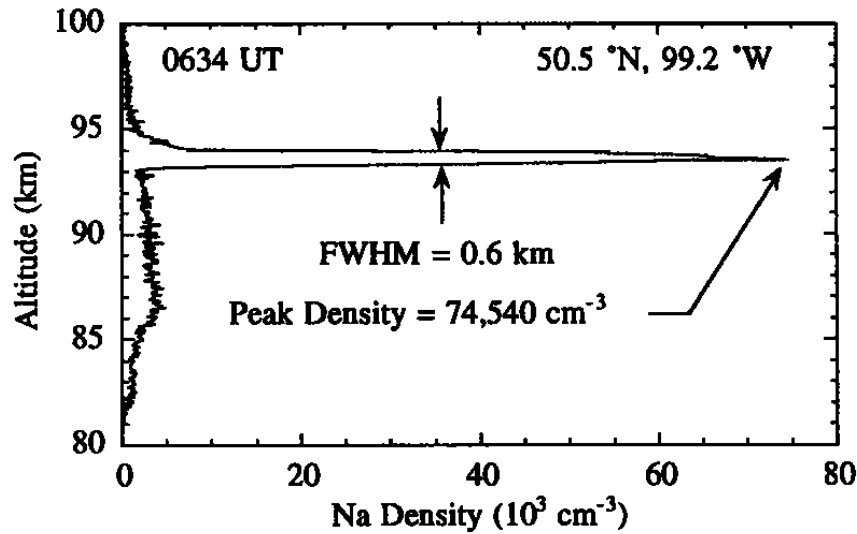


Figure 1.6 Sodium density profile obtained with airborne sodium LIDAR (*Gu et al.*, 1995). An SSL appeared at about 94 km.

is between about 100 and 300 km (*Batista et al.*, 1991; *Fan et al.*, 2007). In some rare cases, an SSL that extended farther than 1000 km was observed by airborne LIDAR (*Kane et al.*, 1991). The second characteristic is the large ratio of peak density of SSLs to background normal sodium density at the same altitude. SSLs have concentrations between about 3 and 10 times higher than that of the background normal sodium layer (cf., *Nagasawa and Abo*, 1995). For example, typical sodium density around 95 km in winter is about $3 \times 10^9 \text{ m}^{-3}$, and typical SSLs may have concentrations of about $2 \times 10^{10} \text{ m}^{-3}$ at the same altitude. SSLs with concentrations greater than $7.4 \times 10^{10} \text{ m}^{-3}$ were observed during ANLC-93 by *Gu et al.* (1995). The third characteristic is rapid growth and short lifetime. SSLs typically reach their maximum concentration in an interval between 2 and 20 min and last for a few tens of minutes to several hours.

1.3.2 Seasonal and Latitudinal Dependence

The sodium density and its peak density in a sodium layer between 80-110 km show a seasonal dependence. The peak altitude of the sodium layer is located at about 87 km in winter and about 92 km in summer at high latitudes (*Gibson and Sandford*, 1971). Since SSLs are superimposed on a background normal layer, appearance altitudes and their peak sodium densities of SSLs have a seasonal dependence. Far more SSLs were seen above 100 km in winter than in summer at high latitudes, although

peak sodium densities in these SSLs were much lower (about $1 \times 10^9 \text{ m}^{-3}$) than those found at about 95 km (*Hansen and von Zahn, 1990*). *Hansen and von Zahn (1990)* also presented that the occurrence rate of SSLs seen at Andøya has a local time dependence, with all their events occurring between 2000 and 0200 LT, with a maximum occurrence at 2200 LT. SSLs are frequently observed at low and high latitudes but rarely observed at mid latitudes (*Senft et al., 1989; Clemesha et al., 1998*). *Nagasawa and Abo (1995)* have argued that SSLs were observed frequently at mid latitudes (Tokyo) as well. Tokyo is located at low latitudes in the geomagnetic coordinate, implying that a geomagnetic effect would play a role in generating SSLs (to some extent).

1.3.3 Generation Mechanisms

Generation mechanisms of SSLs have been investigated and discussed for more than three decades, but are still an open question. Proposed mechanisms are as follows: direct meteor deposition, release from aerosol particles, chemical reduction of appropriate metal compounds, redistribution of existing atoms, and recombination of ions (*Clemesha et al., 1999*). There may be two candidates for the source of sodium atoms: one is neutral sodium bearing molecules/atoms, and the other is sodium ions. For example, the altitudinal redistribution of sodium atoms has been proposed as one of major generation mechanisms of SSLs by *Clemesha (1995)*.

In the first report of an SSL, *Clemesha et al. (1978)* suggested that the origin of the excess sodium atoms must be due to meteor deposition, and in a later paper *Clemesha et al. (1988)* suggested a mechanism whereby an initially thick layer caused by meteor deposition could be converted into a thin layer by wind shear. This mechanism requires a large meteor and/or a large meteor shower that have a total mass greater than 100 kg, but it is believed that occurrence of such an meteor event is rare (*Keay and Cepelcha, 1994*).

By using model calculations, *Plane (2004)* proposed that sodium atoms in the topside of a normal sodium layer are in equilibrium with sodium ions through several chemical reactions. Among sodium compound ions, NaN_2^+ contributes largely to generate sodium atoms. Since chemical reactions of NaN_2^+ are sensitive to the background temperature, investigation of the background temperature is also important for understanding of the generation mechanisms. Chemical reactions show an inverse correlation between sodium atom production and the background temperature (*Plane, 2004*). On the other hand, from an observational side, *Zhou et al. (1993)* argued that a

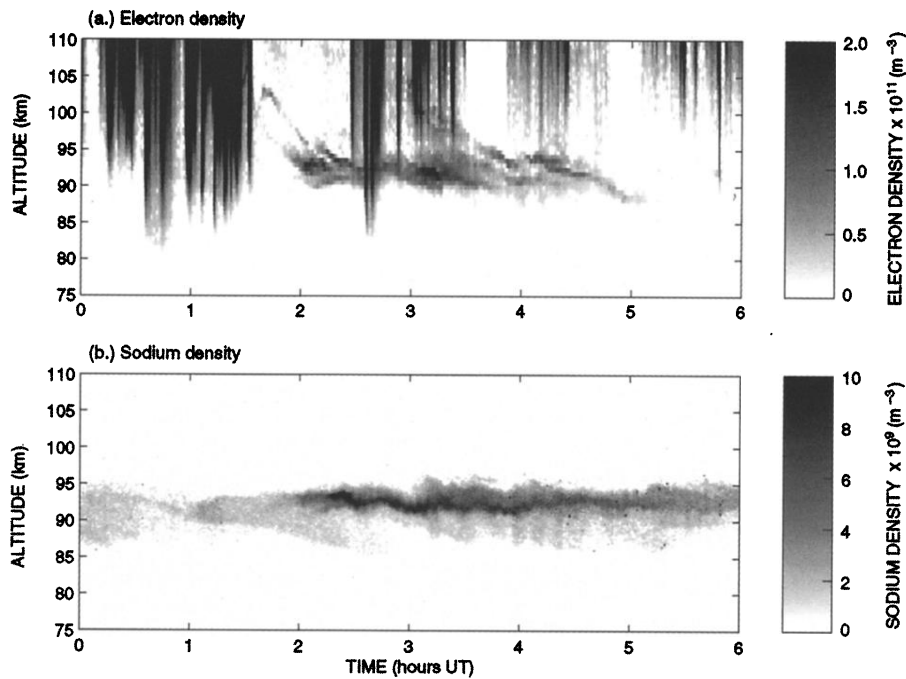


Figure 1.7 Electron and neutral sodium number densities (m^{-3}) as functions of altitude and time on 11 December 1997 (*Heinselman et al.*, 1998).

temperature increase due to tide and/or gravity wave may produce a sodium enhancement. *Gardner et al.* (1993) reported that there was a temperature enhancement over 40 K inside an SSL. Based on 43 SSL events obtained during the Airborne Lidar and Observations of Hawaiian Airglow/Airborne Noctilucent Cloud (ALOHA/ANLC-93) campaigns, *Qian et al.* (1998) reported that the majority of the SSLs had considerably larger temperatures than the mean; the average temperature enhancement was about 13 K. Therefore, the importance and role of the temperature in generating SSLs are controversial (cf. *Delgado et al.*, 2012). It should be pointed out that due to quick temporal and large altitudinal variations of the sodium density inside an SSL (cf. *Liu and Fan*, 2009), the derivation of the temperature requires a high performance of a LIDAR system.

At high latitudes, sodium atoms can be spattered by energetic auroral particles from dust particles (*von Zahn and Hansen*, 1988). Though *Hansen and von Zahn* (1990) dismissed this idea because of the poor correlation between sodium densities and cosmic noise absorption measured by riometer, *Gu et al.* (1995) proposed that the aurora was the cause of the SSL formation because an SSL and an aurora seemed to be co-located in space. On the other hand, *Tsuda et al.* (2013) clearly showed anti-correlation of sodium number densities and auroral particle precipitation based

on simultaneous observations of the sodium LIDAR and European Incoherent Scatter (EISCAT) VHF radar at Ramfjordmoen, Tromsø. Therefore, the role of auroral particle precipitation in generating an SSL is controversial.

The redistribution of sodium atoms in altitude has been proposed as one of the major generation mechanisms of SSLs (Clemesha, 1995). Kirkwood and Collis (1989) proposed that a gravity wave associated with aurora activity redistributed a normal sodium layer. Kirkwood and von Zahn (1991) proposed a generation mechanism whereby concentration of metallic ions transported downward by strong electric fields originating in the magnetosphere can generate an SSL at high latitudes.

A sporadic *E* layer (*Es* layer) is an appearance of an unusual plasma layer in the MLT region (Whitehead, 1989; Mathews, 1991). Since *Es* layers consist of metal ions (Fe^+ , Mg^+ , Na^+ etc.), it has been thought that *Es* layers would play an important role in generating SSLs. High correlations between occurrence of SSLs and *Es* layers have been reported (cf. von Zhan *et al.*, 1987; von Zhan and Hansen, 1988; Nagasawa and Abo, 1995). A deficiency of this idea is low abundance (about 10% or less) of sodium ions in *Es* layers (cf. Clemesha *et al.*, 1999). Heinselmann (2000) reported, however, that an SSL could form via the chemical reactions proposed by Cox and Plane (1998) and that an *Es* layer could supply enough sodium atoms to generate the SSL as shown in Figure 1.7. *Es* layers have been recently considered as the most likely candidate for the generation mechanisms of an SSL (cf. Clemesha *et al.*, 1999). However, SSLs were rarely observed at mid latitudes where the occurrence of *Es* layers is greater than those at low and high latitudes (cf. Arras *et al.*, 2009; Wu *et al.*, 2005). This implies that SSLs cannot be generated by *Es* layers alone. Matuura *et al.* (2013) proposed the horizontal redistribution of ions as a new mechanism capable of providing a sufficient reservoir necessary for the formation of *Es* layers and subsequent metallic atom layers.

Existing observations suggest that different processes may be involved depending on the latitude and altitude of the event (Qian *et al.*, 1998). Contrary to studies of SSLs observed at low latitudes, not much work has been conducted using an Incoherent Scatter (IS) radar and a sodium temperature LIDAR to investigate generation mechanisms of SSLs at high latitudes.

1.4 Purpose of This Thesis

GWs release their momentum flux in the MLT region, which accelerates or decelerates the zonal mean wind. Auroral precipitation and the electric field from the magneto-

sphere inject electromagnetic energy into the polar MLT region. The electromagnetic energy is converted into the thermal energy and kinetic energy in the polar MLT region. For example, an auroral precipitation causes frictional heating and the electric field causes an acceleration of charged particles. Therefore, the polar MLT region is an important region by which to understand the vertical coupling process of earth's atmosphere.

As shown in the previous sections, GWs release their momentum flux through wave dissipation. Although numerous studies for wave dissipation of GWs have been carried out, there are not many studies published that deal with dissipation of GWs of longer periods ($\geq \sim 4$ h) based on observational data of temperature and wind in the MLT region. On the other hand, SSLs may be generated by an electric field applied from the magnetosphere. However, the generation mechanism of an SSL is still an open question. Thus, we evaluate the cause of GW dissipation and generation mechanisms of an SSL.

In this thesis, we analyze two events observed under different geomagnetical conditions at Ramfjordmoen to distinguish the origins of the energy. First, we investigate a GW dissipation event observed on 29 October when auroral effects were negligible. Second, we evaluate generation mechanisms of the SSL observed on 22 January 2012 during a night of high auroral activity.

In Chapter 2, we describe the instruments such as the sodium LIDAR, the EISCAT UHF radar, the meteor radar, and the photometer operated at Ramfjordmoen utilizing this thesis.

In Chapter 3, observational results from the event on 29 October 2010 are shown, and mechanisms for GW dissipation are evaluated and discussed. Furthermore, the difference in the background atmosphere between two intervals (16:30-21:00 and 21:00-24:30 UT) is investigated. This section ends with a summary of the investigation of the upward-propagating GW.

In Chapter 4, observational results from the event on 22 January 2012 are shown and generation mechanisms are evaluated and then major mechanisms are proposed. This section ends with a summary of the investigation of generation mechanisms of the SSL.

In Chapter 5, we conclude this thesis with the results of Chapter 3 and 4.

Chapter 2

Instruments

This thesis is primarily based on observations of the sodium LIDAR at Ramfjordmoen, Tromsø, Norway (69.6°N, 19.2°E). Furthermore, the EISCAT UHF radar, the Meteor radar, the MF radar, the photometer, and the digital camera are also utilized for obtaining comprehensive datasets. These instruments have been operated at the same observational field.

2.1 Sodium LIDAR

A sodium temperature LIDAR (Light Detection And Ranging) (hereafter, sodium LIDAR) can obtain height resolved temperature and sodium density profiles between about 80 and 110 km. Neutral temperature observations by sodium LIDAR have been conducted since late 1970s (*Gibson et al.*, 1979). In this section, first, measurement principle for the sodium LIDAR will be described, and second, transmission and receiver unit of the sodium LIDAR installed at Tromsø will be presented in detail.

2.1.1 Measurement Principle

The schematic energy level of a sodium atom is shown in Figure 2.1. The D₁ and D₂ lines are transition from first excited state $3p\ ^2P_{1/2}$ to ground state and from first excited state $3p\ ^2P_{3/2}$ to ground state, respectively. Since the D₂ line is utilized by sodium LIDAR measurements, we focus on the characteristics of the D₂ line in this section. The sodium nuclear angular momentum is $I = 3/2$. Thus, the ground state splits into two hyperfine levels with total angular momentum $F = 1$ and $F = 2$ and excited state of $^2P_{3/2}$ splits into four hyperfine levels with the F value from 0 to 3. As

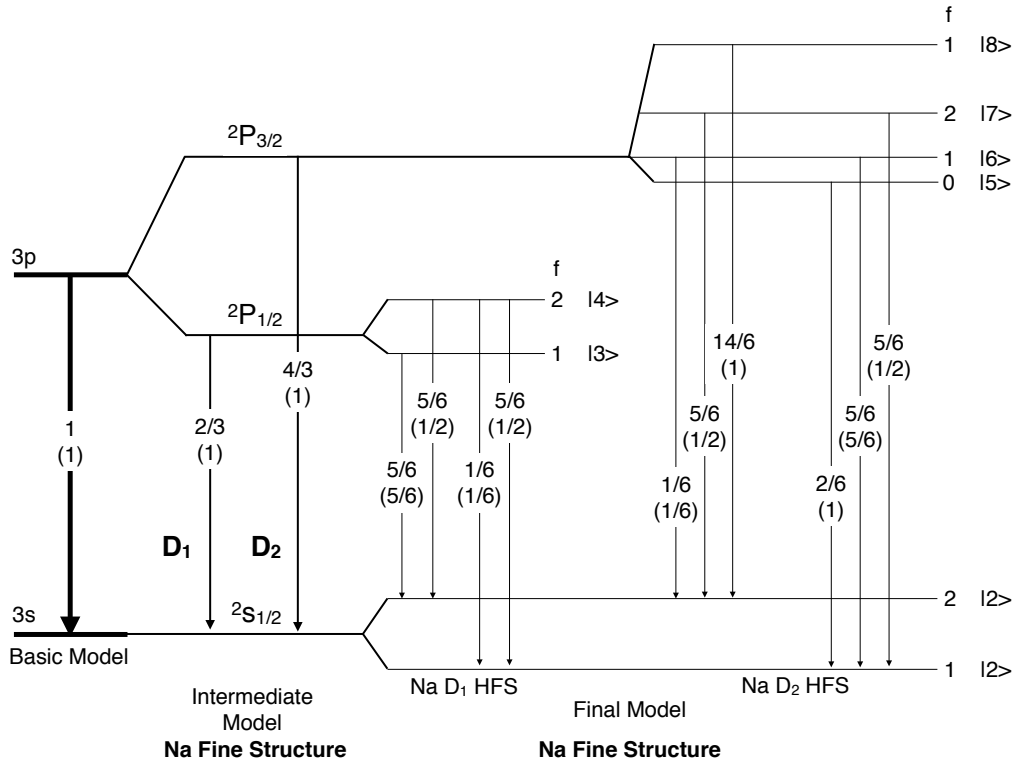


Figure 2.1 Energy level diagram of atomic Na (*She and Yu, 1995*)

a result of this separation, the D₂ line consists of two groups of lines, D_{2a} and D_{2b}. Table 2.1 shows the related numerical parameters of the D₁ and D₂ lines. For a single sodium atom, its absorption line has a Lorentzian shape with some natural line width. However, because of the Doppler effect, the absorption line will be broadened. Thus, the line shape has a Gaussian shape. The sodium D₂ line is expressed by superposition of six D₂ hyperfine transition lines (*Fujii and Fukuchi, 2005*).

$$\sigma_{eff}(\nu) = \frac{1}{\sqrt{2\pi}\sigma_e} \frac{e^2 f}{4\epsilon_0 m_e c} \sum_{n=1}^6 A_n \exp\left(-\frac{[\nu_n - \nu(1 - \frac{\nu_R}{c})]^2}{2\sigma_e^2}\right) \quad (2.1)$$

where ν_n and A_n are the center frequency and the line strength, e is the electric charge, m_e is the mass of electron, c is the speed of light, ν_R is the radial velocity of the sodium atom, and σ_e is the rms width of the Doppler-broadened line σ_D and the laser line shape σ_L and expressed as

$$\sigma_D = \sqrt{\frac{k_B T}{M \lambda_0^2}} \quad (2.2)$$

$$\sigma_e = \sqrt{\sigma_D^2 + \sigma_L^2} \quad (2.3)$$

where the k_B is the Boltzmann constant, M is the mass of sodium atom, λ_0 is the mean sodium D₂ transition wavelength of 589.15826 nm, and T is the temperature. Figure 2.2 shows the sodium absorption cross section for three temperatures at $\nu_R = 0$. The shape of the Doppler broadened linewidth is sensitive to the temperature as shown in Figure 2.2. If we measure this Doppler broadened linewidth, we can derive the temperature.

2.1.2 Temperature and Density Derivation Method

Although the high temporal resolution reduces uncertainties of the measurement, the scanning of a large range frequency is needed to obtain the line shape of the sodium D₂ line. The signal at f_a , which is the frequency at the D_{2a} peak is particularly sensitive to temperature. On the other hand, the temperature sensitivity of the signal at f_c , which is shifted several hundred MHz from f_a is weaker than the sensitivity of signal at f_a . Therefore, the ratio of the signal at f_a to the signal at f_c is a sensitive function

Table 2.1 Parameter of the Na D₁ and D₂ transition lines from *Fujii and Fukuchi (2005)*.

Transition Line	Central Wavelength (nm)	Transition Probability (10 ⁸ s ⁻¹)	Radiative Lifetime (nsec)	Oscillator Strength f_{ik}
D ₁ (² P _{1/2} → ² S _{1/2})	589.7558	0.614	16.29	0.320
D ₂ (² P _{3/2} → ² S _{1/2})	589.1583	0.616	16.23	0.641
Group	² S _{1/2}	² P _{3/2}	Offset (GHz)	Radiative Line Strength
D _{2b}	$F = 1$	$F = 2$	1.0911	5/32
		$F = 1$	1.0566	5/32
		$F = 0$	1.0408	2/32
D _{2a}	$F = 2$	$F = 3$	-0.6216	14/32
		$F = 2$	-0.6806	5/32
		$F = 1$	-0.7150	1/32
Doppler-Free Saturation-Absorption Features of the Na D ₂ Line				
f_a (MHz)	f_c (MHz)	f_b (MHz)	f_+ (MHz)	f_- (MHz)
651.4	187.8	1067.8	-21.4	-1281.4

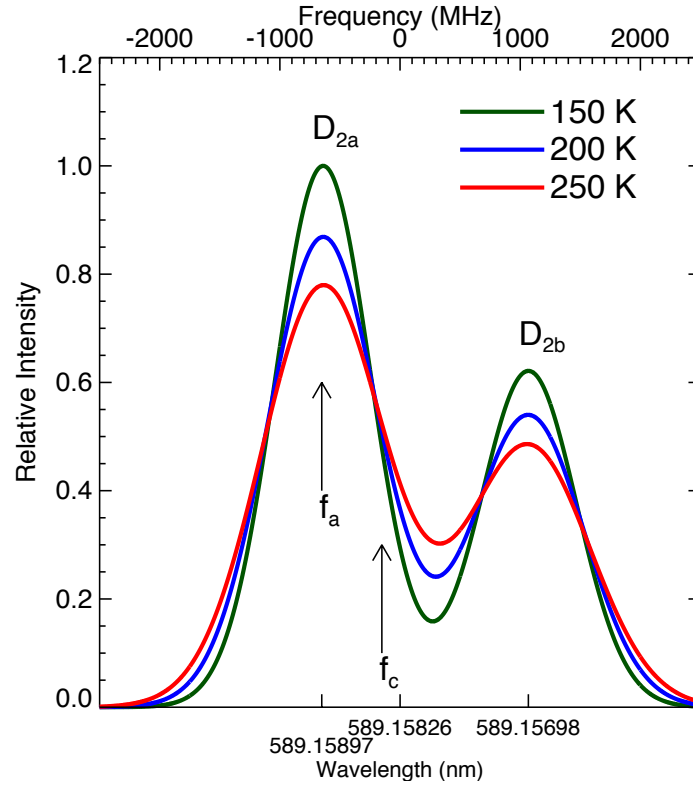


Figure 2.2 Absorption cross section of sodium atom for three temperatures in background $\nu_R = 0$. f_a is frequency at D_{2a} peak. f_c is shifted several hundred MHz from the f_a .

of temperature. The temperature derivation method calculated from the ratio is called two-frequency method (*She et al.*, 1990). For an observation, the ratio is calculated by photon counts of each frequency from a scattering region. Thus, we need solve the LIDAR equation, which is a basic equation in the field of laser remote sensing and describe the relationship between a transmitted photon and a received photon. The general LIDAR equation can be written as

$$N_S(\lambda, z) = \left(\frac{P_L(\lambda) \Delta t}{hc/\lambda} \right) (\sigma_{eff}(\lambda) n_{Na}(z) \Delta z) \left(\frac{A}{4\pi z^2} \right) \times (\eta(\lambda) T_a^2(\lambda) E^2(\lambda, z) G(z)) + N_B \Delta t \quad (2.4)$$

where

- $N_S(\lambda, z)$ = expected photon counts detected at wavelength λ
in the range interval $(z - \Delta z/2, z + \Delta z/2)$;
- λ = detected photon wavelength (m);

$P_L(\lambda)$ = laser output power at laser wavelength λ (m);

Δt = integration time (s);

h = Plank's constant (6.626×10^{-34} J/s);

c = speed of light (2.99792458×10^8 m/s);

Δz = thickness of the range bin or interval (m), which is related to the sampling time τ by $\Delta z = c\tau/2$;

$n_{Na}(z)$ = number sodium density of the resonance constituent;

A = receiving telescope aperture area (m²);

z = range from the scatter to the LIDAR receiver;

$T_a(\lambda, z)$ = one-way transmittance of the lower atmosphere for wavelength λ ;

$\eta(\lambda)$ = lidar optical efficiency for transmitted wavelength at λ ;

$G(z)$ = geometric probability of radiation at range z reaching the detector based on the geometrical considerations; and

N_B = expected photon counts per range bin per unit time due to background noise.

The LIDAR equation includes uncertainty in laser power, atmosphere transmission, and optical efficiency. The most common method for solving the LIDAR equation is to normalize the resonance fluorescence signal to the Rayleigh scattering signal $N_R(\lambda, z_R)$. The Rayleigh scattering lidar equation is expressed as below

$$N_R(\lambda, z_R) = \left(\frac{P_L(\lambda)\Delta t}{hc/\lambda} \right) (\sigma_R(\lambda)n_{Na}(z_R)\Delta z) \left(\frac{A}{z_R^2} \right) \times (\eta(\lambda)T_a^2(\lambda, z_R)G(z_R)) + N_B\Delta t \quad (2.5)$$

where σ_R is Rayleigh backscatter cross section obtained from *Bates* (1984). In this study, $N_R(\lambda, z_R)$ is the photon count at a 30 km altitude obtained from the function, which is calculated by least square of the photon counts from 25 to 35 km to avoid fluctuation of photon counts by atmospheric waves. The N_B is an average value of photon counts from 115.06 to 130.13 km. The extinction between z_R and z is negligible and the receiving telescope can see the full laser beam at both of altitude z and altitude z_R . We can assume $T_a(\lambda, z) = T_a(\lambda, z_R)$ and $G(z) = G(z_R) = 1$. The normalized photon count is expressed as

$$N_{norm}(f, z, t) = \frac{N_{Na}(f, z, t)}{N_R(f, z_R, t)E^2(f, z)} = \frac{\sigma_{eff}n_{Na}(z)}{\sigma_R n_{Na}(z_R)} \frac{z_R^2}{4\pi z^2} \quad (2.6)$$

where $N_{Na}(f, z, t)$ and $N_R(f, z_R, t)$ are pure Na and Rayleigh photon counts, respectively and shown below:

$$N_{Na}(f, z, t) = N_S(\lambda, z) - N_B \Delta t \quad (2.7)$$

$$N_R(f, z_R, t) = N_R(\lambda, z_R) - N_B \Delta t \quad (2.8)$$

The ratio of the normalized photon count at f_a to at f_c is defined as

$$R_T(z) = \frac{N_{norm}(f_c, z, t_1)}{N_{norm}(f_a, z, t_2)} = \frac{\sigma_{eff}(f_c, z) n_{Na}(z, t_1)}{\sigma_{eff}(f_a, z) n_{Na}(z, t_2)} \approx \frac{\sigma_{eff}(f_c, z)}{\sigma_{eff}(f_a, z)} \quad (2.9)$$

In this equation, we assume that the sodium density is constant at time t_1 and t_2 . Figure 2.3 shows the R_T variation with temperature. Therefore, R_T can be utilized to accurately derive the temperature. The sodium density is also derived by following equation.

$$n_{Na}(z) = n_R(z_R) 4\pi \frac{\sigma_{eff}}{\sigma_R} \frac{N_{Na}(f, z, t)}{N_R(f, z_R, t) E^2} \frac{z^2}{z_R^2} \quad (2.10)$$

To derive the neutral temperature, a sodium LIDAR needs to switch two frequencies and the calculation requires the assumption of the sodium density constant. On the other hand, the sodium density derivation requires the photon counts from z_R and z at one frequency.

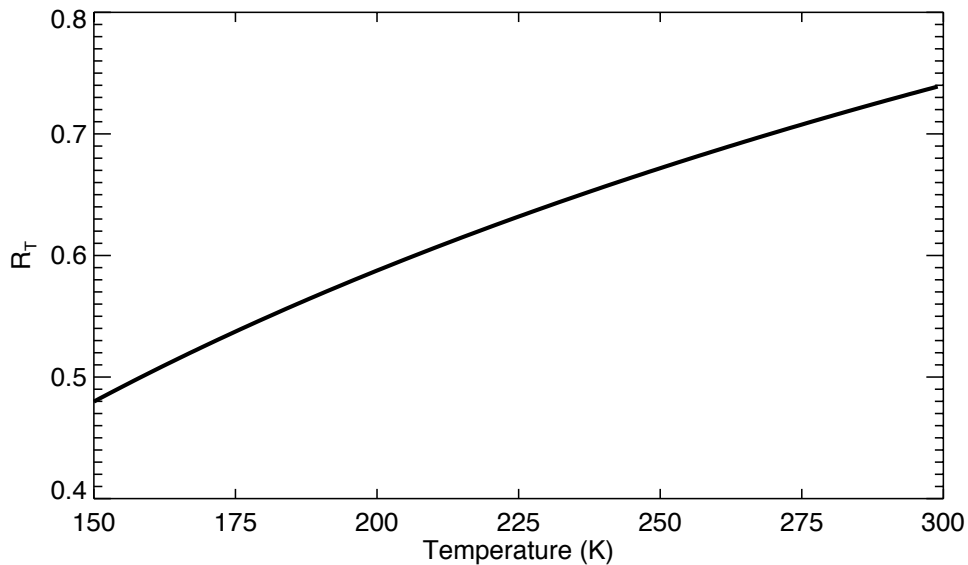


Figure 2.3 Ratio R_T versus the temperature T from 150 to 300 K in background wind $v_R = 0$.

2.1.3 Error Calculation

The random uncertainty associated with laser jitter, random Na density fluctuations, and the shot noise cause the temperature and the sodium density derivation error. The laser jitter is usually quite small (*Fujii and Fukuchi, 2005*). The random Na density fluctuation can be minimized and eliminated by quickly frequency switching.

Since the photon count statistically depends on Poisson distribution, the shot noise limits the measurement precision. According to *Fujii and Fukuchi (2005)*, for the two-frequency ratio technique, the relative error of ratio R_T is given by

$$\frac{\Delta R_T}{R_T} = \frac{\left(1 + \frac{1}{R_T}\right)^{1/2}}{N_{fa}^{1/2}} \left\{ 1 + \frac{B}{N_{fa}} \frac{\left(1 + \frac{1}{R_T^2}\right)}{\left(1 + \frac{1}{R_T}\right)} \right\}^{1/2} \quad (2.11)$$

where

$$N_{fa} = N_{Na}(f_a, z, t) \quad (2.12)$$

$$B = N_B \Delta t \quad (2.13)$$

As shown in equation (2.11), the relative error of ratio strongly depends on the photon count at f_a . The temperature error is given by

$$\Delta T = \frac{\partial T}{\partial R_T} \Delta R_T = \frac{\Delta R_T}{R_T} \left(\frac{\partial \sigma_{eff}(f_c)/\partial T}{\sigma_{eff}(f_c)} - \frac{\partial \sigma_{eff}(f_a)/\partial T}{\sigma_{eff}(f_a)} \right)^{-1} \quad (2.14)$$

The error calculation of sodium density is more simply. By calculation of the propagation of errors for the equation (2.10), the sodium density error is given by

$$\Delta n_{Na} = \frac{\sqrt{N_{fa} + 2B}}{N_{fa}} n_{Na} \quad (2.15)$$

According to this calculation, the Tromsø sodium LIDAR can derive the temperature and the sodium density with error values less than 1 K and 10^8 m^{-3} (correspond to 0.2% of the sodium density), respectively from 80 to 100 km at nighttime.

2.1.4 Transmission and Receiving Units

Figure 2.4 shows layout of transmission unit of the Tromsø sodium LIDAR. The LIDAR transmission unit consists of an all solid state Q-switched single-frequency

source tuned to the sodium LIDAR at 589.1583 nm. This unit was manufactured by MegaOpt Co., Ltd.. The source is based on sum-frequency mixing of two injection-locked neodymium-doped yttrium/aluminum/garnet (Nd:YAG) lasers in LiB_3O_5 , which were used under 90 degree phase-matching condition at a temperature 39.5 degree. We observed an average output power of ~ 2.2 W on 22 January 2012 at a repetition rate of 1 kHz which corresponds to an energy conversion efficiency of approximately 45%. Due to loss in optical devices (i.e., lens, mirror, and telescope), we transmitted with a power of ~ 1.8 W in the beginning of the season. During the first seasonal observations, the power was from 1.4 W to 1.8 W. During the second seasonal observations, the laser power was from 2.2 W to 2.5 W.

We changed the wavelength every 2 or 1 min for the two-frequency method by Acoust-Optics.

The telescope is the Celestron's Schmidt-Cassegrain Optical Tube with a diameter of 355 mm, the Photomultiplier Tube is H7421-40 produced by Hamamatsu photonics K.K., and the multichannel scaler is AMCS-USB+ by Sigma Space Corporation. The range resolution is 96 m. When we monitor the field-of-view of the telescope to capture laser backscatter echo correctly from the sodium layer, a CCD camera (ST-9XEi) is used to observe the field-of-view by changing the raypath by a mirror (motor controlled).

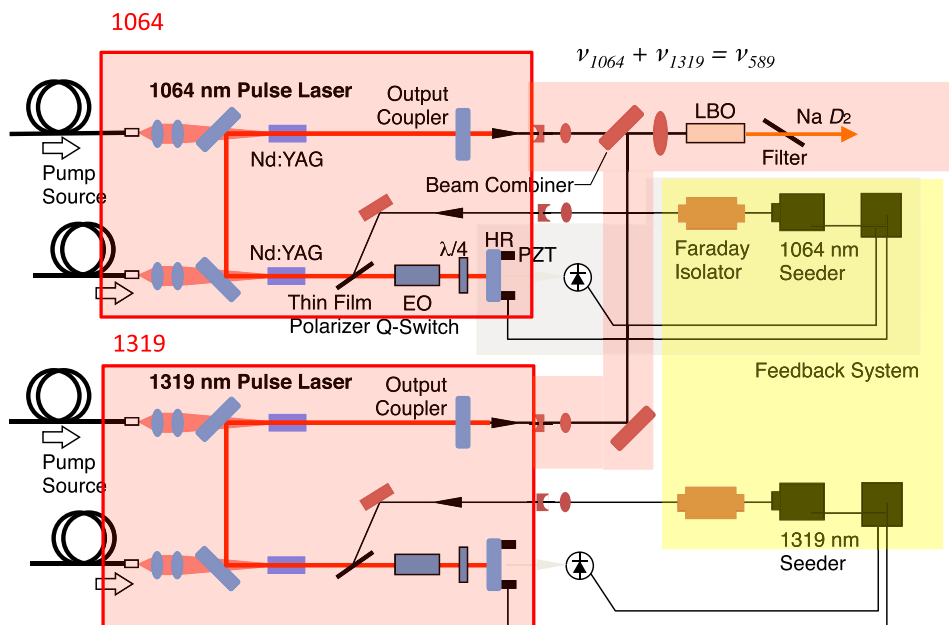


Figure 2.4 Layout of sodium D_2 resonance light source for the sodium LIDAR at Tromø (Nozawa *et al.*, 2014).

2.2 EISCAT UHF Radar

The European Incoherent Scatter (EISCAT) UHF radar at Ramfjordmoen has a 32 m antenna that is fully steerable both in azimuth and elevation and has been operated since 1981. The EISCAT UHF radar transmits a radio wave at 931 MHz to electrons and received the reflection from the Thomson backscatter of the electrons. Since the Debye length of plasma in the ionosphere (about 6.87×10^{-3} m) is much less than the wavelength of transmit wave (about 0.32 m), the EISCAT UHF radar observes ion acoustic and Langmuir wave. Figure 2.5 shows the scattered spectrum of the EISCAT UHF radar that consists of ion line and plasma line. This spectrum provides the electron density, electron temperature, ion velocity, and ion temperature.

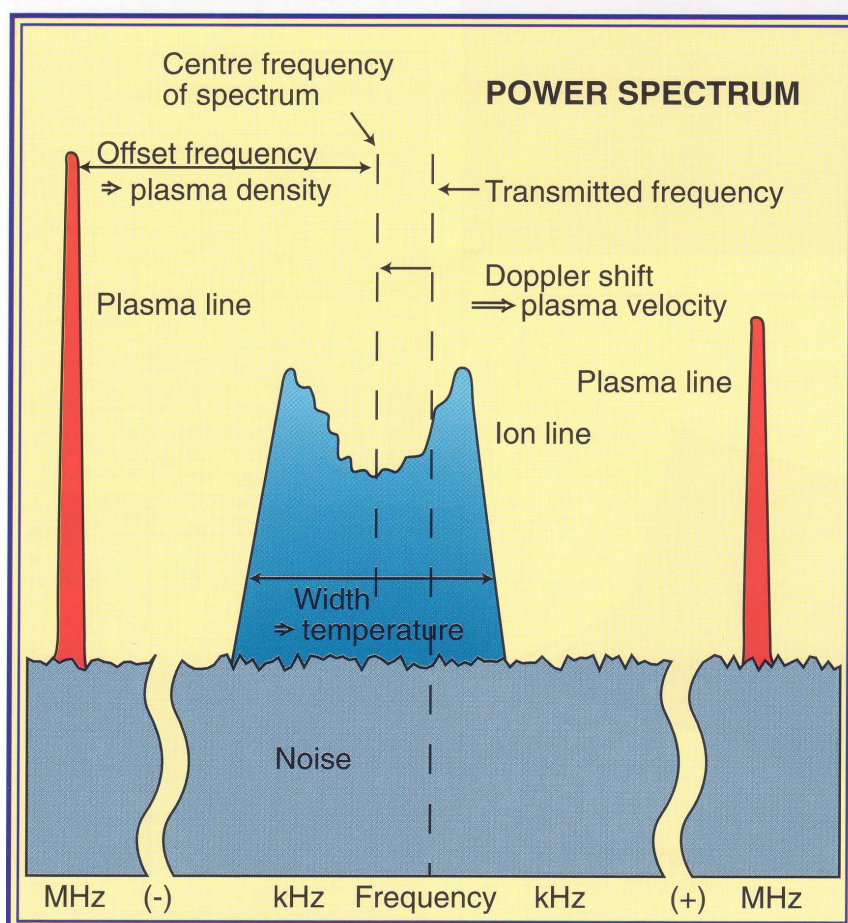


Figure 2.5 Power spectrum of incoherent scatter radar. (from the pamphlet of the EISCAT Scientific Association)

2.3 Meteor Radar and MF Radar

The Meteor radar (MR) installed in Ramfjordmoen can continually provide neutral wind velocity data with 2 km altitude and 1 h time resolution from approximately 80 to 100 km (*Hall et al.*, 2005). This radar system operates at 30.25 MHz. The field of view of this radar is about 140 degree, i.e. a spatial averaging over perhaps 200 km at the peak echo occurrence height. Descriptions of the determination of wind velocity may be found, for example, in *Aso et al.* (1979) and *Tsutsumi et al.* (1999).

The Tromsø MF radar has been in operation for more than 20 years in a spaced-antenna (wind measuring) mode (see, e.g., *Meek*, 1980; *Reid*, 1996). A recent specification of this radar can be found in *Hall* (2001). The Tromsø MF radar operating at 2.78 MHz has continually provided wind data together with echo power in the height region of ~ 70 to ~ 100 km in so-called “virtual” height. As a result of group retardation, the true heights of the reflections are somewhat lower, particularly for heights above 90 km (*Hall*, 2001). The time resolution is usually 5 min.

2.4 Photometer

The photometer was pointed towards along local geomagnetic field line (Azimuth= 182.6° , Elevation= 77.5°) with a field of view of 1.2 degrees. It has equipped with three optical

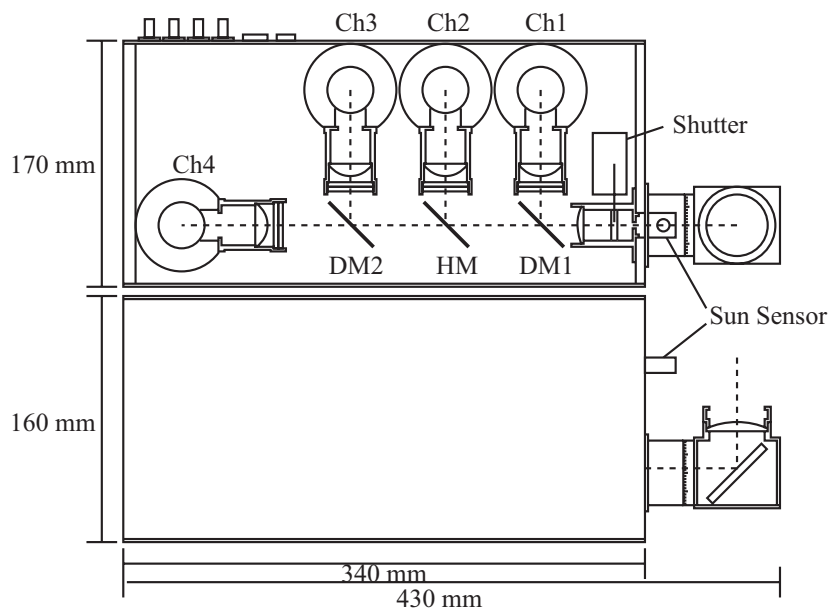


Figure 2.6 Layout of the photometer. HF and DM are half mirror and dichroic mirror.

filters tuned for wavelengths of 427.8nm, 557.7 nm, 630.0 nm. Their FWHMs are 2nm, 3nm and 2nm, respectively. Figure 2.6 shows layout of the photometer. The photometer can receiver photons through the three filters simultaneously with a sampling rate of 20 Hz.

2.5 Digital Camera

The all-sky digital camera has been installed at Ramfjordmoen to verify the local weather, aurora, and cloud conditions. To obtain all-sky images we use a D5000 NIKON digital camera fitted with a fisheye lens, which is 4.5mm F2.8 EX DC CIRCULAR FISHEYE HSM by SIGMA Corporation. Figure 2.7 shows several examples of all-sky images under several conditions: geomagnetic quiet time, high auroral activity, and overcast. The sampling rate and exposure time are 1min and 30 sec, respectively.

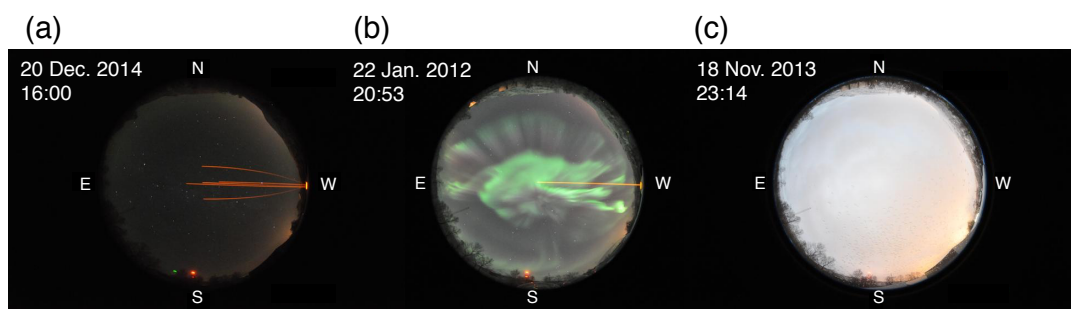


Figure 2.7 Images under conditions of (a) geomagnetic quiet condition, (b) high auroral activity, and (c) overcast.

Chapter 3

Gravity Wave Dissipation in the Polar MLT Region

In this Section, we have investigated the dissipation process of a GW in the polar MLT region based on temperature, wind, and echo power data obtained with the sodium LIDAR, meteor radar, and MF radar, respectively, operated at the same observational field: Ramfjordmoen, Tromsø, Norway (69.6°N, 19.2°E). The 3-hour Kp index was 1, 0, 0, and 0 between 15:00 UT on 29 October and 03:00 UT on 30 October 2010, indicating that auroral effects are negligible. The result of this Chapter have been reported by *Takahashi et al.* (2014).

3.1 Observational Results

Figure 3.1a shows temporal and altitudinal variations of the neutral temperature observed with the sodium LIDAR from 16:30 UT on 29 October 2010 to 00:30 UT on 30 October 2010. To increase the signal-to-noise ratio, we have applied time integration of 10 min and smoothing to the height with a von Hann (Hanning) window of 1.2 km resolution. Corresponding error values are shown in Figure 3.1b. The error values are less than 2 K for most instances below ~ 101 km, while the error values reached about 10-20 K at 105 km. From Figure 3.1a, we can identify that a higher temperature region lowered with time during the observational interval between 80 and 95 km. For example, the higher-temperature (about 230 K) region was seen at about 92 km at 20:00 UT and moved down to about 82 km at 23:00 UT. These temporal and altitude variations of the temperature suggest the signature of a monochromatic gravity wave (GW) propagating upward. On the other hand, no periodical temperature

variation can be seen above 95 km between 16:30 and 21:00 UT, while a similar (but weaker) temperature variation can be found above 95 km from 21:00 to 24:30 UT. This difference suggests that conditions of the background atmosphere changed and affected the propagation of the GW.

Figure 3.2a shows contours of spectra of the neutral temperature from 80 to 100 km for the same time interval as Figure 3.1. The Lomb-Scargle periodogram method (cf. *Press and Rybicki, 1989; Hocke, 1998*) using an oversampling factor of 4 was applied. From Figure 3.2a, a component with a period of about 4 h is found to be dominant below 90 km, while at 100 km a component of about 8 h is significant. The amplitude of the 4 h component reached a maximum at 86 km with a value of ~ 15 K. It should be pointed out that the 8 h temporal variation found at 100 km is probably not a real periodic component because no clear temporal variation of the temperature between 16:30 and 21:00 UT above 95 km is seen in Figure 3.1a. As shown in Figures 3.2b and 3.2c when we analyzed temperature data for two time intervals separately between 16:30 and 20:30 UT and between 20:30 and 24:30 UT, no salient periodic variation of the temperature was found for the earlier interval above 95 km, while a 4 h variation component was found for the latter interval.

Figure 3.3 shows nighttime temporal variations of eastward (a) and northward (b) wind velocities observed with the MR from 16:30 to 24:30 UT. MR wind measurement above 100 km is rather difficult, and therefore we present only the wind velocity from 80 to 100 km. The zonal wind blew eastward above 92 km over the interval with a maximum velocity of about 60 m s^{-1} . The eastward wind, however, did not show dramatic changes before and after 21:00UT. On the other hand, the meridional wind velocity varied from -30 m s^{-1} (southward) to 40 m s^{-1} (northward). The northward wind speed became lower after 21:00UT above 90 km, and the wind direction changed from north to south around 21:30 UT below ~ 90 km.

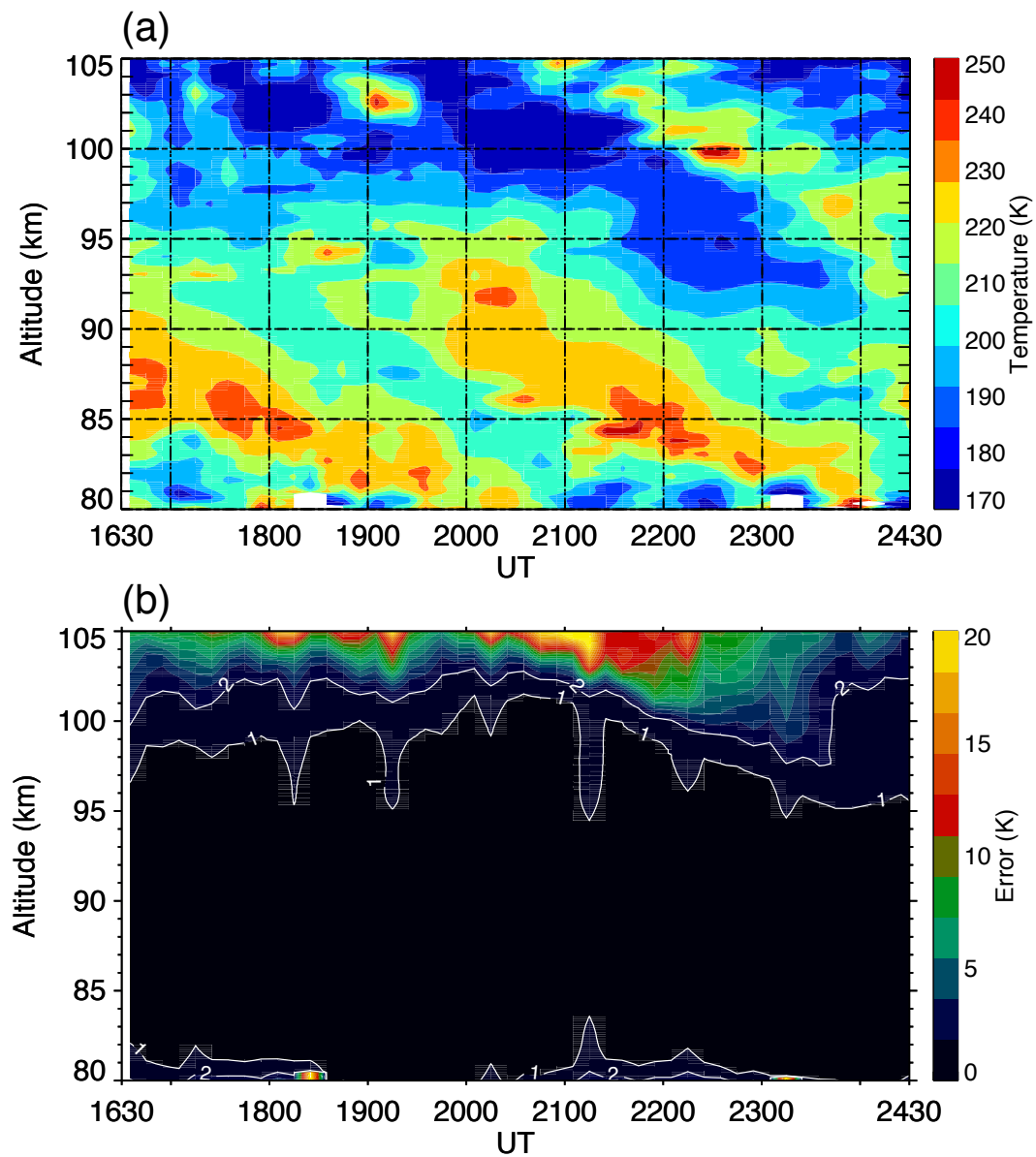


Figure 3.1 (a) The neutral temperature variation from 16:30 UT 29 October to 00:30 UT on 30 October 2010. The warmer color indicates higher temperature and colder color indicates lower temperature. The original temporal and altitude resolution is 10 min and 1.2 km, respectively, and a 30 min running average is applied. (b) The corresponding error values of the temperature.

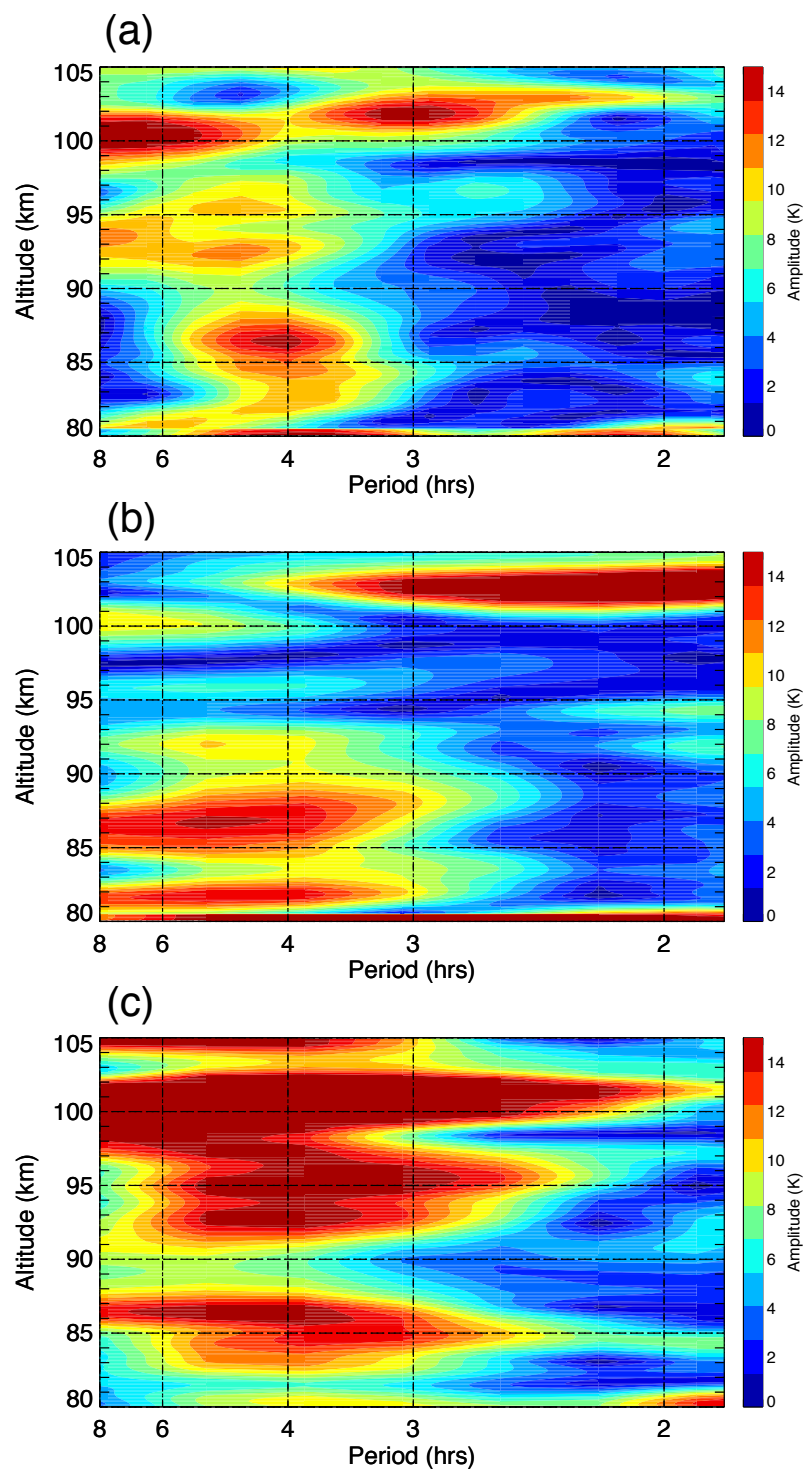


Figure 3.2 Periodograms as a function of altitude for the neutral temperature variation (a) between 16:30 to 24:30 UT, (b) between 16:30 and 20:30 UT, and (c) between 20:30 and 24:30 UT derived by the Lomb-Scargle method with an oversampling factor of 4.

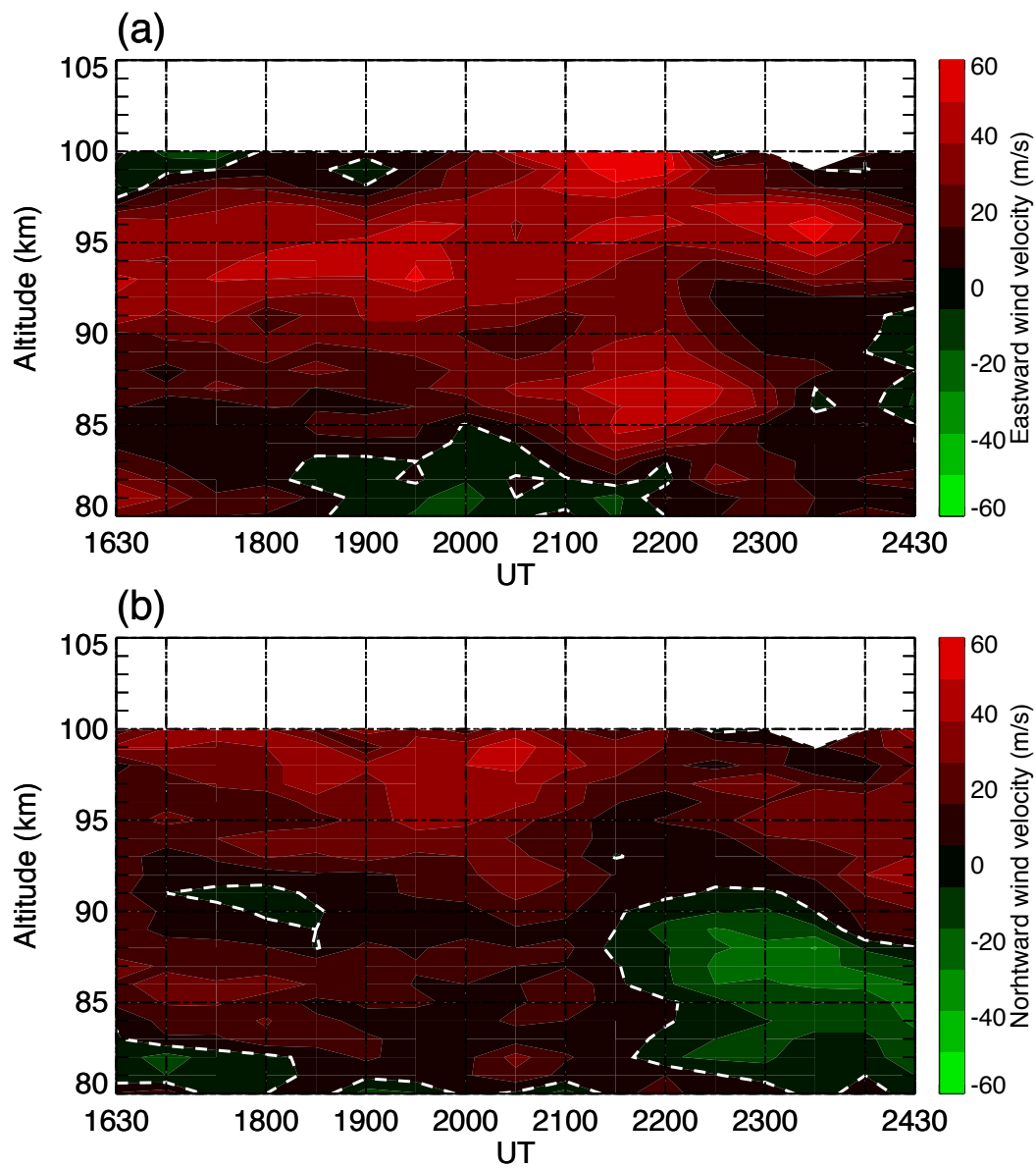


Figure 3.3 The eastward (a) and northward (b) wind velocity obtained by meteor radar from 80 to 100 km from 16:30 to 24:30 UT on 29 October 2010. White dashed lines indicate zero wind velocity.

3.2 Discussion

We will investigate how the GW disappeared around 95 km before 21:00UT by evaluating three mechanisms: critical-level filtering and convective and dynamic instabilities. If critical-level filtering prevents a GW from achieving upward propagation, the background wind velocity must be equal to or larger than the horizontal phase velocity of the GW. The square of the Brunt-Väisälä frequency should become negative in the height region if a GW is dissipated by convective instabilities. The square of the Brunt-Väisälä frequency, N^2 , is expressed by

$$N^2 = \frac{g}{T} \left(\frac{dT}{dz} + \Gamma_d \right) \quad (3.1)$$

where g , T , z , and Γ_d are the acceleration of gravity (9.5 m s^{-2}), neutral temperature, altitude, and adiabatic lapse rate in dry air ($9.5 \times 10^{-3} \text{ K m}^{-1}$). The (bulk) Richardson number is calculated from the following formula:

$$Ri = \frac{N^2}{\left(\frac{du}{dz}\right)^2 + \left(\frac{dv}{dz}\right)^2} \quad (3.2)$$

where du/dz and dv/dz are differential eastward and northward wind velocities, respectively. One of the dynamical instabilities in the atmosphere is the Kelvin-Helmholtz (KH) instability, which sets in when the Richardson number (Ri) of the wind profile is less than 0.25 (*Drazin*, 1958), whereas $Ri < 1$ describes conditions still favorable to the instability persisting (cf. *Szewczyk et al.*, 2013).

3.2.1 Critical-Level Filtering

We have derived horizontal phase velocity, vertical and horizontal wave numbers and propagating direction of the GW from the LIDAR temperature data as well as the MR wind data using the hodograph method (*Sawyer*, 1961). The dispersion relation of inertia gravity wave, on the assumption that the Boussinesq approximation can be applied for GWs, is shown as

$$\sigma = k(c - U) = \left(\frac{f^2 m^2 + N^2 k^2}{k^2 + m^2} \right)^{1/2} \quad (3.3)$$

where σ is intrinsic frequency, k is horizontal wave number, c is the phase velocity of the GW, U is the background wind speed along with the propagation direction of the GW, f is the inertia frequency ($f = 1.36 \times 10^4 \text{ rad s}^{-1}$ at Tromsø), and m is the vertical wave number of the GW. The altitude region where c equals U is called the critical level, and GW cannot propagate to altitudes above the critical level. This is known as critical-level filtering (cf. *Ejiri et al.*, 2009; *Suzuki et al.*, 2009; *Taylor et al.*, 1993).

The hodograph method is based on the linear theory for GWs (cf. *Placke et al.*, 2013) and has been used to determine the propagation direction as well as phase velocity of GWs (e.g., *Yamamoto et al.*, 1987; *Namboothiri et al.*, 1996). For a monochromatic wave, an ellipse can be drawn. The major axis of the ellipse indicates the propagation direction, and the direction of rotation as a function of height (from lower height to upper height) indicates the direction of energy transport. The upward propagation of GWs observed in the Northern Hemisphere is subject to a clockwise rotation. Intrinsic frequency of a GW can be obtained from the polarization relation

$$\sigma = \frac{\tilde{u}}{\tilde{v}} f \quad (3.4)$$

where \tilde{u} and \tilde{v} are lengths of the major and minor axes, respectively. The dispersion relation can be obtained from equation (3.3) when solved for horizontal wave number (k):

$$k^2 = \frac{f^2 - \sigma^2}{\sigma^2 - N^2} m^2 \quad (3.5)$$

The vertical wave number (m) can be derived by the hodograph method, and N^2 can be calculated from the LIDAR temperature data as a function of altitude and time using equation (3.1). Phase velocity is given as follows:

$$c = \frac{\omega}{k} \quad (3.6)$$

where ω is the apparent frequency, and $\omega = 4.36 \times 10^{-4} \text{ rads}^{-1}$ (i.e., $2\pi/4 \text{ h}$) in this event. By using the hodograph method, and equations (3.4), (3.5), and (3.6), we can derive the phase velocity along the propagation direction of the GW.

The hodograph method works properly only for a monochromatic wave event (cf. *Lue and Kuo*, 2012). It should be pointed out that for the four winter observations of the sodium LIDAR at Tromsø, from October 2010 to March 2014, the current event is one of the most prominent monochromatic wave events. In addition, geomagnetically,

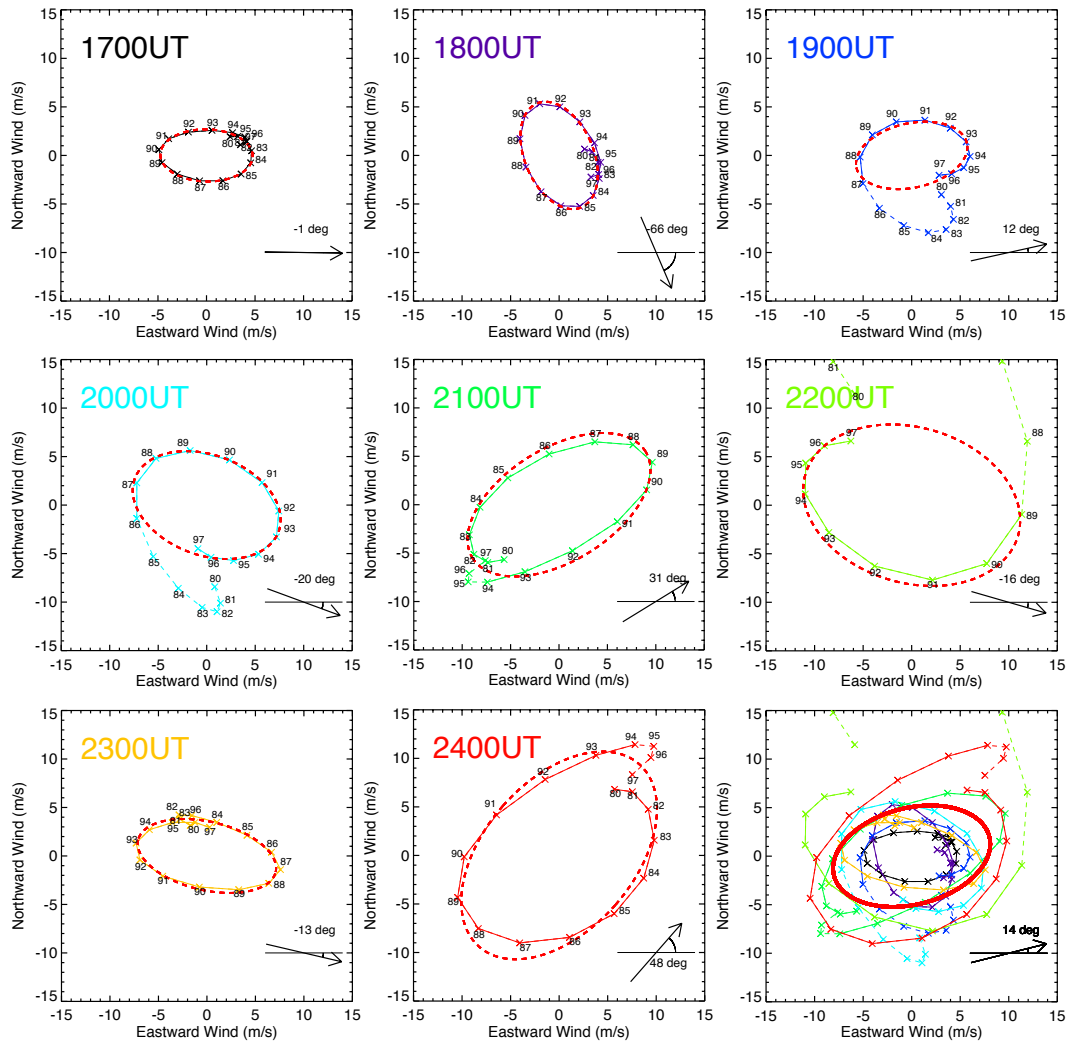


Figure 3.4 Eight hourly hodographs associated with the fitted ellipses are shown. Crosses denote data values associated with corresponding height values (in km). In the bottom right panel, superimposed hodographs with the fitted ellipse (thicker solid line) are presented. The estimated propagation direction is illustrated in each panel.

it was a very quiet interval (K_p less than 1); thus, this event is a rare case. For the hodograph analysis, we use MR wind data obtained over 48 h from 00:00 UT on 29 October to 24:00 UT on 30 October 2010. First, the mean wind over periodic components that are 48 h and longer (longer than 8 h) and which are derived by the Lomb-Scargle periodogram method using an oversampling factor of 4 is removed from the wind data. Second, using the 8 h length of wind data from 16:30 to 24:30 UT on 29 October 2010, periodic components are derived by the Lomb-Scargle periodogram

method using an oversampling factor of 4, and then shorter components (shorter than 3 h) are removed from the wind data. Third, a similar procedure is applied for the altitude domain from 80 to 97 km. Then, components utilized for the hodograph analysis that have periods of 3 to 8 h and whose vertical wavelength is longer than 7.5 km are selected from the data sets.

Figure 3.4 shows eight sets of hourly hodographs (solid lines) from 17:00 to 24:00UT. Data values (shown by crosses) together with corresponding height values are illustrated. Furthermore, ellipses (red dashed lines) derived by the least-squares fit and estimated propagation directions are presented in each panel. Some other periodic components seem to be mixed in the hodographs at 19:00, 20:00, and 22:00 UT at lower heights, and we have only used data values at and above 87, 86, and 89 km for the respective times. Given the 180 deg ambiguity, we can conclude that the GW propagated toward east-northeast/east-southeast or west-southwest/west-northwest.

In the bottom right panel, all the eight hodographs together with an ellipse (thick red solid line) are illustrated, and the ellipse is obtained by the least-squares fit of the eight hodographs using the following method. The upward GW propagation can be divided into two components east-west and north-south that are expressed by the apparent frequency (ω), the vertical wave number (m), the phase (ϕ) of the retrieved wave component, and the propagation direction angle (θ) counted clockwise from east. The following equations are utilized to derive the ellipse:

$$U_{east} = \tilde{u} \cos(\omega t - mz - \phi) \cos \theta - \tilde{v} \sin(\omega t - mz - \phi) \sin \theta \quad (3.7)$$

$$U_{north} = \tilde{u} \cos(\omega t - mz - \phi) \sin \theta - \tilde{v} \sin(\omega t - mz - \phi) \cos \theta \quad (3.8)$$

The major and minor axes of the fitted hodograph (i.e., the ellipse) are 16.5 and 9.95 m s⁻¹, respectively. The propagation direction is 14 deg north (south) from east (west), i.e., almost eastward or westward. The estimated vertical wavelength is about 11.9 km. By substituting the major and minor axes and the inertial frequency, equation (3.4) gives the intrinsic frequency of the gravity wave, σ , as 2.26×10^{-4} rad s⁻¹, which corresponds to an oscillation period of ~ 7.7 h. The square of the Brunt-Väisälä frequency, N^2 , is 4.41×10^{-4} rad² s⁻² (i.e., the Brunt-Väisälä period being about 5 min) on average (negative values were rejected) between 81 and 95 km from 16:30 to 24:30 UT. Thus, equation (3.5) gives the horizontal wave number (k), i.e., 4.56×10^{-6} rad m⁻¹, which corresponds to the horizontal wavelength of ~ 1379 km. Therefore, the horizontal phase velocity, c , is calculated to be 96 m s⁻¹ by equation (3.6).

Table 3.1 Parameters derived with the hodograph method.

Time (UT)	\bar{u} (m/s)	\bar{v} (m/s)	θ (rad)	c (m/s)	U (m/s)	$c - U$ (m/s)
1700	9.51	5.37	-0.02	88.6	38.1	50
1800	11.6	7.07	-1.17	95.2	39.2	56
1900	11.6	6.63	0.22	86.2	45.4	40
2000	15.8	10.3	-0.35	100	50.3	50
2100	21.0	11.7	0.55	83.6	51.9	32
2200	22.8	16.0	-0.28	127	47.9	79
2300	14.6	7.06	-0.23	75.9	51.0	25
2400	25.0	15.4	0.85	98.5	37.6	61
All	16.5	9.95	0.24	95.8	51.3	45

All parameters derived from the hodograph method are listed in Table 1. Since the intrinsic frequency is less than apparent frequency, the propagation direction is likely almost eastward. The maximum wind velocity along the estimated propagation direction during the 8 h is 51 m s^{-1} , which is significantly less than c (96 m s^{-1}). Furthermore, as shown in Table 1, the differences ($c - U$) for the hourly results are always positive. These results indicate that the phase velocity c was always greater than the background wind velocity U . Therefore, we conclude that critical-level filtering was not a dominant mechanism for the GW disappearing in this event. Another point to be investigated is the similarity of wave-like structures measured with the LIDAR and the MR. Since physical parameters provided with the two instruments differ, to ensure both instruments captured the same GW, we should investigate the relationship below:

$$\tilde{\theta} \left(= \frac{\theta'}{\bar{\theta}} \right) = i \frac{N^2}{g\sigma} \frac{k}{m} u' \quad (3.9)$$

where $\tilde{\theta}$ is proportion of the fluctuation of the potential temperature, $\bar{\theta}$ and i are the potential temperature and imaginary unit, and θ' and u' are perturbations of potential temperature and wind velocity along the propagation direction, respectively (cf. *Fritts and Alexander, 2003*). Here, we use the MR wind data obtained for the same interval as the LIDAR temperature data from 16:30 to 24:30 UT on 29 October 2010, and $u' = 13 \text{ m s}^{-1}$ at 87 km (from Figure 3.5c). By using the parameter values above, we obtain

$$\tilde{\theta} = 0.023 \quad (3.10)$$

This estimation suggests that perturbation of the background temperature due to the GW should be $\sim 2.3\%$. The averaged temperature over the 8 h is $\sim 216 \text{ K}$ at 87 km,

and then the temperature perturbation is calculated to be ~ 5.0 K ($= 0.023 \times 216$), which is about 40% of the amplitude observed by the LIDAR (see Figure 3.5c).

According to Equation (3.9), the phase of the GW in the temperature should precede by 90 deg that of the wind along the propagation direction (i.e., 1 h for the oscillation period of 4 h). Figure 3.5a shows height profiles of the phases of the temperature and the wind for the GW (with an apparent period of 4 h) along its propagation direction, and Figure 3.5b shows their differences. Figure 3.5c shows height profiles of the amplitudes of the temperature (blue) and the wind (red) data. Blue double circles denote the values whose normalized amplitudes are greater than the corresponding 99% significance levels, and they are located between 85 and 90 km and between 96 and 97 km. The phase difference between 85 and 90 km presented in Figure 3.5b shows that phases of the temperature preceded that of the wind by about 0-1 h. When we consider worse temporal resolution of the MR (1 h) wind measurements, these results confirm that the LIDAR and the MR have captured the same GW signature.

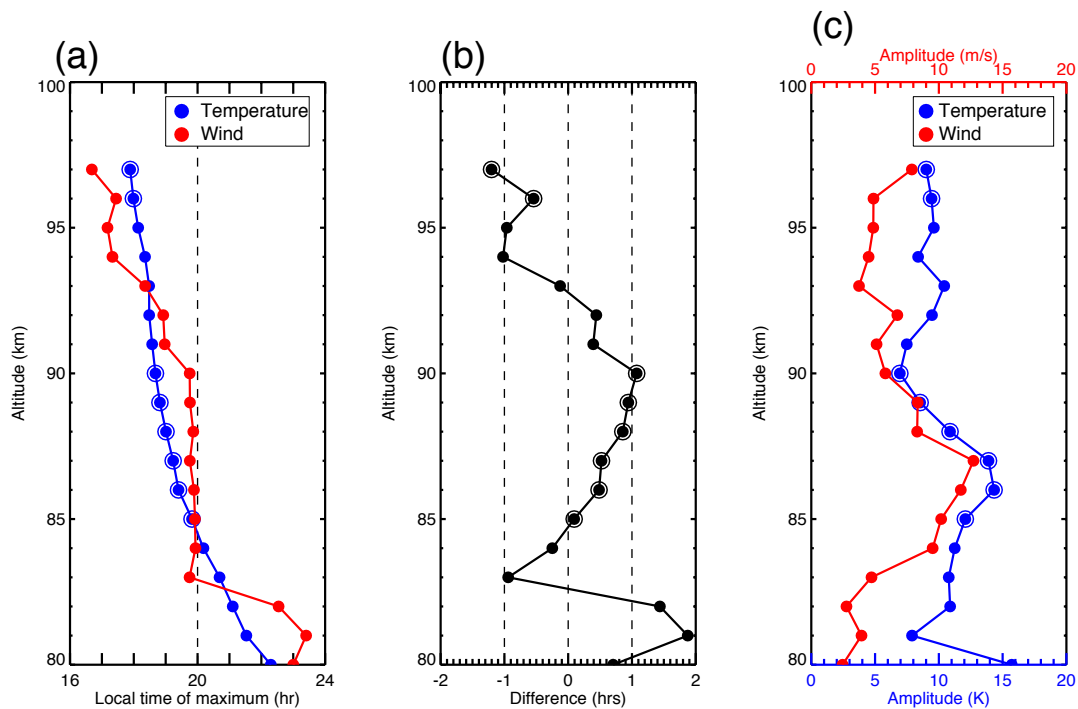


Figure 3.5 The local time maximum (a), phase difference between temperature and wind oscillation (b), and amplitude profile of the temperature and wind (c). The red and blue circles denote wind and temperature data, respectively. The period is 4 h. The double circles show values over the 99% significance level.

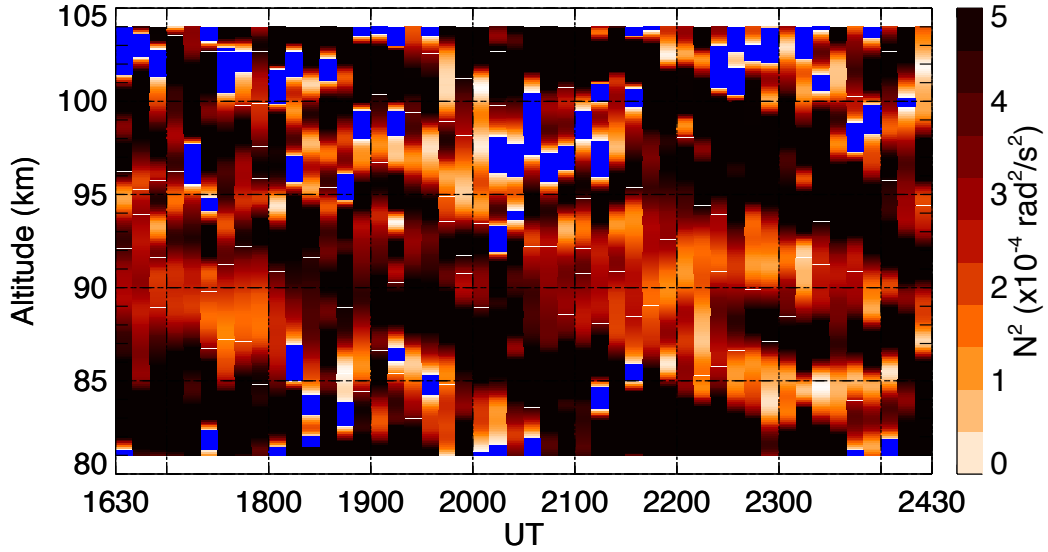


Figure 3.6 Variations of the square of Brunt-Väisälä frequencies (N^2) from 16:30 to 24:30 UT between 81 and 104 km. Negative N^2 regions are shown by blue filled squares.

3.2.2 Convective and Dynamic Instabilities

GWs dissipate their energy due to convective instabilities when the background temperature gradient is superadiabatic (*Hodges Jr., 1967*). The Brunt-Väisälä frequency can be used as an indicator of the convective instability. Figure 3.6 shows the square of Brunt-Väisälä frequencies, derived by Equation (3.1), from 16:30 to 24:30 UT between 81 and 104 km. Negative ($N^2 < 0$) regions are shown by blue filled squares. The vertical temperature gradient, dT/dz , is calculated using neighbor data within ± 1 km height. Below 87 km, there is a tendency for the number of negative regions to be larger before 21:00 UT than those after 21:00 UT, while between 87 and 94 km N^2 is almost always positive over the time interval. Between 95 and 100 km, N^2 is lower before 21:00 UT than after 21:00 UT. Furthermore, there is a tendency for the negative values to occur more frequently before 21:00 UT than after 21:00 UT between 95 and 100 km.

Figure 3.7a shows variations of the Richardson number from equation (3.2), and Figure 3.7b shows their error values. More precisely, this Ri should be called the bulk Richardson number, but, as in many other studies, we call it the Richardson number in this paper. The error values are calculated based on the propagation of uncertainties,

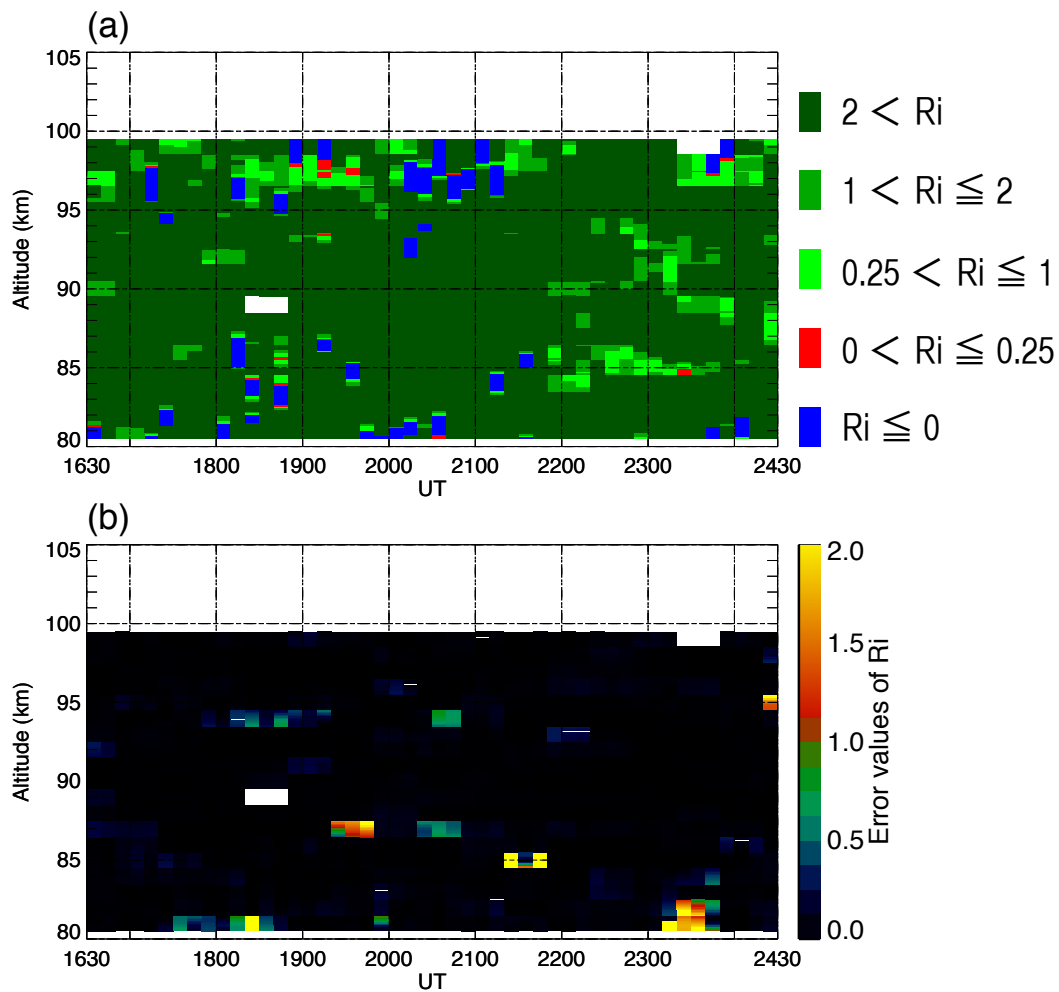


Figure 3.7 (a) Variations of the Richardson number from 81 to 99 km between 16:30 and 24:30 UT on 29 October 2010. Negative values are shown by blue filled squares. (b) Error values of the Richardson number.

and they are less than 0.5 for almost the whole time interval. Between 16:30 and 21:30 UT, there is an almost continual layer (about a few km thick) where the Richardson number is less than 2 (including negative values) between 95 and 99 km. The value of $0 < Ri < 0.25$ occurred rarely, but it occurred between 18:50 and 19:40 UT around 97-98 km. Since the almost all-sky horizontal view (~ 140 degree) as well as poor height (2 km) and temporal (1 h) resolution of the MR induces overestimation of Ri , we are able to say that the shear instability occurred more frequently than the current occurrence of $0 < Ri < 0.25$.

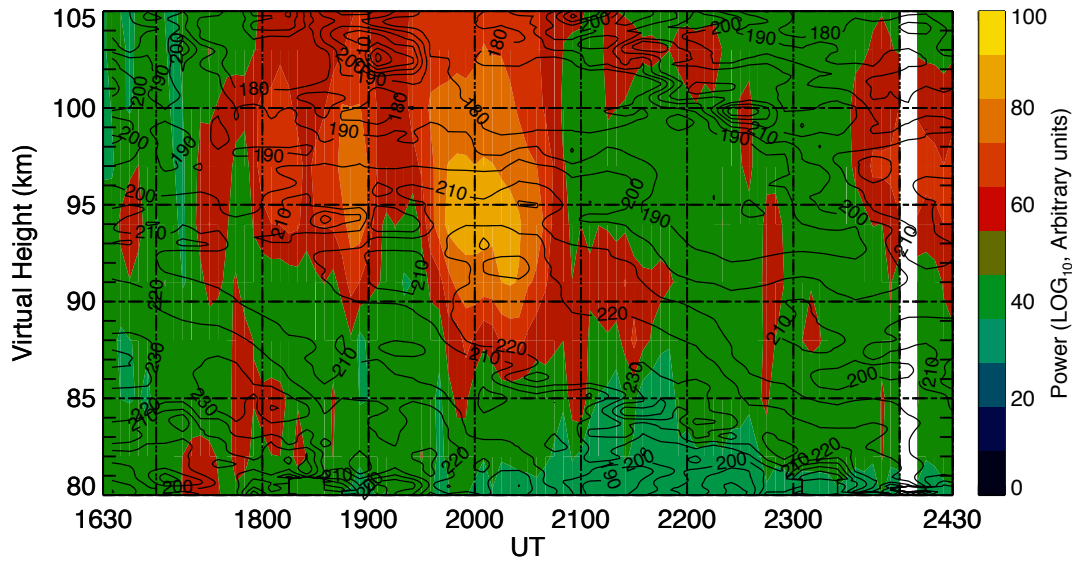


Figure 3.8 Variations of MF radar echo intensity from 80 to 105 km (in virtual height) between 16:30 and 24:30 UT on 29 October 2010. The black lines are contours of the neutral temperature (K) shown in Figure 3.1a.

3.2.3 GW Breaking

Atmospheric GW breaking/saturation result in turbulence and irregularities of the electron density. The backscatter echo power of MF radars depends on turbulence and sharp gradients of the electron density. Thus, the echo power can be used as a proxy of turbulent regions (cf. *Thrane et al.*, 1987). The observations were made during a very geomagnetically quiet interval; thus, the influence of auroral particle precipitation would be negligible. Figure 3.8 shows height-time variations of the backscatter echo power from 16:30 and 24:30 UT on 29 October 2010 together with contour lines of the neutral temperature shown in Figure 3.1a. Enhancements of the backscatter echo power are found from 18:00 to 21:00 UT above about 90 km, and the echo power decreased sharply after 21:00 UT. This suggests the presence of strong turbulence above 90-95 km between 18:00 and 21:00 UT. This region corresponds to the region where the Brunt-Väisälä frequency became lower and Ri was lower.

Figure 3.9 shows the sodium mixing ratio, which is the ratio of sodium density to neutral density as a function of altitude and time together with potential temperature between 16:30 and 24:30 UT on 29 October 2010. The mixing ratio was calculated in the same way as in the work of *Williams et al.* (2002), where the measured temperature was utilized to determine the total air density based on hydrostatic relation and ideal gas law (cf. *Liu et al.*, 2004). Potential temperature is defined

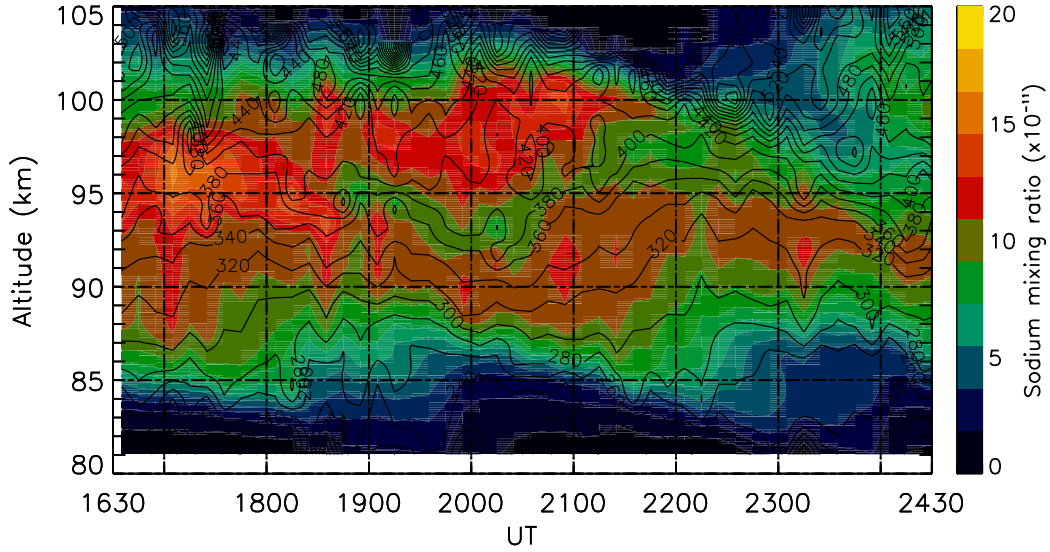


Figure 3.9 The color contours show the sodium mixing ratio ($\times 10^{-11}$) on 29 October 2010. The black lines are contours of the potential temperature (K).

as $T(t, z)(p(t_0, z_0)p^{-1}(t, z))^{\kappa^{-1}}$, where $T(t, z)$ is neutral temperature obtained by LIDAR as a function of time (t) and altitude (z), κ is the index of potential temperature ($= 2/7$), $p(t, z)$ is pressure as a function of time and altitude, and t_0 and z_0 are the reference time and altitude determined to be 20:30 UT and 81 km, respectively. $p(t_0, z_0)$ is given by

$$p(t_0, z_0) = n(t_0, z_0)k_b\bar{T}(z_0) \quad (3.11)$$

where $n(t_0, z_0)$ is given by MSIS-E-90 model (Hedin, 1991) and k_b is the Boltzmann constant ($= 1.38 \times 10^{-23} \text{ J K}^{-1}$). $\bar{T}(z_0)$ ($= 206 \text{ K}$) is the average value of the observed temperatures over the 8 h at 81 km. By assuming the hydrostatic equilibrium, we can calculate the pressure as follows:

$$p(t, z) = p(t_0, z_0) \exp\left(-\frac{g}{R} \int_{z_0}^z T(t, h)^{-1} dh\right) \quad (3.12)$$

where R ($= 287 \text{ J kg}^{-1} \text{ K}^{-1}$) is the gas constant (cf. Williams *et al.*, 2002). The atmospheric number density is then calculated from the ideal gas law:

$$n(t, z) = \frac{p(t, z)}{k_b T(t, z)} \quad (3.13)$$

The sodium mixing ratio shows a double peak structure between 18:00 and 21:30 UT. An overturning in the sodium mixing ratio should indicate that a wave is breaking or is about to break (*Hecht, 2004*). Possible causes of overturning features of the sodium density between 95 and 105 km were discussed by *Larsen et al. (2004)*. Though the causes are still not well understood, an overturning is a common characteristic of Kelvin-Helmholtz instabilities associated with large shears or the manifestation of GW breaking (*Larsen et al., 2004*)

To summarize the observational results, the region of the lower Richardson number above 95 km corresponds relatively well to regions of enhancements of MF radar echo power as well as to the overturning structure of the sodium mixing ratio. Therefore, the dissipation of the GW around 95 km before 21:00UT would probably be due to wave breaking caused by the instabilities.

3.2.4 Possible Caused of the Difference of the GW Propagation

Finally, we will briefly discuss what caused the difference between the two intervals, that is to say, why the GW did not dissipate after about 21:00 UT. We already demonstrated that the zonal wind, almost parallel to the wave propagation direction, did not change much, while the meridional wind changed direction below 91 km between the intervals, showing a more southward direction after 21:30 UT. The greater change in the meridional wind, however, did not occur above 90 km; thus, it is not be a major candidate mechanisms for the GW dissipating above 95 km. The semidiurnal tide is a dominant source of changing the wind and temperature in the polar upper mesosphere and lower thermosphere and reduces the stability on the topside of the positive temperature perturbation (cf. *Zhao et al., 2003*). We have derived semidiurnal tidal amplitude and phase using 48 h MR wind data obtained from 00:00UT on 29 October and 24:00UT on 30 October 2010 by using the Lomb-Scargle periodogram method, and we present them in Figure 3.10. The semidiurnal tidal amplitudes reached a maximum at 91 km for both the meridional and zonal components with values of ~ 16 and ~ 13 m s⁻¹, respectively, and minimized at 95-96 km. Since the phase jump is seen around 95 km, it appears that another mode grew above 95 km. Around 95 km, the semidiurnal tidal amplitudes were very small, and thus it seems that the semidiurnal tide did not significantly influence the GW propagation.

Figure 3.11 compares background conditions between the two intervals before and after 21:00UT. In the top panel, altitude profiles of the averaged temperature are compared, and it is found that the shapes of them differ. In particular, between 94 and

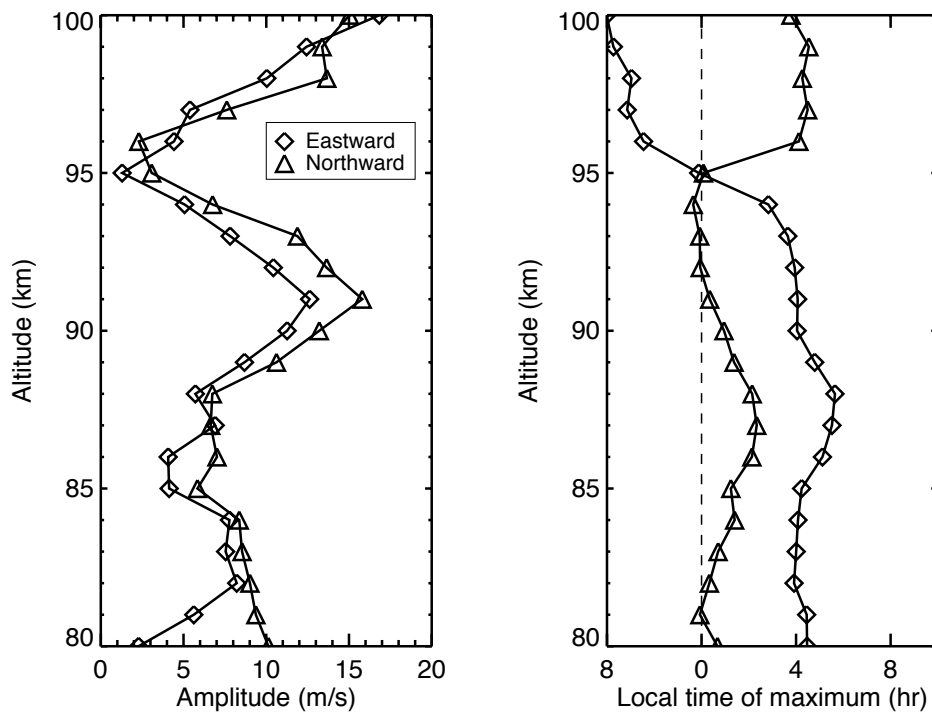


Figure 3.10 Altitude profiles of semidiurnal tidal amplitude (left) and local time of maximum (right). Diamonds and triangles denote eastward and northward components, respectively.

100 km, the negative temperature gradient (-4.4 K km^{-1}) existed before 21:00 UT, while after 21:00 UT the temperature was relatively constant (associated with small fluctuations) by height. This suggests that the atmosphere before 21:00 UT tended to become unstable more easily due to wave-induced temperature oscillation than in the later interval. In the middle panel, the neutral densities derived by Equation (3.13) are presented for comparison. The averaged neutral density before 21:00 UT is larger than that after 21:00 UT above 95 km, while between 85 and 95 km the opposite is true. The difference is presented more clearly in Figure 3.11c. In the bottom panel, the ratio of the neutral densities (thick line) as well as the pressure (thin line) derived by Equation (3.12) are presented. Between 85 and 95 km the averaged neutral density was larger by up to $\sim 3\%$ after 21:00 UT, while between 95 and 100 km it is larger by up to $\sim 10\%$ before 21:00 UT. The ratio of the pressure shows that higher pressure occurred above 87 km before 21:00 UT.

To summarize, during the earlier interval (i.e., before 21:00 UT), the neutral density and the pressure were higher up to ~ 10 and $\sim 7\%$ above 95 and 87 km, respectively

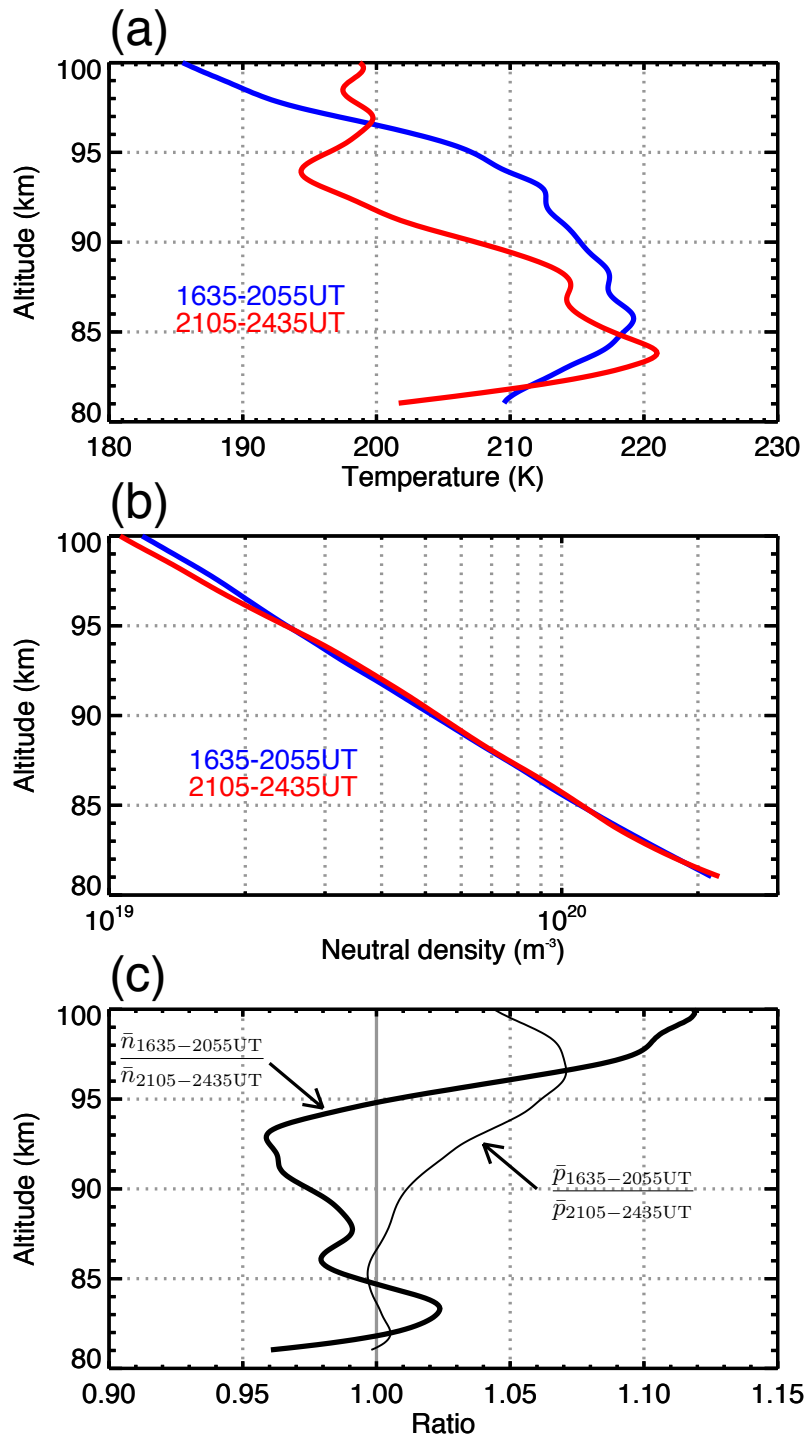


Figure 3.11 (a) Altitude profiles of the background temperature are compared for the two intervals between 16:30 and 21:00 UT and 21:00 and 24:30 UT. (b) Same as (a) but for the neutral density. (c) Ratios of neutral density (thick line) and pressure (thin line) between the two intervals.

and the steady negative slope of the temperature gradient existed above 94 km. It appears that these different background conditions would cause the difference of the GW propagation. We would suggest that, before 21:00UT between 85 and 94 km, the GW amplitude grew more significantly with increasing height than in the latter interval, that the GW reached around 95 km where the steeper negative temperature slope existed, and that the GW then broke down, generating the strong turbulence observed by MF radar. On the other hand, after 21:00 UT, the growth of GW amplitude was less below 95 km, and the background atmosphere was more stable (no negative temperature gradient) above 95 km and allowed the GW to propagate to upper heights.

3.3 Summary

A monochromatic GW was observed on 29 October 2010 with the sodium LIDAR operated at Ramfjordmoen, Tromsø, Norway (69.6°N, 19.2°E). The observational data were obtained during a geomagnetically very quiet interval ($Kp \leq 1$). The spectral as well as the hodograph analyses indicated that apparent period, intrinsic period, vertical and horizontal wavelengths, and maximum amplitude were 4 h, ~ 7.7 h, ~ 11.9 km, $\sim 1.38 \times 10^3$ km, and ~ 15 K, respectively, from 81 to 95 km. The GW dissipated at ~ 95 km height from 16:30 to $\sim 21:00$ UT, while the GW propagated further over 100 km from 21:00 to 24:30 UT. We evaluated three candidate mechanisms for the dissipation of the GW: critical level filtering, the convective, and dynamic instabilities. To evaluate critical-level filtering, we compared the background wind velocity and the phase velocity derived by the hodograph method. As a result of the analysis, we have found that the phase velocity is almost always greater than the background wind velocity, indicating that critical-level filtering did not play a role in this event. To evaluate the convective and dynamic instabilities, we calculated the Brunt-Väisälä frequency (N) and Richardson number (Ri). Before 21:00 UT and between 95 and 100 km, N^2 is lower and the negative N^2 appears to occur more frequently. There was an almost continual layer a few kilometers thick where the Ri is smaller (≤ 2) between 95 and 100 km before 21:20 UT, implying that the dynamic instabilities would occur, considering poorer height and horizontal and temporal resolutions of the MR wind data. Because we found enhancements of MF radar power echo before 21:00 UT and an overturning structure of the sodium mixing ratio between 18:30 and 21:30 UT, we concluded that the GW dissipated due to wave breaking caused by the instabilities before $\sim 21:00$ UT.

We investigated differences of background atmosphere for the two intervals between 16:30 and 21:00 and 21:00 and 24:30 UT. The most prominent difference is that there was a steady negative slope of the averaged temperature (-4.4 K km^{-1}) between 94 and 100 km before 21:00 UT. We propose that the difference in the temperature profile above 94 km is a probable cause of the change in the GW propagation. We need further data sets to investigate this issue in more detail. Since October 2012, the sodium LIDAR at Tromsø has observed wind data together with neutral temperature and sodium density data along with five directions (usually, vertical, north, south, east, and west). Thus, we can conduct similar studies in the near future but using wind data with higher height and narrower spatial resolution.

Chapter 4

Generation Mechanisms of the Sporadic Sodium Layer During a Night of High Auroral Activity

In this section, we have evaluated generation mechanisms of an SSL appearing in the polar MLT region for the night of 22 January 2012 by using data obtained with the sodium LIDAR, the EISCAT UHF radar, the meteor radar, an all-sky digital camera, and the 3-wavelength photometer operated at the same observational field. The 3-hour Kp index was 4+, 4–, 5– and 5– between 15:00 UT on 22 January and 03:00 UT on 23 January 2012. The aurora activity was high through the night. The result of this Chapter have been reported by *Takahashi et al.* (2015).

4.1 Observational Results

In this section, we describe observational results obtained by the sodium LIDAR, the EISCAT UHF radar (vertical position) and the photometer. Since the photometer was pointed at the field-aligned position, the volume of the photometer observation was about 22 km southward from the vertical observation at a 100 km altitude. Figures 4.1a and 4.1b show temporal and altitude variations of the sodium density and the neutral temperature, respectively, from 16:00 UT on 22 January to 04:00 UT on 23 January 2012 obtained by the sodium LIDAR. The sodium density and the neutral temperature were derived with 2 min temporal and about 0.5 km altitude resolution (smoothing in altitude with Hanning window). From Figure 4.1a, we can identify a peculiar region with higher sodium density at 93-94 km between 21:18 and 21:36

UT above a normal sodium layer located at about 80-90 km. After 21:40 UT there is a thinner sodium density layer at around 95-97 km, which gradually descended to about 90 km until 24:00 UT. These higher sodium density regions are thought to be so-called SSLs, and we mainly focus on generation mechanisms of the SSL appearing at 93-94 km in this paper.

From Figure 4.1b, below 90 km, the neutral temperature varied from about 210 to 260 K. There seemed to be a lower temperature region around 92-98 km between 20:00 and 22:00 UT, indicating that the SSL appeared in the lower temperature region. Due to quick temporal and large altitudinal variations of the sodium density, the temperature values around and inside the SSL region could be unreliable, and we have derived the values with higher temporal resolution and present the results later in this session.

Figures 4.1c, 4.1d and 4.1e show temporal and altitude variations of the electron density and emission intensities at 427.8 nm and 557.7 nm obtained by the EISCAT UHF radar in the vertical position and the photometer with the field-aligned position, respectively. The photometer measurements clearly showed that auroral particle precipitation intermittently occurred throughout the night, and the electron density profile indicated that the auroral particle precipitation often reached 95 km and below, indicating frequent precipitation of high energy (greater than 30 keV) particles (cf. *Rees*, 1963).

In addition to the auroral ionizations, there are two layered structures associated with relatively high electron density of over 10^{10} m^{-3} appearing between 20:00 and 24:00 UT. Although auroral ionization contaminated their identification, the upper layer appeared at about 105 km at 20:00 UT, gradually descended, and stayed at around 94 km between 21:18 and 21:40 UT, ascended and reached about 97 km at 21:50 UT, and again descended to 88 km as the time went by. The lower layer appeared at 90 km at 19:30 UT and descended and reached at 87 km at 20:00 UT and stayed there until 24:00 UT. These layers were likely sporadic *E* (*Es*) layers consisting of metal ions (Fe^+ , Ca^+ , Na^+ etc.) and electrons.

Figure 4.2a shows variations of the sodium density as well as the altitude of the maximum sodium density from 20:00 to 24:00 UT between 90 and 100 km with 2 min and 0.5 km resolution (smoothing in altitude with Hanning window). Figures 4.2b and 4.2c present temporal variations of the maximum sodium density of the SSL and the ratio of the maximum sodium density to the background normal sodium density at the same altitude, respectively. The background normal sodium density is the averaged value between 16:00 and 19:00 UT at each altitude when the sodium

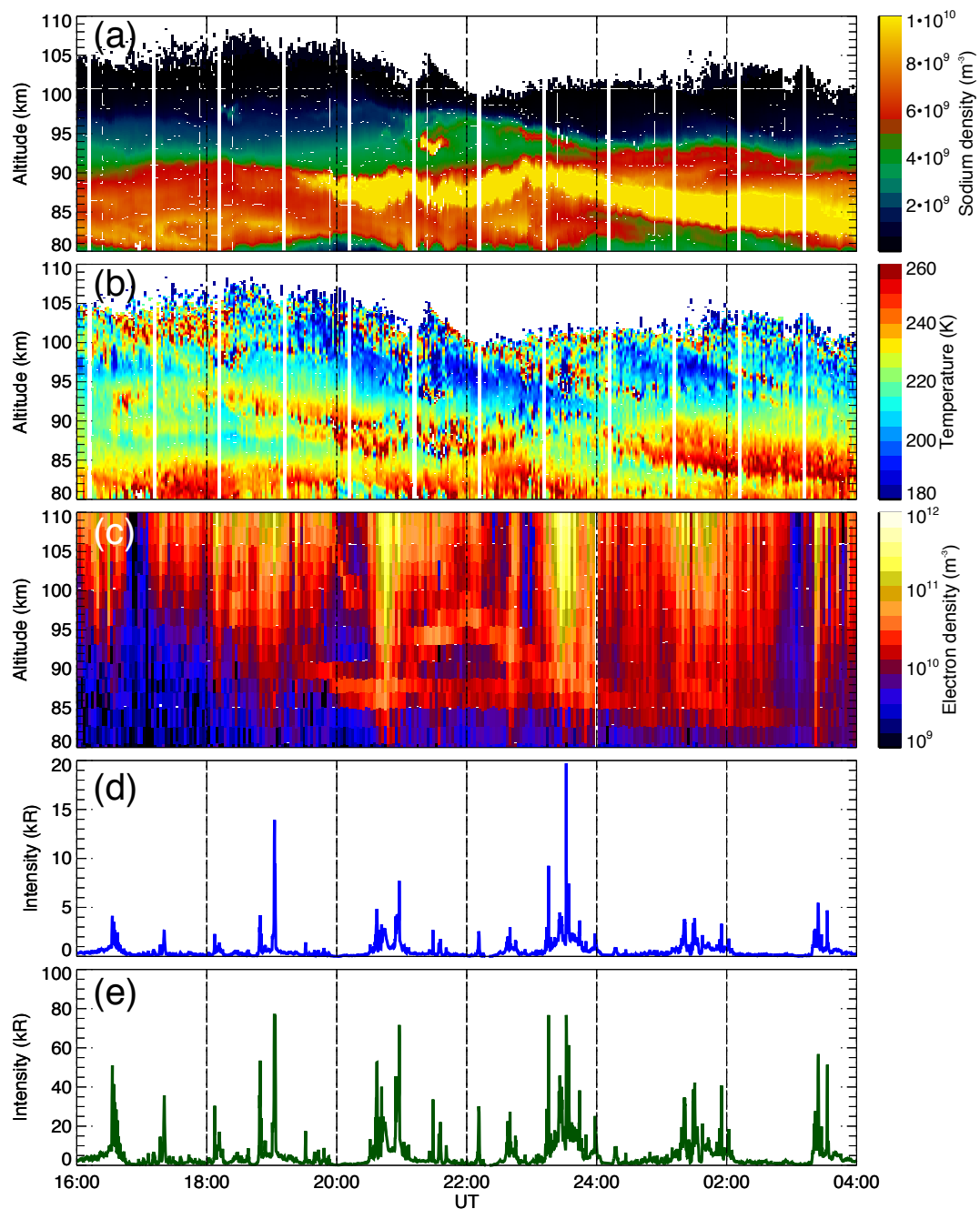


Figure 4.1 Variations of the sodium density (a), the neutral temperature (b), and the electron density (c), the emission intensity (10 sec averaged values) of 427.8 nm (d) and 557.7 nm (e) from 16:00 UT on 22 January to 04:00 UT on 23 January are shown. The temporal and altitude resolution in (a) and (b) is 2 min and 0.5 km and in (c) is 30 sec and about 2.2 km, respectively.

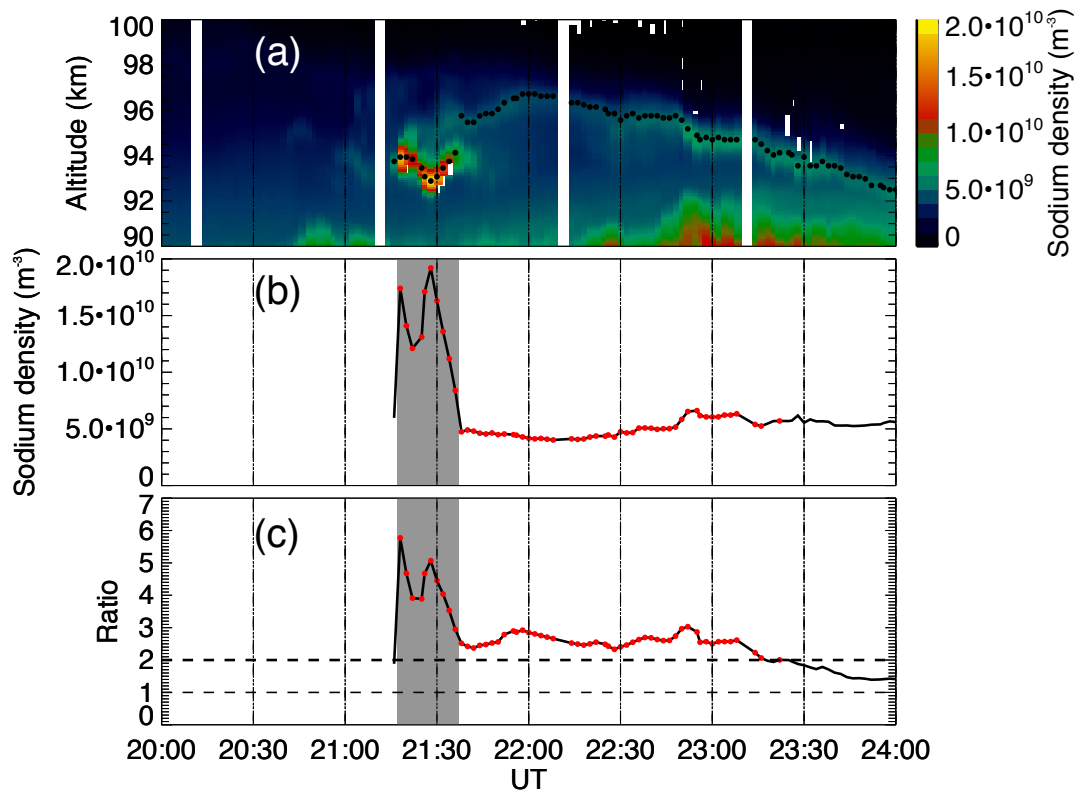


Figure 4.2 (a) Variations of the sodium density from 20:00 to 24:00 UT on 22 January 2012 between 90 and 100 km are presented. Black dots denote altitudes of the maximum density of the SSL(s). (b) The maximum sodium density of the SSL(s). (c) The ratio of the maximum sodium density to the background sodium density at the same altitude. Red dots in (b) and (c) denote data values with the ratio greater than 2. In this study, we mainly focus on the SSL occurring for time intervals shown in the gray shade (i.e. 21:18 and 21:36 UT).

density varied smoothly with time. The ratio rapidly increased from 1.9 to 5.8 for 2 min from 21:16 to 21:18 UT. In this study, the SSL was defined by stating that the ratio of the maximum density to the background normal density is greater than 2 (cf. *Simonich, 2005*).

The maximum altitude of the SSL descended by 1 km to about 93 km at 21:28 UT when the sodium density maximized, and ascended by 1 km to about 94 km from 21:30 to 21:36 UT. At around 21:38 UT, another SSL appeared at around 97 km. After 22:00 UT, the maximum altitude of the SSL gradually descended and reached about 92 km at 24:00 UT. The sodium density inside the first SSL rapidly increased from $\sim 6.0 \times 10^9 \text{ m}^{-3}$ to $\sim 1.7 \times 10^{10} \text{ m}^{-3}$ in 2 min between 21:16 and 21:18 UT. After the first sudden enhancement, the sodium density inside the SSL decreased to

$1.2 \times 10^{10} \text{ m}^{-3}$ at 21:22 UT, and again increased to $\sim 1.9 \times 10^{10} \text{ m}^{-3}$ at 21:28 UT. From 21:28 UT to 21:36 UT, the sodium density of the SSL gradually decreased from $1.9 \times 10^{10} \text{ m}^{-3}$ to $8.0 \times 10^9 \text{ m}^{-3}$; at 21:38 UT the ratio of the maximum sodium density to the background sodium density became lower than 2. The FWHM of the SSL at 21:28 UT was ~ 1.1 km. At 21:38 UT, another SSL appeared at 97 km. The maximum sodium density of the later SSL was lower than that of the earlier one, but between 21:40 UT and 23:00 UT the maximum sodium density was still a few times higher than that of the background.

The sodium density inside the SSL observed from 21:18 to 21:36 UT drastically changed with time and altitude, thus the derivation of the temperature requires high spatial and temporal resolution. The sodium LIDAR at Tromsø has recorded signals every 5 sec and switched the frequencies every 1 min. Since data obtained during the frequency-switching interval has to be removed due to possible mixture of the two frequency data, we have derived the temperature with 15 sec temporal and 96 m altitude resolution every 1 min.

Figure 4.3 compares the altitude profile of the sodium density and the neutral temperature derived with a 15 sec temporal and 96 m altitude resolution. For temperature data, 1 km running averaged values are presented every 96 m. The enhancement of the sodium density began at 21:17 UT around 94 km. The maximum density altitude was located at the local temperature minimum at 21:17 UT, 21:19 UT and 21:20 UT in contrast to *Gardner et al.* (1993), who pointed out that the SSL was located in the higher temperature region. Although at times the temperature increased inside or nearby the SSL, no trend of temperature can be seen inside the SSL. Considering possible variations of temperature due to atmospheric waves, we can conclude that the SSL in this event was not located in an enhanced temperature region.

Figure 4.4 shows all-sky images from 20:00 UT to 22:00 UT. From 20:00 UT to 20:20 UT, auroral arcs were located on the southern side of the all-sky images. At 20:25 UT, poleward expansion due to auroral breakup occurred. The bright part of auroral arcs reached at the zenith of Tromsø at 20:40 UT. From 21:18 to 21:36 UT when the sodium LIDAR observed the SSL, auroral arcs passed over the zenith, the lowest height level in which the EISCAT radar detected the ionization for the time interval was around 100 km, which was clearly higher than the top of the SSL according to Figures 4.1a and 4.1c. These results imply that the auroral precipitation is unlikely for making a large contribution to generation of the SSL analyzed in this study.

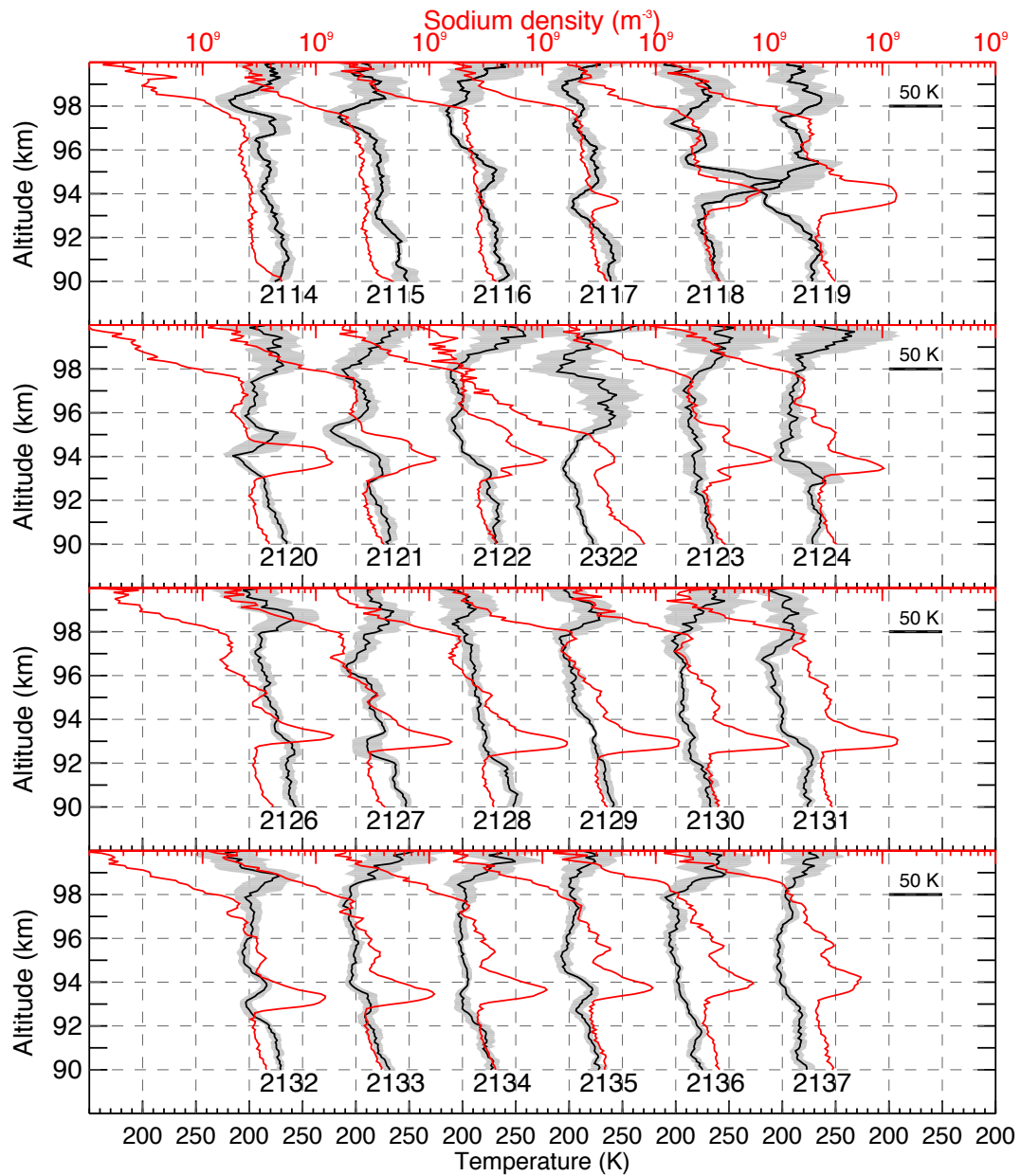


Figure 4.3 Altitude profiles of sodium density (red line) and neutral temperature (black line) from 21:14 UT to 21:37 UT every 1 min on 22 January 2012 are presented. These values are derived with a 15 sec temporal and 96 m height resolution. A 1 km running average is applied to the temperature profile. The gray shade shows standard deviations of the temperature data (1 sigma)

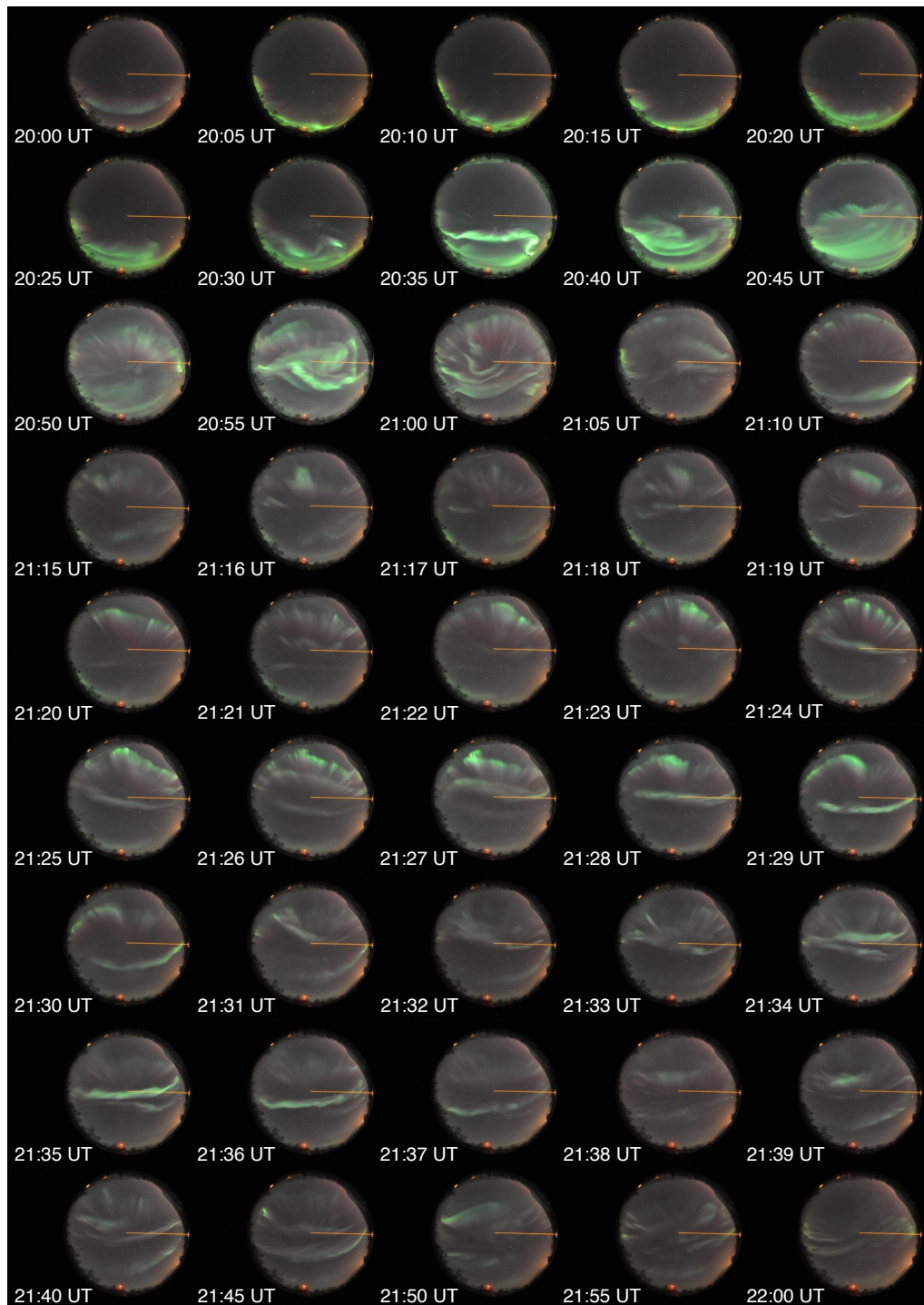


Figure 4.4 All-sky images obtained with the digital camera. The images obtained between 21:15 and 21:40 UT on 22 January 2012 are shown every 1 min, while the images between 20:50 and 20:15 UT and between 21:40 and 22:00 UT are shown every 5 min.

4.2 Discussion

Much attention has been paid to the generation mechanisms of SSLs for about 35 years, since *Clemesha et al.* (1978) first reported an SSL. Possible proposed candidates are supply of sodium atoms from an *Es* layer, an effect of the electric field (downward ion motion), chemical reactions due to local temperature enhancements, meteor absorption, and auroral particle spattering (cf. *Kane et al.*, 1993; *Heinselman*, 2000; *Kirkwood and von Zahn*, 1991; *Gardner et al.*, 1993; *Clemesha et al.*, 1988; *von Zahn and Hansen*, 1988). The key points to fulfill are how to supply enhanced sodium atoms and how to make a thin layer structure with a large horizontal extent. Supply of sodium atoms from an *Es* layer has been considered the most possible generation mechanism. *Kane et al.* (1993) argued that an *Es* layer triggered the release of sodium atoms, but the *Es* layer was not the major source of the SSL observed at Arecibo. This is because it is often the case that the number of sodium ions contained in an *Es* layer is not enough for generation of an SSL by comparison of IS radar and LIDAR observations.

4.2.1 Production From the *Es* Layer

As shown in Figure 4.1c, the two *Es* layers appeared between 80 and 110 km between approximately 2000 and 2400 UT on 22 January 2012. Figure 4.5a compares maximum density altitudes of the SSL and the upper *Es* layer. When the SSL appeared at 21:18 UT, the SSL was located at almost the same altitude of the upper *Es* layer (observed in the vertical direction of the EISCAT UHF radar). The maximum altitude of the SSL descended and then ascended between about 93 and 94 km between 21:18 and 21:36 UT, while the *Es* layer remained at 94 km. During the time interval, the difference of the altitudes between the *Es* layer and the SSL was about 1 km at largest. Thus we can propose that the SSL and the *Es* layer were located at the same altitude considering the worse altitude resolution (2.2 km) of the EISCAT measurements. This implies that the *Es* layer contributed to the generation of the SSL (to some extent). Furthermore, the *Es* layer was observed at almost the same altitude as three positions of the EISCAT measurements, suggesting the *Es* layer and (probably) the SSL extended at least 36 km in a horizontal direction. Figure 4.5c shows the ratio of the sodium density to the electron density. The ratio varied from 0.56 to 0.27 between 21:18 and 21:30 UT. Figure 4.5d shows column densities integrated between 92 and

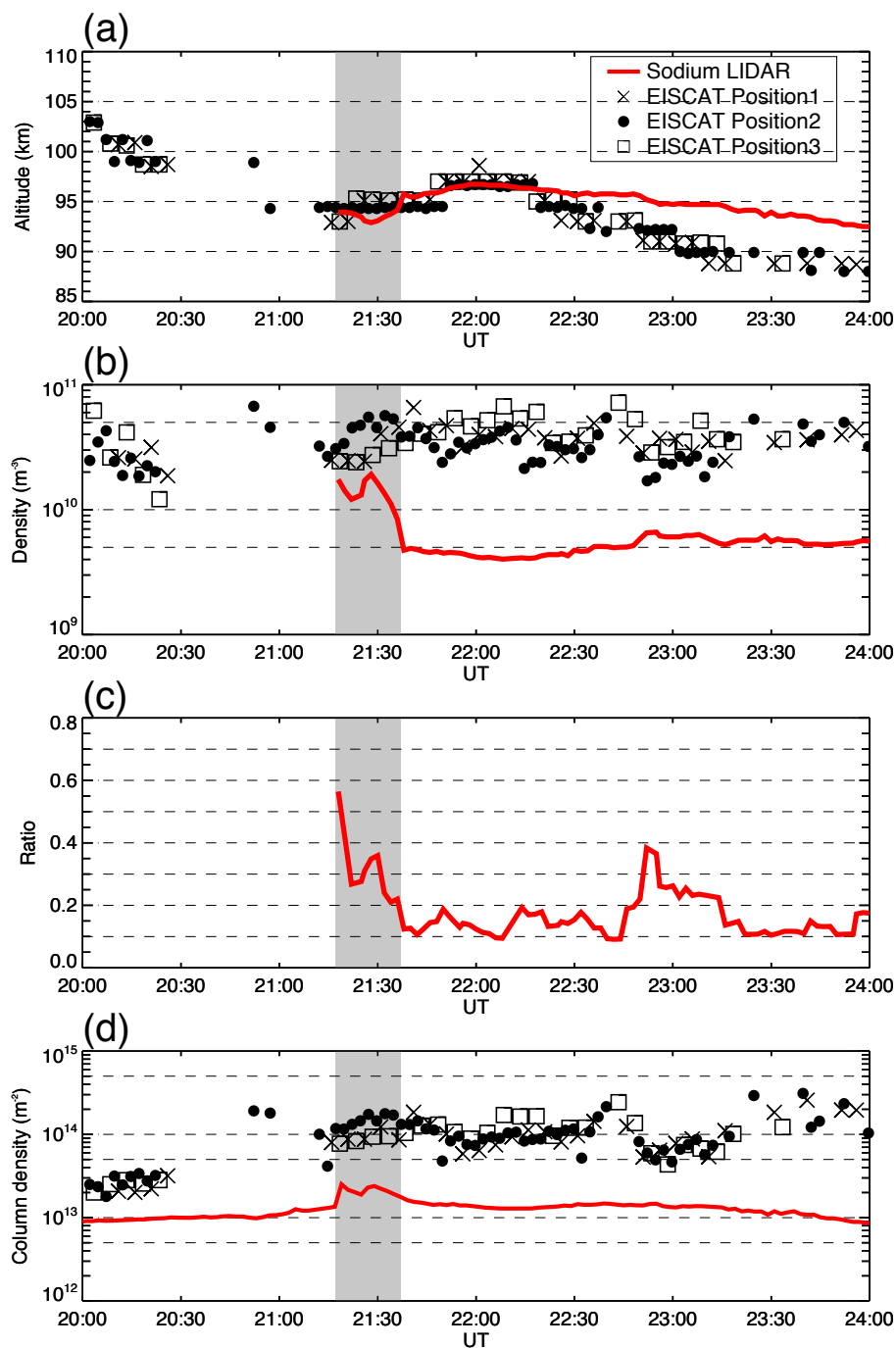


Figure 4.5 (a) Variations of altitudes of the maximum SSL (red line) and the E_s layer for three different directions (square, closed circle, and triangle) of the EISCAT UHF radar measurements are compared. Shade area denotes the time interval when the SSL was seen. (b) Same in (a) except for the density. (c) Variations of the ratio of the maximum sodium density of the SSL to the maximum electron density in the E_s layer (in the vertical position of the EISCAT measurements) are shown. (d) Comparison of column densities integrated between 92 and 97 km are shown.

97 km of the electron densities and sodium densities. An increase of the sodium column density requires source(s) of sodium atoms (cf. *Simonich, 2005*).

The conversion of sodium ions in an *Es* layer to sodium atoms through a charge exchange process or clustering reactions has been discussed as a major source of high density SSLs appearing between 90 and 100 km (*von Zahn and Hansen, 1988*). Some in-situ measurements suggest that sodium ion abundance is several percent of the total abundance of electron density. *Kane et al. (1993)* estimated that the sodium ion abundance in an *Es* layer was 10% at maximum. Figure 4.5b shows variations of sodium density and electron density. The averaged maximum electron density from 20:00 to 21:18 UT was $3.0 \times 10^{10} \text{ m}^{-3}$ with a standard derivation of $1.3 \times 10^{10} \text{ m}^{-3}$. The averaged maximum sodium density of the SSL from 21:18 UT to 21:36 UT was $1.4 \times 10^{10} \text{ m}^{-3}$ with a standard derivation of $3.2 \times 10^9 \text{ m}^{-3}$. When we assume that the *Es* layer contained sodium ions with 10 percent of the total ions (cf. *Hansen and von Zahn, 1990; Kane et al., 1993*), the amount of the sodium ions was $3.0 \times 10^9 \text{ m}^{-3}$, which corresponds to about only 21% of the averaged maximum sodium density of the SSL. This result indicates that the *Es* layer alone could not provide enough supply of the sodium atoms in this event, but probably contributed to the generation to some extent.

4.2.2 Concentration From a Sodium Ion Layer by Electric Field

Kirkwood and von Zahn (1991) proposed a possibility for concentration of metallic ions by the electric fields. *Plane (2004)* proposed that Na^+ distributes around the topside of a sodium layer as a reservoir of the sodium layer and its shape is the Gaussian distribution with an altitude of maximum density of about 105 km. We evaluate effects of the electric field for Na^+ .

Figure 4.6 shows the direction and the strength of the electric field derived by the EISCAT UHF radar data with a 10 min resolution from 18:00 and 24:00 UT on 22 January 2012. Before 20:00 UT, the direction of the electric field fluctuated between the north, west, and south with a strength of 25 mV m^{-1} or less. From 20:20 to 21:30 UT, the direction gradually changed from the south through the west to the north-west with the intensity of $17\text{-}45 \text{ mV m}^{-1}$. The south-westward electric field works most effectively for downward motion of ions below 120 km (*Oyama et al., 2012*). From 21:30 to 22:40 UT, the direction of the electric field changed from the north-west to the south with the intensity of $10\text{-}60 \text{ mV m}^{-1}$, and from 22:40 UT to 24:00 UT the direction was approximately southward.

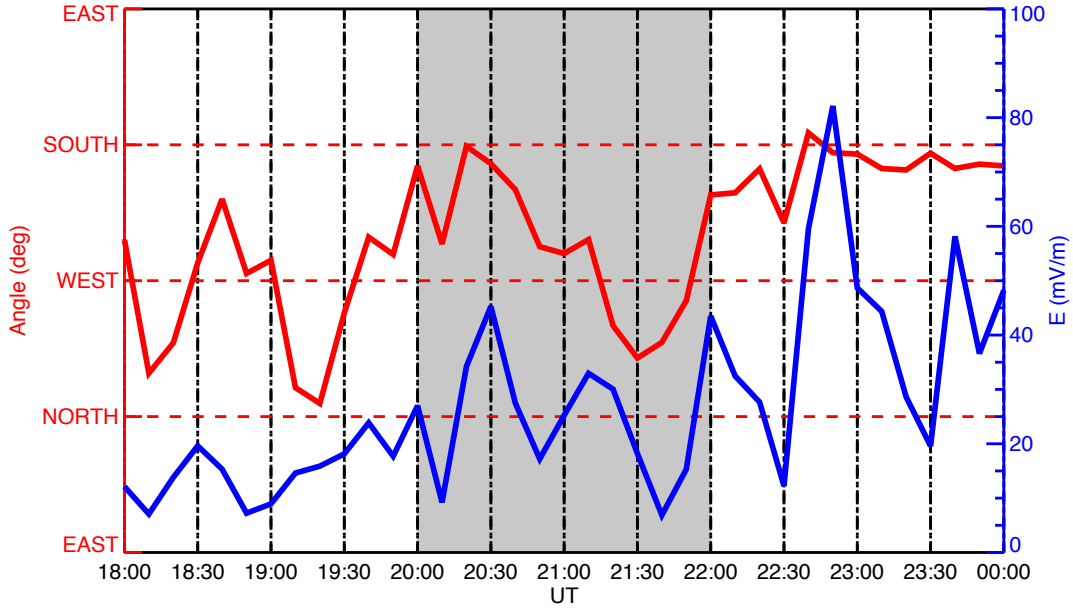


Figure 4.6 Temporal variations of the direction (red line) and the strength (blue line) of the electric field derived by the EISCAT UHF radar from 18:00 to 24:00 UT on 22 January 2012 are shown.

To evaluate effects of the electric field, we have calculated its contributions based on continuity equation in the vertical direction:

$$\frac{dn_{si}(z)}{dt} = q_{si}(z) - L_{si}(z) - \frac{d}{dz}(n_{si}(z)v_{si}(z)) \quad (4.1)$$

where $n_{si}(z)$ is sodium ion density at height z , $q_{si}(z)$ is the sodium ion production rate, $L_{si}(z)$ is the sodium ion loss rate, and $v_{si}(z)$ is the vertical sodium ion velocity and is counted positively upwards. The vertical sodium ion velocity is expressed as (cf. *Kirkwood and von Zahn, 1991*):

$$\begin{aligned} v_{si}(z) = & \frac{\Omega_{si}v_{in}(z)}{\Omega_{si}^2 + v_{in}^2(z)} \left(\frac{E_N}{B_0} \sin I + W_E(z) \right) \cos I \\ & + \frac{\Omega_{si}^2}{\Omega_{si}^2 + v_{in}^2(z)} \left(\frac{E_E}{B_0} - W_N(z) \sin I \right) \cos I \\ & + \left(1 - \frac{\cos^2 I \Omega_{si}^2}{\Omega_{si}^2 + v_{in}^2(z)} \right) W_Z(z) \end{aligned} \quad (4.2)$$

where Ω_{si} is sodium ion gyro frequency, v_{in} is ion neutral collision frequency (given from equation [2.29a] by *Kelley, 2009*), I is the inclination of the earth's magnetic

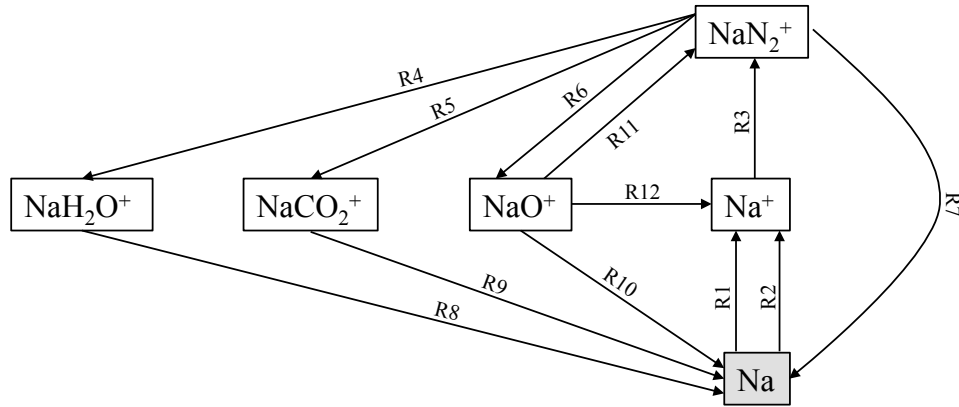
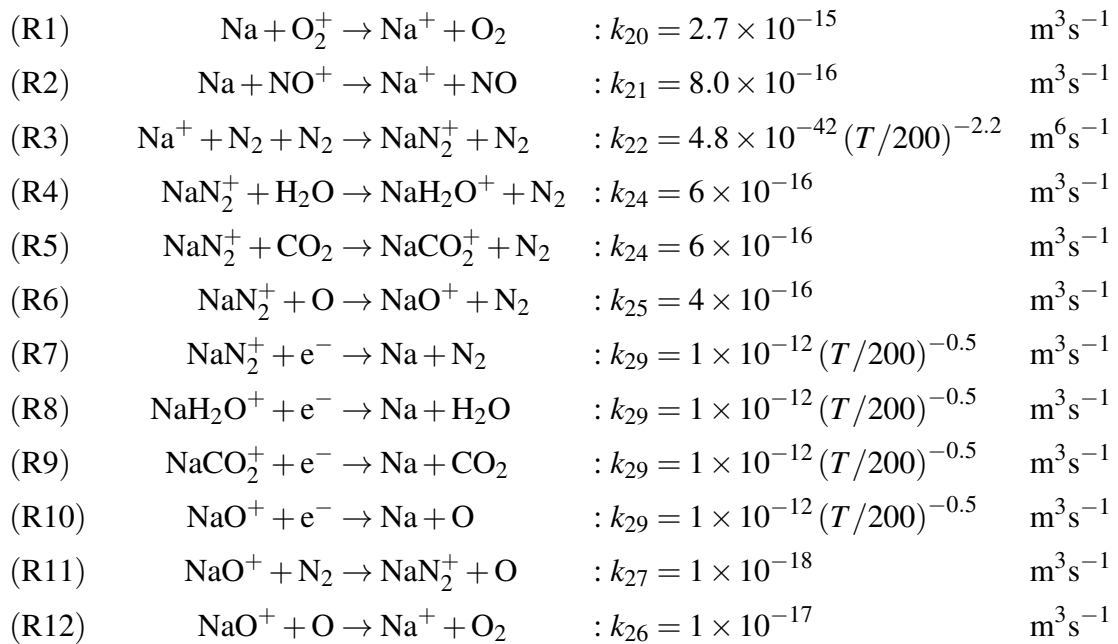


Figure 4.7 Schematic drawing of circular reactions among Na, Na⁺, NaN₂⁺, NaO⁺, NaH₂O⁺, and NaCO₂⁺.

field obtained with IGRF geomagnetic model ($I = 78.1^\circ$ at Tromsø at 100 km), E_N and E_E are the northward and eastward components of the electric field, $W_N(z)$, $W_E(z)$, and $W_Z(z)$ are the northward, eastward and upward components of the neutral wind, and B_0 is the strength of the earth's magnetic field. *Kirkwood and von Zahn* (1991) simulated Fe⁺ development based on the continuity equation, but they used the continuity equation without the ion production and the ion loss rate. Because related chemical reactions cannot be negligible below about 100 km, the ion production and the loss rate in the continuity equation are included in this study. The schematic chemical reactions in a sodium layer is shown in Figure 4.7.



where T is the temperature. In this study, we calculate density developments of sodium atoms, sodium ions, NaN_2^+ , NaCO_2^+ , NaH_2O^+ , and NaO^+ by numerical analysis of the following equations:

$$\begin{aligned} \frac{d[\text{Na}]}{dt} = & k_{29}[\text{NaN}_2^+][e^-] + k_{29}[\text{NaO}^+][e^-] + k_{29}[\text{NaCO}_2^+][e^-] \\ & + k_{29}[\text{NaH}_2\text{O}^+][e^-] - k_{20}[\text{Na}][\text{O}_2^+] - k_{21}[\text{Na}][\text{NO}^+] \end{aligned} \quad (4.3)$$

$$\begin{aligned} \frac{d[\text{Na}^+]}{dt} = & k_{20}[\text{Na}][\text{O}_2^+] + k_{21}[\text{Na}][\text{NO}^+] + k_{26}[\text{NaO}^+][\text{O}] \\ & - k_{22}[\text{Na}^+][\text{N}_2][\text{N}_2] \end{aligned} \quad (4.4)$$

$$\begin{aligned} \frac{d[\text{NaN}_2^+]}{dt} = & k_{22}[\text{Na}^+][\text{N}_2][\text{N}_2] + k_{27}[\text{NaO}^+][\text{N}_2] - k_{29}[\text{NaN}_2^+][e^-] \\ & - k_{25}[\text{NaN}_2^+][\text{O}] - k_{24}[\text{NaN}_2^+][\text{CO}_2] - k_{24}[\text{NaN}_2^+][\text{H}_2\text{O}] \end{aligned} \quad (4.5)$$

$$\begin{aligned} \frac{d[\text{NaO}^+]}{dt} = & k_{25}[\text{NaN}_2^+][\text{O}] \\ & - k_{26}[\text{NaO}^+][\text{O}] - k_{27}[\text{NaO}^+][\text{N}_2] - k_{29}[\text{NaO}^+][e^-] \end{aligned} \quad (4.6)$$

$$\frac{d[\text{NaCO}_2^+]}{dt} = k_{24}[\text{NaN}_2^+][\text{CO}_2] - k_{29}[\text{NaCO}_2^+][e^-] \quad (4.7)$$

$$\frac{d[\text{NaH}_2\text{O}^+]}{dt} = k_{24}[\text{NaN}_2^+][\text{H}_2\text{O}] - k_{29}[\text{NaH}_2\text{O}^+][e^-] \quad (4.8)$$

The initial condition of an altitude profile of sodium atoms is given by the averaged profile between 16:00 and 19:00 UT. For Na^+ , a Gaussian distribution is assumed with a maximum altitude of 105 km, its FWHM of 10 km, and its peak density of $3.5 \times 10^9 \text{ m}^{-3}$ after *Plane* (2004). Additional sodium ions from *Es* layer are included: the amount is 10% of the electron density at 104 km. The initial condition for NaCO_2^+ is assumed with one-tenth of the density of Na^+ at 2000 UT. The initial condition of densities of NaN_2^+ , NaH_2O^+ , and NaO^+ are assumed to be zero. We assumed the molecular ion abundance (e.g. 77% $[\text{NO}^+]$ and 17% $[\text{O}_2^+]$ at 94 km) of the total electron density (obtained by the EISCAT UHF radar measurements) with a reference of the IRI model (*Bilitza*, 2001) outside the *Es* layer (in particular, during auroral particle precipitation intervals [e.g. around 20:57 UT]), while 10% (NO^+) and 1% (O_2^+) were assumed in the *Es* layer: the latter assumption values are somewhat arbitrary. It should be pointed out that the molecular ions (NO^+ and O_2^+) work on the loss of sodium atoms through reactions of (R1) and (R2). The neutral densities of major species (e.g. N_2 , O_2 , O) are given by MSIS-E-90 Atmosphere Model (*Hedin*,

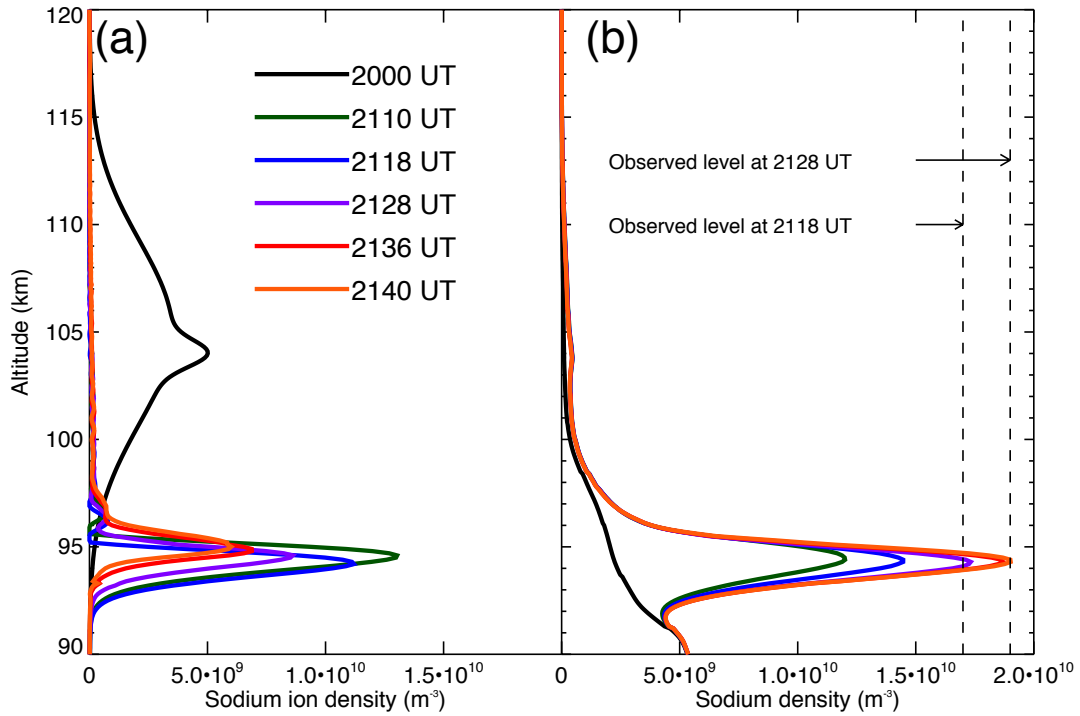


Figure 4.8 Temporal developments of sodium ions (a) and sodium atoms (b) are illustrated.

1991). The densities of CO_2 and H_2O are given as follows (Allen, 1965):

$$[CO_2] = (3 \times 10^{-4}/0.7811)[N_2] \quad (4.9)$$

$$[H_2O] = (5 \times 10^{-7}/0.7811)[N_2] \quad (4.10)$$

The calculation started at 20:00 UT. The number density of each species was calculated with a time step of 1 min and vertical resolution of 0.1 km between 80 and 120 km until 22:00 UT. Figures 4.8a and 4.8b illustrate temporal variations of density profiles of sodium ions and sodium atoms, respectively. In this calculation, the electric field values, horizontal wind velocity values (above 100 km), and the electron density values are given from the EISCAT measurements, horizontal wind velocities at and below 100 km are given from MR data. Neutral temperature values at and below 100 km are given by the sodium LIDAR measurement, while above 100 km given by MSIS-E-90 Atmosphere Model. The vertical wind velocity was assumed to be zero over the height region.

Figure 4.8a shows a temporal development of the redistribution of sodium ions. At 21:18 UT, the altitude of maximum sodium ions reached 94.2 km, and the maximum

sodium ion density decreased with time after 20:45 UT, indicating the transportation from sodium ions to sodium atoms. Since N_2 density increases exponentially with decreasing altitude, the conversion of sodium ions to sodium atoms enhances with decreasing altitude. Furthermore, the altitude of the maximum sodium ion density ascended from 21:20 to 21:40 UT by about 2 km.

Figure 4.8b shows that the calculation suitably produced a thin layer with high sodium density with FWHM of about 2 km. The sodium density steadily increased from 21:10 to 21:40 UT. The sodium density was enhanced from $2.4 \times 10^9 \text{ m}^{-3}$ at 20:00 UT to $1.5 \times 10^{10} \text{ m}^{-3}$ at 21:18 UT at 94.4 km. The value at 21:18 UT corresponds to about 88% of the observed value at 94 km, and at 21:28 UT the calculated density of the sodium atom was $1.7 \times 10^{10} \text{ m}^{-3}$, which was about 89% of the observed value. The calculation shows the maximum sodium density reached $1.9 \times 10^{10} \text{ m}^{-3}$ at 21:40 UT, which was about the same as the observed maximum sodium density at 21:28 UT. Although the calculation, which mainly used observational values, did not completely reproduce the observational results, some important features (e.g. a thin layer, a maximum sodium density altitude, and an enhanced sodium density) were well produced. Therefore, we propose that (1) the major source was sodium ions in a normal sodium ion layer, and (2) the electric field played a major role in generating the SSL in this event.

4.2.3 Effect of Temperature

Figure 4.9 compares sodium column density and mean neutral temperature between 92 and 97 km derived with 15 sec temporal and 96 m altitude resolution. The mean temperature decreased from 18:00 to 20:45 UT, while the sodium column density gradually increased. The mean temperature increased from 20:45 to 21:00 UT, and decreased again from 21:00 to 22:00 UT. After about 22:00 UT, the mean temperature increased and the sodium column density tended to decrease. The background temperature between 20:30 and 23:30 UT was lower by about 20 K than those for the other intervals. Thus there was a tendency that the background temperature was in inverse proportion to sodium column density. Since the sodium production is in inverse relation to the background neutral temperature (R7, R8, R9, R10), the background temperature condition seemed to support the generation of the SSL in this event. The calculation also supports the idea that when the temperature was set to be constant (230 K), the calculated maximum sodium density was reduced by about 6% from the value of the calculation using the real temperature conditions.

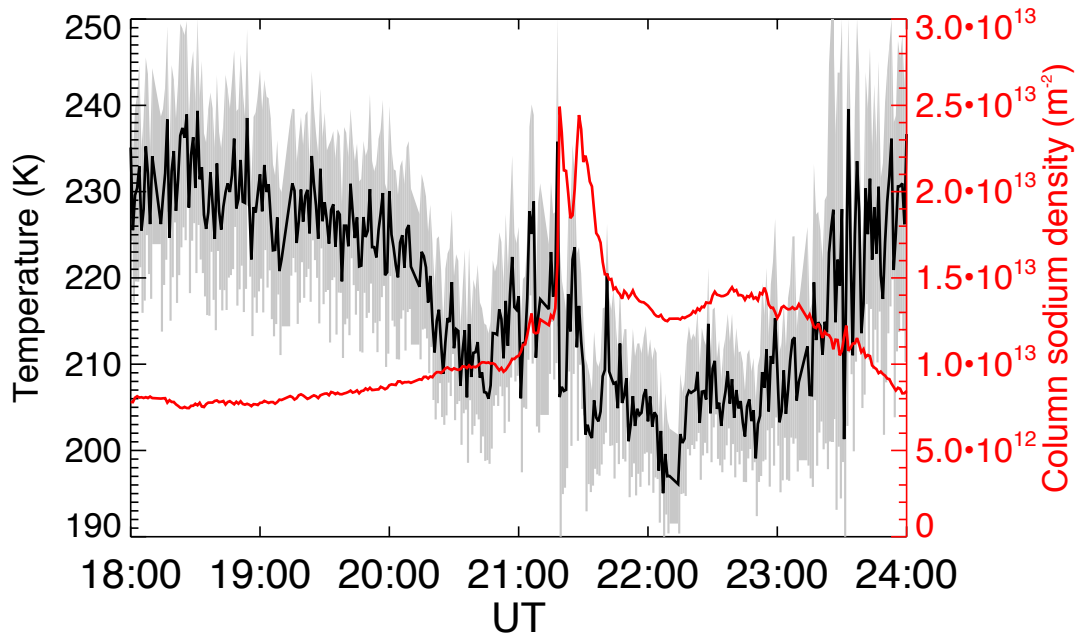


Figure 4.9 Comparison of sodium column density (red line) and mean temperature (black line) between 92 and 97 km every 1 min. The sodium density and the temperature are derived with 15 sec temporal and 96 m height resolution. The gray shading denotes standard deviations of the mean temperature.

4.2.4 Meteor Absorption and Auroral Particle Spattering

Figure 4.10 shows variations of the meteor count observed by MR at Tromsø from 12:00 to 24:00 UT on 22 January 2012. Monthly averaged values for January 2012 are also illustrated for comparison. Figure 4.10 shows no remarkable increase of the meteor count between 12:00 and 24:00 UT, in particular around 21:00 UT on 22 January 2012. Moreover, the temporal variation of the meteor count for 22 January is similar to that of the monthly average, but the number of counts was lower than the monthly averaged values. These results imply that the meteor shower did not occur during this time interval. If a cosmic bombardment with a mass of over 100 kg comes into the atmosphere, it must be detected as a bright trail by an all-sky digital camera. Such a bright trail was not seen in images operated at the same observational field. Therefore, we can exclude the possibility of the effect of meteors and/or meteor showers.

According to *von Zahn and Hansen* (1988), auroral particles with energy of higher 40 keV may provide sodium atoms from dust particles. Figure 4.1c showed that the electron density was enhanced at 20:57 UT below 90 km due to auroral particle

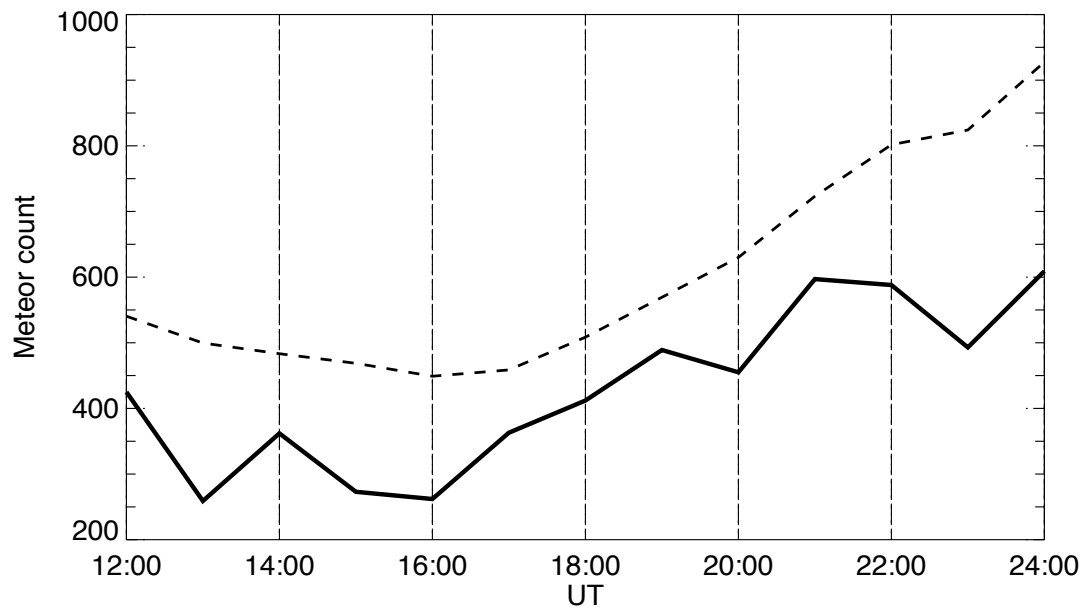


Figure 4.10 Variations of meteor count from 12:00 to 24:00 UT on 22 January 2012 observed by the meteor radar at Tromsø are shown by the solid line. Dashed line denotes monthly averaged meteor counts over January 2012.

precipitation. In this time interval, the auroral particles, which penetrated into 90 km or lower, should have energy of 40 keV or higher (cf. *Rees, 1963; Heinselman, 2000*). Although the sodium atoms are spattered quickly from dust particles through the auroral spattering process (*von Zahn and Hansen, 1988*), the auroral particle precipitation occurred about 20 min earlier than the time of the commencement of the SSL generation. Therefore, the auroral particle spattering is unlikely a major contributor to the SSL generation. On the other hand, since the auroral activity was high over the night, the aurora particle precipitation might produce additional sodium ions through the charge exchange process (cf. *Heinselman, 2000*), consequently the background density of sodium ions might be increased. For example, a life time of a sodium ion at 93 km is about 30 min (*Cox and Plane, 1998*). Through this process, there would be a possibility that the auroral particle precipitation (as another source) contributed to the generation of the SSL to some extent.

4.2.5 The Effect of Advection

For generation mechanisms of SSLs, such a rapid increase of the sodium density implies a possibility of advection (cf. *Clemesha et al., 1978; Batista et al., 1991*). Since the sodium LIDAR observed only the vertical direction on the night of 22

January 2012, evaluation of the effect of the advection is rather difficult. As we mentioned, the *Es* layer extended at least 36 km southward and eastward from the vertical position at Tromsø. With the accordance of timing of the SSL advent with the *Es* layer, we could assume the SSL would have also a similar extent with the *Es* layer. The lifetime of the SSL (about 18 min) and the eastward wind (30 m s^{-1}) might suggest the advection effect and explain the rapid increase of the sodium density, since the movement value ($= 18 \text{ min} \times 30 \text{ m s}^{-1}$) is about 32 km, similar to the extent (about 36 km). Even if the rapid increase of the sodium density from 21:16 to 21:18 UT was due to the advection, we could say that the SSL was generated nearby the field of view of the sodium LIDAR. This is because, as already mentioned before, the EISCAT radar and MR observational values, used in the calculation of the temporal development of the normal sodium ion layer, are spatial average to some extent.

At any rate, by using the point measurement data of the sodium LIDAR, we cannot exclude the possibility of (horizontal) advection. We have made five beam observations (north, south, east, west, and vertical positions) with the sodium LIDAR at Tromsø since October 2012. Thus we will do further investigations of the generation mechanisms of SSLs at high latitudes including the advection effect in the near future.

4.3 Summary

On 22 January 2012, an SSL was observed at about 93-94 km by the sodium LIDAR operated at a high latitude station at Ramfjordmoen, Tromsø, Norway. The auroral activity was high for the night. From 21:18 to 21:36 UT, the sodium density inside the SSL was from about 2 and 6 times greater than the background sodium density. The EISCAT UHF radar detected an *Es* layer of above 90 km between about 20:00 and 23:00 UT. The *Es* layer was located at about 94 km altitude where the SSL was observed from 21:18 to 21:36 UT. This result is likely to indicate that the *Es* layer contributed to the SSL generation. The *Es* layer, however, could provide less than 21% (at largest) of the sodium atoms of the SSL if the abundance of sodium ions is 10% and all the sodium ions are transported of the plasma density in the *Es* layer.

By using observational values obtained with multiple instruments and some model values, we have calculated a temporal development of sodium ions in a normal sodium ion layer under consideration of chemical reactions and the effect of the electric field and the wind. In this calculation, we have used observational data of the electric field, the horizontal wind velocity, neutral temperature (below 100 km), and the electron

density. As the result of this calculation, those processes can provide about 88% of the sodium atoms of the SSL at 94.4 km. No enhancement of meteor count or a bright trail was observed, and auroral particle precipitation with high energy (40 keV or so) occurred 20 min earlier than the time of the commencement of the SSL generation. Thus, effects of meteor absorption and auroral particle spattering appear not to be dominant mechanisms in this event. Therefore, we have concluded that the major source was sodium ions in a normal sodium ion layer, and the SSL was generated by conversion of sodium ions into sodium atoms by a combination of the following effects: (1) the redistribution of the sodium ions of a normal sodium ion layer due to the electric field with strength of about 17-45 mV m⁻¹, and (2) the higher electron density of the sporadic *E* layer facilitated the chemical reactions and also the *Es* layer supplied additional sodium ions. It should be pointed out that we, mainly based on observational data, have, for the first time, demonstrated the possibility of sodium ions in a normal sodium ion layer as a (major) source of an SSL. Furthermore, we have presented that the SSL was located in the lower temperature region, and that there was no temperature enhancement inside the SSL in this event. More efforts are needed to elucidate mechanisms of the rapid growth of the sodium atom density as well as the effect of advection.

Chapter 5

Summary and Conclusions

In this thesis, we have conducted two event studies that investigated two phenomena occurring in the polar MLT region. First, we have investigated dissipation processes and propagation conditions of an upward-propagating GW under geomagnetically quiet conditions. Second, we have evaluated generation mechanisms of an SSL on a night of high auroral activity. The former phenomenon is a manifestation of a coupling process between the MLT and the lower atmosphere, while the latter is a manifestation of coupling processes between the polar MLT and the magnetosphere/ionosphere. Dissipation of GWs plays an important role in the MLT wind dynamics by providing energy and momentum. On some occasions, GWs penetrate through the MLT region into the thermosphere/upper ionosphere and then cause some interesting phenomena there. On the other hand, auroral precipitation and electric fields originating from the magnetosphere often influence significantly thermal conditions and wind dynamics in the polar MLT region. The auroral precipitation causes the Joule and particle heating and ions accelerated by the electric field drive the neutral wind by collisions. Therefore, electromagnetic energy from the magnetosphere is converted into the thermal and dynamical energy of neutral atmosphere. Furthermore, auroral effects might reach the stratosphere and troposphere. For example, nitric monoxide compounds (i.e., NO_x) produced by auroral precipitation in the lower thermosphere are transferred downward to the upper stratosphere, and destroy the ozone there. Therefore, these case studies presented in this thesis contribute to our further understanding of the vertical coupling process between the atmosphere regions and the magnetosphere.

In Chapter 2, an event observed from 16:30 to 24:30 UT on 29 October 2010 during a very geomagnetically quiet interval ($Kp \leq 1$) was addressed. The sodium LIDAR observations conducted in Tromsø, Norway (69.6°N, 19.2°E) captured a

clearly discernible gravity wave (GW) signature. Derived vertical and horizontal wavelengths, maximum amplitude, apparent and intrinsic period, and horizontal phase velocity were about ~ 11.9 km, $\sim 1.38 \times 10^3$ km, ~ 15 K, 4 h, ~ 7.7 h, and ~ 96 m⁻¹, respectively, between a height of 80 and 95 km. Of particular interest is a temporal development of the uppermost altitude that the GW reached. The GW disappeared at around 95 km height between 16:30 and 21:00UT, while after 21:00UT the GW appeared to propagate to higher altitudes (above 100 km). We have evaluated critical-level filtering, convective and dynamic instabilities for dissipation using data obtained by the sodium LIDAR and a meteor radar. It is found that critical-level filtering did not occur, and the convective and dynamic instabilities occurred on some occasions. MF radar echo power showed significant enhancements between 18:30 and 21:00 UT, and an overturning feature of the sodium mixing ratio was observed between 18:30 and 21:20 UT above about 95 km. From these results, we have concluded that the GW was dissipated due to wave breaking caused by instabilities before 21:00 UT. Additionally the GW observed after 21:00 UT is an important evidence for thermospheric GWs that penetrate the polar MLT region based. We have also investigated the difference of the background atmosphere for the two intervals and would suggest that a probable cause of the change in the GW propagation was due to the difference in the temperature gradient of the background atmosphere above 94 km.

In Chapter 3, we evaluated generation mechanisms for an SSL by using data obtained with the sodium LIDAR, the EISCAT UHF radar, the meteor radar, digital camera, and the photometer at Ramfjordmoen, Tromsø, Norway for the SSL event observed on 22 January 2012. The sodium density inside the SSL was from about 2 and 6 times greater than the background sodium density. The EISCAT UHF radar detected an *Es* layer of above 90 km between about 2000 and 2300 UT. The *Es* layer was located at about 94 km altitude where the SSL was observed from 2118 to 2136 UT. This result is likely to indicate that the *Es* layer contributed to the SSL generation. The *Es* layer, however, could provide less than 21% (at largest) of the sodium atoms of the SSL if the abundance of sodium ions is 10% of the electron density of the *Es* layer and all the sodium ions are transported.

By using observational values obtained with multiple instruments and some model values, we have calculated a temporal development of sodium ions in a normal sodium ion layer under consideration of chemical reactions and the effect of the electric field and the wind. In this calculation, we have used observational data of the electric field, the horizontal wind velocity, neutral temperature (below 100 km), and the electron density. As the result of this calculation, those processes can provide about 88% of

the sodium atoms of the SSL at 94.4 km. No enhancement of meteor count or a bright trail was observed, and auroral particle precipitation with high energy (40 keV or so) occurred 20 min earlier than the time of the commencement of the SSL generation. Thus, effects of meteor absorption and auroral particle spattering appear not to be dominant mechanisms in this event. Therefore, we have concluded that the major source was sodium ions in a normal sodium ion layer, and the SSL was generated by conversion of sodium ions into sodium atoms by a combination of the following effects: (1) the redistribution of the sodium ions of a normal sodium ion layer due to the electric field with strength of about 17-45 mV m⁻¹, and (2) the higher electron density of the sporadic *E* layer facilitated the chemical reactions and also the *Es* layer supplied additional sodium ions. It should be pointed out that we, mainly based on observational data, have, for the first time, demonstrated the possibility of sodium ions in a normal sodium ion layer as a (major) source of an SSL. Furthermore, we have presented that the SSL was located in the lower temperature region, and that there was no temperature enhancement inside the SSL in this event. More efforts are needed to elucidate mechanisms of the rapid growth of the sodium atom density as well as the effect of advection.

In this thesis, We have quantitatively discussed the effects of energy influx from the lower and the upper atmosphere by investigating gravity wave and SSL events under different geomagnetic conditions based on observational data. To summarize, we propose that atmospheric instability and electric field applied by the magnetosphere play an important role for vertical coupling of atmosphere in the polar MLT region.

References

- Allen, C. W., *Astrophysical Quantities* 2nd ed., *Athlone Press*, Univ. of London, 1963.
- Arras, C., J. Wickert, G. Beyerle, S. Heise, T. Schmidt, and C. Jacobi, A global climatology of ionospheric irregularities derived from GPS radio occultation, *Geophys. Res. Lett.*, *35*, doi:10.1029/2008GL034158, 2008.
- Aso, T., T. Tsuda, and S. Kato, Meteor radar observations at Kyoto Univ., *J. Atmos. Terr. Phys.*, *41*, 517-525, doi:10.1016/0021-9169(79)900758, 1979.
- Bates, Rayleigh scattering by air, *Planet. Space. Sci.*, *32*, 6, 785-790, 1984.
- Batista, P. P., B. R. Clemesha, D. M. Simonich, Horizontal structures in sporadic sodium layers at 23°S, *Geophys. Res. Lett.*, *18*, 1027-1030, 1991.
- Bilitza, D.: MSIS-E-90 Atmosphere Model, http://nssdc.gsfc.nasa.gov/space/model/models/msis_n.html, 2002.
- Bowman, M. R., A. J. Gibson, and M. C. W. Sandford, Atmospheric sodium measured by a tuned laser radar, *Nature*, *221*, 456-457, 1969.
- Chapman, S., Note on atmospheric sodium, *Astrophys. J.*, *90*, 309, 1939.
- Clemesha, B. R., V. W. J. H. Kirchhoff, D. M. Simonich, and H. Takahashi, Evidence of an extraterrestrial source for the mesospheric sodium layer, *Geophys. Res. Lett.*, *5*, 873-876, 1978.
- Clemesha, B. R., P. P. Batista, and D. M. Simonich, Concerning the origin of enhanced sodium layers, *Geophys. Res. Lett.*, *15*, 1267-1270, 1988.
- Clemesha, B. R., Sporadic neutral metal layers in the mesosphere and lower thermosphere, *J. Atmos. Terr. Phys.*, *57*, 725-736, 1995.

- Clemesha, B. R., D. M. Simonich, P. P. Batista, I. S. Batista, Lidar observations of atmospheric sodium at an equatorial location, *J. Atmos. Sol. Terr. Phys.*, *60*, 1773-1778, 1998.
- Clemesha, B. R., P. P. Batista, and D. M. Simonich, An evaluation of the evidence for ion recombination as a source of sporadic neutral layers in the lower thermosphere, *Adv. Space Res.*, *24*, 547-556, 1999.
- Cox, R. M., and J. M. C. Plane, An ion-molecule mechanism for the formation of neutral sporadic Na layers, *J. Geophys. Res.*, *103*, 6349-6359, doi:10.1029/97JD03376, 1998.
- Delgado, R., J. S. Friedman, J. T. Fentzke, S. Raizada, C. A. Tepley, and Q. Zhou, Sporadic metal atom and ion layers and their connection to chemistry and thermal structure in the mesopause region at Arecibo, *J. Atmos. Sol. Terr. Phys.*, *74*, 11-23, 2012.
- Donahue, T. M., R. Resnick, and V. R. Stull, Distribution in the upper atmosphere of sodium atoms excited by sunlight, *Phys. Rev.*, *104*, 873, 1956.
- Drazin, P. G., The stability of a shear layer in an unbounded heterogeneous inviscid fluid, *J. Fluid Mech.*, *4*, 214-224, 1958.
- Ejiri, M. K., M. J. Taylor, T. Nakamura, and S. J. Franke, Critical level interaction of a gravity wave with background winds driven by a large-scale wave perturbation, *J. Geophys. Res.*, *114*, D18117, doi:10.1029/2008JD011381, 2009.
- Fan, Y. Z., J. M. C. Plane, and J. Gumbel, On the global distribution of sporadic sodium layers, *Geophys. Res. Lett.*, *34*, L15808, doi:10.1029/2007GL030542, 2007.
- Fujii, T., T. Fukuchi (eds.), *Laser Remote Sensing*, CRC Press, Boca Raton, 2005.
- Fritts, D. C., and Rastogi, P. K., Convective and dynamical instabilities due to gravity wave motions in the lower and middle atmosphere: Theory and observations, *Radio Sci.*, *20*, 1247-1277, 1985.
- Fritts, D. C., and Alexander, M. J., Gravity wave dynamics and effects in the middle atmosphere, *Rev. Geophys.*, *41*, 1003, doi:10.1029/2001RG000106, 2003.

- Fritts, D. C., and Vadas, S. L., Gravity wave penetrate into the thermosphere: sensitivity to solar cycle variations and mean winds, *Ann. Geophys.*, 26, 3841-3861, doi:10.5194/angeo-26-3841-2008, 2008.
- Gardner, C. S., T. J. Kane, D. C. Senft, J. Qian, and G. C. Papen, Simultaneous observations of sporadic E, Na, Fe, and Ca⁺ layers at Urbana, Illinois: Three case studies, *J. Geophys. Res.*, 98, 16865-16873, 1993.
- Gibson, A. J., and M. C. W. Sandford, The seasonal variation of the night-time sodium layer, *J. Atmos. Terr. Phys.*, 33, 1675-1684, doi:10.1016/0021-9169(71)90215-7, 1971.
- Gibson, A. J., L. Thomas, S. K. Bhattacharyya, Laser observations of the ground-state hyperfine structure of sodium and of temperatures in the upper atmosphere, *Nature*, 281(5727), 131-132, 1979.
- Gu, Y. Y., J. Qian, G. C. Papen, G. R. Swenson, and P. J. Espy, Concurrent observations of auroral activity and a large sporadic sodium layer event during ANLC-93, *Geophys. Res. Lett.*, 22, 2805-2808, 1995.
- Hall, C. M., The Ramfjordmoen MF radar (69°N, 19°E): application development 1990-2000, *J. Atmos. Sol. Terr. Phys.*, 63, 171-179, 2001.
- Hall, C. M., T. Aso, M. Tsutsumi, S. Nozawa, A. H. Manson, and C. E. Meek, A comparison of mesosphere and lower thermosphere neutral winds as determined by meteor and medium-frequency radar at 70°N, *Radio Sci.*, 40, RS4001, doi:10.1029/2004RS003102, 2005.
- Hansen, G., and U. von Zahn, Sudden sodium layers in polar latitudes, *J. Atmos. Terr. Phys.*, 52, 585-608, 1990.
- Hecht, J. H., R. L. Walterscheid, D. C. Fritts, J. R. Isler, D. C. Senft, C. S. Gardner, and S. J. Franke, Wave breaking signatures in OH airglow and sodium densities and temperatures 1. Airglow imaging, Na lidar, and MF radar observations, *J. Geophys. Res.*, 102, 6655-6668, 1997.
- Hecht, J. H., Instability layers and airglow imaging, *Rev. of Geophys.*, 42, RG1001, doi:10.1029/2003RG000131, 2004.

- Hecht, J. H., Liu, A. Z., Walterscheid, R. L., and Rudy, R. J.: Maui Mesosphere and Lower Thermosphere (Maui MALT) observations of the evolution of Kelvin-Helmholtz billows formed near 86km altitude, *J. Geophys. Res.*, *110*, D09S10, doi:10.1029/2003JD003908, 2005.
- Hedin, A. E., Extension of the MSIS thermosphere model into the lower atmosphere, *J. Geophys. Res.*, *96*, 1159-1172, 1991.
- Heinselman, C. J., J. P. Thayer, and B. J. Watkins, A high-latitude observation of sporadic sodium and sporadic E-layer formation, *Geophys. Res. Lett.*, *25*, 3059-3062, 1998.
- Heinselman, C. J., Auroral effects on the gas phase chemistry of meteoric sodium, *J. Geophys. Res.*, *105*, 12,181-12,192, 2000.
- Hocke, K., Phase estimation with the Lomb-Scargle periodogram method, *Ann. Geophys.*, *16*, 356-358, 1998.
- Hodges Jr., R. R., Generation of turbulence in the upper atmosphere by internal gravity waves, *J. Geophys. Res.*, *72*, 3455-3458, 1967.
- Holton, J. R., The role of gravity wave induced drag and diffusion in the momentum budget of the mesosphere, *J. Atmos. Sci.*, *39*, 791-799, 1982.
- Kane, J. T., C. A. Hostetler, and C. S. Gardner, Horizontal and vertical structure of the major sporadic sodium layer events observed during ALOHA-90, *Geophys. Res. Lett.*, *18*, 1365-1368, 1991.
- Kane, T. J., C. S. Gardner, Q. Zhou, J. D. Mathews, and C. A. Tepley, Lidar, radar and airglow observations of a prominent sporadic Na/sporadic E layer event at Arecibo during AIDA-89, *J. Atmos. Terr. Phys.*, *55*, 499-511, 1993.
- Keay, C. S., and Cepelcha, Z., Rate of observation of electrophonic meteor fireballs, *J. Geophys. Res.*, *99*, 13,163-13,165, 1994.
- Kelley, M. C., The Earth's ionosphere: Plasma physics and electrodynamics second edition, *Academic Press Inc.*, 2009.
- Kirkwood, S., and Collis, P. N., Gravity wave generation of simultaneous auroral sporadic-E layers and sudden neutral sodium layers, *J. Atmos. Terr. Phys.*, *51*, 259-269, 1989.

- Kirkwood, S., and von Zahn, U., On the role of auroral electric fields in the formation of low altitude sporadic-E and sudden sodium layers, *J. Atmos. Terr. Phys.*, *53*, 389-407, 1991.
- Kurzawa, H., and U. von Zahn, Sodium density and atmospheric temperature in the mesopause region in polar summer, *J. Atmos. Terr. Phys.*, *52*, 981-993, 1990.
- Larsen, M. F., A. Z. Liu, C. S. Gardner, M. C. Kelley, S. Collins, J. Friedman, and J. H. Hecht, Observations of overturning in the upper mesosphere and lower thermosphere, *J. Geophys. Res.*, *109*, doi:10.1029/2002JD003067, 2004.
- Li, F., A. Z. Liu, G. R. Swenson, J. H. Hecht, and W. A. Robinson, Observation of gravity wave breakdown into ripples associated with dynamical instabilities, *J. Geophys. Res.*, *110*, D09S11, doi:10.1029/2004JD004849, 2005.
- Lindzen, R. S., Turbulence and stress owing to gravity wave and tidal breakdown, *J. Geophys. Res.*, *86*, 9707-9714, doi:10.1029/95JD03299, 1981.
- Liu, A. Z., R. G. Roble, J. H. Hecht, M. F. Larsen, and C. S. Gardner, Unstable layers in the mesopause region observed with Na lidar during the Turbulent Oxygen Mixing Experiment (TOMEX) campaign, *J. Geophys. Res.*, *109*, D02S02, doi:10.1029/2002JD003056, 2004.
- Liu, Y., and Fan Y, Behavior of sporadic Na layers on small time scale, *J. Atmos. Sol. Terr. Phys.*, *71*, 1374-1382, 2009.
- Lu, X., A. L. Ziu, G. R. Swenson, T. Li, T. Leblac, and I. S. McDermid, Gravity wave propagation and dissipation from the stratosphere to the lower thermosphere, *J. Geophys. Res.*, *114*, D11101, doi:10.1029/2008JD010112, 2009.
- Lue, H. Y., and F. S. Kuo, Comparative studies of methods of obtaining AGW's propagation properties, *Ann. Geophys.*, *30*, 557-570, doi:10.5194/angeo-30-557-2012, 2012.
- Mathews, J. D., Sporadic E : current views and recent progress, *J. Atmos. Sol. Terr. Phys.*, *60*, 413-435, 1998.
- Matuura, N., T. Tsuda, and S. Nozawa, Field-aligned current loop model on formation of sporadic metal layers, *J. Geophys. Res.*, *118*, 1-12, doi:10.1002/jgrs.50414, 2013.

- Meek, C. E., An efficient method for analysing ionospheric drifts data, *J. Atmos. Terr. Phys.*, *42*, 835-839, 1980.
- Miyagawa, H., T. Nakamura, T. Tsuda, M. Abo, C. Nagasawa, T. D. K. Kobayashi, T. Kitahara, and A. Nomura, Observations of mesospheric sporadic sodium layers with the MU radar and sodium lidars, *Earth Planet Science*, *51*, 785-797, 1999.
- Nagasawa, C., and M. Abo, Lidar observations of a lot of sporadic sodium layers in mid-latitude, *Geophys. Res. Lett.*, *22*, 263-266, 1995.
- Namboothiri, S. P., T. Tsuda, M. Tsutsumi, T. Nakamura, C. Nagasawa, and M. Abo, Simultaneous observations of mesospheric gravity waves with the MU radar and a sodium lidar, *J. Geophys. Res.*, *101*, 4057-4063, 1996.
- Nozawa, S., T. D. Kawahara, N. Saito, C. M. Hall, T. T. Tsuda, T. Kawabata, S. Wada, A. Brekke, T. Takahashi, H. Fujiwara, Y. Ogawa, and R. Fujii, Variations of the neutral temperature and sodium density between 80 and 107 km above Tromsø during the winter of 2010-2011 by a new solid state sodium LIDAR, *J. Geophys. Res.*, *119*, 441-451, doi:10.1002/2013JA019520, 2014.
- Nygrén, T., T. Turunen, and H. Rishbeth, Interference of tidal and gravity waves in the ionosphere and an associated sporadic E-layer, *J. Atmos. Terr. Phys.* *52*, 609-624, 1990.
- Oyama, S., J. Kurihara, B. J. Watkins, T. T. Tsuda, and T. Takahashi, Temporal variations of the ion-neutral collision frequency from EISCAT observations in the polar lower ionosphere during periods of geomagnetic disturbances, *J. Geophys. Res.*, *117*, doi:10.1029/2011JA017159, 2012.
- Placke, M., P. Hoffmann, M. Gerding, E. Becker, and M. Rapp, Testing linear gravity wave theory with simultaneous wind and temperature data from the mesosphere, *J. Atmos. Terr. Phys.*, *93*, 57-69, 2013.
- Plane, J. M. C., R. Cox, J. Qian, W. M. Pfenninger, G. C. Papen, C. S. Gardner, and P. J. Espy, Mesospheric Na layer at extreme high latitudes in summer, *J. Geophys. Res.*, *103*, 6381-6389, 1998.
- Plane, J. M. C., C. S. Gardner, J. Yu, C. Y. She, R. R. Garcia, H. C. Pumphrey, Mesospheric Na layer at 40°N: Modeling and observations, *J. Geophys. Res.*, *104*, 3773-3788, doi: 10.1029/1998JD100015, 1999.

- Plane, J. M. C., Atmospheric chemistry of meteoric metals, *Chem. Rev.*, *103*, 4963-4984, 2003.
- Plane, J. M. C., A time-resolved model of the mesospheric Na layer: constraints on the meteor input function, *Atmos. Chem. Phys.*, *4*, 627-638, 2004.
- Press, W. H. and Rybicki, G. B.: Fast algorithm for spectral analysis of unevenly sampled data, *Astrophys. J.*, *338*, 277-280, 1989.
- Qian, J., Y. Gu, and C. S. Gardner, Characteristics of the Sporadic Na layers observed during the Airborne Lidar and Observations of Hawaiian Airglow/Airborne Noctilucent Cloud (ALOHA/ANLC-93) campaigns, *J. Geophys. Res.*, *103*, 6333-6347, 1998.
- Rees, M. H., Auroral ionization and excitation by incident energetic electrons, *Planet. Space Sci.*, *11*, 1209, 1963.
- Reid, I. M., On the measurement of gravity waves, tides and mean winds in the low and middle latitude mesosphere and thermosphere with MF radar, *Adv. Space Res.*, *18*, 131-140, 1996.
- Sawyer, J. S.: Quasi-periodic wind variations with height lower stratosphere, *Q. J. Meteorol. Soc.*, *87*, 24-33, 1961.
- Senft, D. C., R. L. Collins, and C. S. Gardner, Mid-latitude lidar observations of large sporadic sodium layers, *Geophys. Res. Lett.*, *16*, 715-718, 1989.
- She, C. Y., H. Latifi, J. R. Yu, R. J. Alvarez II, R. E. Bills, and C. S. Gardner, Two-frequency LIDAR technique for mesospheric Na temperature measurements, *Geophys. Res. Lett.*, *31*, L24111, doi:10.1029/2004GL021165, 1990.
- She, C. Y., and Yu, J. R., Doppler-free saturation fluorescence spectroscopy of Na atoms for atmospheric application, *Appl. Opt.*, *34*, 1063-1075, 1995.
- Suzuki, S., K. Shiokawa, K. Hosokawa, K. Nakamura, and W. K. Hocking, Statistical characteristics of polar cap mesospheric gravity waves observed by an all-sky airglow imager at Resolute Bay, Canada, *J. Geophys. Res.*, *114*, A01311, doi:10.1029/2008JA013652, 2009.

- Simonich, D. M., B. R. Clemasha, and V. W. J. H. Kirchhoff, The Mesospheric sodium layer at 23°S: Nocturnal and Seasonal Variations, *J. Geophys. Res.*, *84*, 1543-1550, doi:10.1029/JA084iA04p01543, 1979.
- Simonich, D., B. Clemasha, P. P. Batista, Sporadic sodium layers and the average vertical distribution of atmospheric sodium, *Adv. Space Res.*, *35*, 1976-1980, 2005.
- Siskind, D. E., C. A. Barth, and J. M. Russell III, A climatology of nitric oxide in the mesosphere and thermosphere, *Adv. Space Res.*, *21*, 1353-1362, 1998.
- Szewczyk, A., B. Strelnikov, M. Rapp, I. Strlnikova, G. Baumgarten, N. Kaifler, T. Duncker, and U.-P. Hoppe, Simultaneous observations of a Mesospheric Inversion Layer and turbulence during the ECOMA-2010 rocket campaign, *Ann. Geophys.*, *31*, 775-785, doi:10.5194/angeo-31-775-2013, 2013.
- Takahashi, T., Nozawa, S., Tsutsumi, M., Hall, C., Suzuki, S., Tsuda, T. T., T. D. Kawahara, N. Saito, S. Oyama, S. Wada, T. Kawabata, H. Fujiwara, A. Brekke, A. Manson, C. Meek, and R. Fujii, A case study of gravity wave dissipation in the polar MLT region using sodium LIDAR and radar data. *Ann. Geophys.*, *32*, 1195-1205, doi:10.5194/angeo-32-1195-2014, 2014.
- Takahashi, T., S. Nozawa, T. T. Tsuda, Y. Ogawa, N. Saito, T. Hidemori, T. D. Kawahara, C. Hall, H. Fujiwara, N. Matuura, A. Brekke, M. Tsutsumi, S. Wada, T. Kawabata, S. Oyama, and R. Fujii, A case study on generation mechanisms of a sporadic sodium layer above Tromsø (69.6°) during a night of high auroral activity, *Submitted to Ann. Geophys.*
- Taylor, M. J., E. H. Ryan, T. F. Tuan, and R. Edwards, Evidence of preferential directions for gravity wave propagation due to wind filtering in the middle atmosphere, *J. Geophys. Res.*, *98*, 6047-6057, 1993.
- Thrane, E. V., T. A. Blix, C. Hall, T. L. Hansen, U. von Zahn, W. Meyer, P. Czechowsky, G. Schmidt, H.-U. Widdel, and A. Neumann, Small scale structure and turbulence in the mesosphere and lower thermosphere at high latitude in winter, *J. Atmos. Terr. Phys.*, *46*, 119-128, 1987.
- Tsutsumi, M., D. Holdsworth, T. Nakamura, and I. Reid, Meteor observations with an MF radar, *Earth Planets Space*, *51*, 691-699, 1999.

- Tsuda, T. T., S. Nozawa, T. D. Kawahara, T. Kawabata, N. Saito, S. Wada, Y. Ogawa, S. Oyama, C. M. Hall, M. Tsutsumi, M. K. Ejiri, S. Suzuki, T. Takahashi, and T. Nakamura, Decrease in sodium density observed during auroral particle precipitation over Tromsø, Norway, *Geophys. Res. Lett.*, *40*, 4486-4490, doi:10.1002/grl.50897, 2013.
- Vadas, S. L. and Fritts, D. C., Thermosphere responses to gravity waves arising from mesoscale convective complexes, *J. Atmos. Solar Terres. Phys.*, *66*, 781-804, 2004.
- von Zahn, U., P. der Gathen, and G. Hansen, Forced release of sodium from upper atmospheric dust particles, *Geophys. Res. Lett.*, *14*, 76-79, 1987.
- von Zahn, U. and Hansen, T. L., Sudden neutral sodium layers : a strong link to sporadic E layers, *J. Atmos. Terr. Phys.*, *50*, 93-104, 1988.
- Whitehead, J. D., Recent work on mid-latitude and equatorial sporadic-E, *J. Atmos. Terr. Phys.*, *51*, 401-424, 1989.
- Williams, B. P., M. A. White, D. A. Kruger, and C. Y. She, Observation of a large amplitude wave and inversion layer leading to convective instability in the mesopause region over Fort Collins, CO (41N, 105W), *Geophys. Res. Lett.*, *29*, 1850, doi:10.1029/2001GL014514, 2002.
- Wu, D. L., C. O. Ao, G. A. Hajj, M. de la T. Juarez, and A. J. Mannucci, Sporadic E morphology from GPS-CHAMP radio occultation, *J. Geophys. Res.*, *110*, doi:10.1029/2004JA010701, 2005.
- Xu, J., H.-L. Liu, W. Yuan, A. K. Smith, R. G. Roble, C. J. Mertens, J. M. Russell III, and M. G. Mlynczak, Mesopause structure from Thermosphere, Ionosphere, Mesosphere, Energetics, and Dynamics (TIMED)/Sounding of the Atmosphere Using Broadband Emission Radiometry (SABER) observations. *J. Geophys. Res.*, *112*, D09102, doi:10.1029/2006JD007711, 2007.
- Yamamoto, M., T. Tsuda, S. Kato, T. Sato, and S. Fukao, A Saturated inertia gravity wave in the Mesosphere Observed by the Middle and Upper atmosphere radar, *J. Geophys. Res.*, *92*, 11993-11999, 1987.

Zhao, Y., A. Z. Liu, and C. S. Gardner, Measurements of atmospheric stability in the mesopause region at starfire optical range, NM, *J. Atmos. Sol.-Terr. Phys.*, *65*, 219-232, 2003.

Zhou, Q., J. D. Mathews, and C. A. Tepley, A proposed temperature dependent mechanism for the formation of sporadic sodium layers, *J. Atmos. Terr. Phys.*, *55*, 513-521, 1993.